Mineralia Slovaca, Web ISSN 1338-3523, ISSN 0369-2086, https://doi.org/10.56623/ms.2022.54.2.2
54, 2 (2022), 119 – 162, © Authors 2022. CC BY 4.0

Oxidation and decomposition of stratiform SedEx sulfidic mineralization in the epidote-amphibolite facies producing cassiterite, V-rich micas, In-Sn-Ag-Sb-Pb-Bi-Zn-Fe-As-Cu-Ni-Co sulfides and Fe-Ca-Pb carbonates in situ (Bystrý potok locality, Gemeric unit, W. Carpathians)

MARTIN RADVANEC, IVAN HOLICKÝ and STANISLAV GONDA

State Geological Institute of Dionýz Štúr, Mlynská dolina 1, Sk-817 04 Bratislava, Slovakia

Graphical abstract

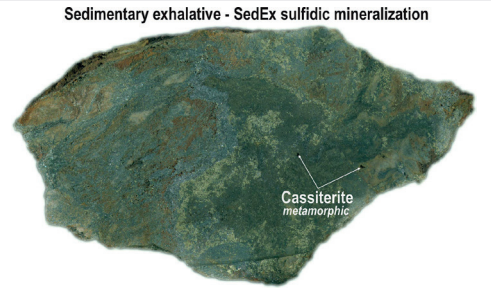

Highlights

- Stratigraphicaly linked Silurian C-rich phyllites with limestone lenses and Late Silurian–Devonian SedEx sulfidic mineralization were metamorphosed in Permian epidote-amphibolite facies and related chlorite-apatite zone of Variscan orogenesis.
- Limestones were transformed to hedenbergite-garnet-epidote-actinolite-chlorite-fluorapatite bearing skarn.
- The Sn-In-Fe-Ag-Pb-Bi-Ni-rich SedEx-sulfides were decomposed by fluid phase oxidation to form metamorphogenic cassiterite, V-rich micas, szomolnokite, hauchecornite, In-rich sakuraiite, Cu-Ag tetrahedrites, siderite a.o. minerals in situ.

Abstract: The studied area of Bystrý potok locality (Gemeric unit, W. Carpathians) is built of lenses of lydites and limestones, being a part of the graphite bearing phyllites of Silurian Holec Beds. The Holec Beds represent the bedrock of the albite-quartz bearing keratophyre (trachyte sensu IUGS classif.) sequence with stratiform SedEx (sedimentary-exhalation) sulfidic mineralization in the Gemeric Lower Paleozoic stratigraphy. This SedEx mineralization was contemporaneous with Late Silurian–Devonian keratophyre/basalt magmatism and originated at 280–340 °C from the seafloor exhalates in Lower Paleozoic rift magmatism. The Silurian-Devonian rock sequences were metamorphosed in Permian.

The limestone lenses were altered to Permian skarn in the epidote-amphibolite facies (526–546 °C, 3–6 kbar) and in related chlorite-apatite zone (420–540 °C) they consisted of garnet $Grs_{41.4-60.2}Sps_{19.8-32.8}Alm_{16.7-22.2}Adr_{0-8.5}$, hedenbergite $Wo_{44.5-50.1}Fs_{31.6-38.2}En_{12.7-20.7}$, epidote, actinolite, fluorapatite, titanite, chlorite, ankerite and siderite. The disseminated original millerite was partially replaced by hauchecornite, hauchecornite-(*Sb)* and cobaltite was formed in the silicate matrix of the skarn.

The Permian metamorphism of the epidote-amphibolite facies and the chlorite-apatite zone has also released a fluid phase rich in O_2, H_2O, CO_2, H_3PO_4, H_2S, HF and V from the organic matter-bearing rock (Holec Beds) into the overlying bed with keratophyres and primary stratiform SedEx sulfidic mineralization where V-rich micas, V-rich chlorite and schreyerite formed. The primary stratiform SedEx sulfidic mineralization composed predominantly of pyrite 1 less pyrrhotite, chalcopyrite, sphalerite 1, galena 1, arsenopyrite, ferrokesterite, stephanite, gudmundite, bismuthinite 1, PbBiSb-rich sulphide ($A_2B_2S_5$-type) and kobellite has been oxidized and decomposed by this fluid phase to form a new metamorphic minerals in situ. The pyrrhotite decomposed to form szomolnokite, pyrite 2, goethite and siderite. The galena 1 was partly oxidized and decomposed to anglesite and cerussite. The In-rich ferrokesterite, Sn-rich sakuraiite and In-rich sphalerite 1 oxidized, decomposed, and reacted with the fluid phase to form cassiterite, chalcopyrite, In-rich sakuraiite and sphalerite 2. The PbSbBi-rich sulfide ($A_2B_3X_6$-type), wittite, bismuthinite 2, native Bi and Se-rich galena 2 are new minerals, formed by the decomposition of original PbBiSb-rich sufhide ($A_2B_2X_5$-type), kobellite and bismuthinite 1.

Tetrahedrites 1–3 ranging from tetrahedrite-*(Fe)*, kenoargentotetrahedrite-*(Fe)* to rozhdestvenskayaite-*(Fe)* show a gradual ordering in three separate zones controlled by immiscibility gaps in the Cu-Ag substitution of tetrahedrite group. These tetrahedrites were formed by the decomposition of the original SedEx ferrokesterite, stephanite and gudmundite. The gudmundite was also commonly oxidized to form valentinite and the decomposition of ferrokesterite, galena 1 and gudmundite also produced bournonite and plumosite-like. Altogether 22 reactions illustrate the relationship between the source SedEx mineralization and the new metamorphic minerals, which have formed at the expense of the original stratiform SedEx sulfidic mineralization in situ.

The metamorphogenic fluid phase, released from the Holec Beds, has been enriched with additional elements from the stratigraphic horizon of the stratiform SedEx sulfidic mineralization and is genetically part of the Permian metamorphic-magmatic-hydrothermal (MMH) cycle (281–256 Ma).

Key words: metallogeny, stratiform SedEx mineralization, metamorphism, cassiterite, In and Bi sulfides, Cu-Ag tetrahedrites, Gemeric unit

Introduction

The occurrence of stratiform sulfidic, mostly pyrite mineralization, in the valley of Bystrý potok creek, is located between the Banisko and Zlatý stôl hills in the central part of Gemeric unit, the Western Carpathians (Fig. 1). Its stratiform position has been verified by three adit levels since 1877, when four mining tariffs for the occurrence of pyrite were granted, forming the "Alžbeta" mining field (Fig. 1b). The final data on mining activities are from 1914–1917. According to mining prospecting, the mineralization has the shape of a column or a narrow lens widened conformably with the dip of beds. The lens is 20 m long, 0.81 to 2 m thick and has a depth range of about 100 m. Mineralization at the lens margin has wedged out or was tectonically cut (Kantor & Fusán, 1952; Grecula et al., 1995). A hereditary tunnel long ca 310 m was dug under the lens. There is a lack of any data about it and no mining maps have been preserved (Kantor & Fusán, 1952). Material on small heaps indicates that variable mineral assemblages have been found in the Alžbeta mining field (Kantor & Fusán, 1952; Ilavský, 1961; Drnzíková & Mandáková, 1970 in Grecula et al., 1995).

The polymetallic ore in the lens is often massive, layered (alternating layers are up to 7 cm thick with different proportions of individual sulfides), but usually a disseminated form is also present, consisting of pyrite, chalcopyrite, galena, sphalerite, pyrrhotite, arsenopyrite, marcasite, ankerite, dolomite, quartz, being accompanied by rare cassiterite, white mica similar to zinnwaldite, tetrahedrite, jamesonite, Sb-Bi sulfides, gold, apatite and muscovite (Grecula et al., 1995). For the first time in this locality, cassiterite was exactly described in Gemeric unit (Kantor & Fusán, 1952).

Metallogenesis at the Bystrý potok locality is the aim of this study. Here, metamorphogenic minerals, formed in the epidote-amphibolite facies and the related chlorite-apatite zone, have been identified in layers, bands and aggregates of the original stratiform SedEx sulfidic mineralization in-situ. These new minerals were formed by oxidation and decomposition of the original SedEx mineralization into cassiterite, valentinite, goethite, szomolnokite, anglesite, V-rich mica, V-rich chlorite, schreyerite, Fe-Mn-Pb carbonates and Ag-Sb-Pb-Bi-Zn-Sn-In-Fe-As-Cu-Ni-Co sulfides in the Permian metamorphism. Metamorphogenic ore minerals and their SedEx source mineralization are also found in the albite-quartz bearing metakeratophyre (trachyte – IUGS). The original keratophyre and SedEx mineralization formed contemporaneously with the keratophyre/basic-spilitic magmatism in the Late Silurian-Devonian rift and are stratigraphically located in the upper part of the host Holec Beds or on their surface. The Holec Beds are composed of lydites and lenses of limestones in the Silurian graphitic phyllite formation of Lower Paleozoic age (Grecula, 1982; Grecula et al., 1995, 2009, 2011). The limestone lenses therein have been altered to form a skarn consisting of garnet, hedenbergite, epidote, actinolite, chlorite and Ni-Co-As-Sb-Bi-rich sulfiides, and this mineral assemblage determines the P-T condition of the epidote-amphibolite facies in this locality.

Geological setting and mineralogy description

The Bystrý potok study area is composed of Lower Paleozoic sequences of Betliar and Smolník formations of Gemeric Volovec Supergroup – pyroclastics, metapsammite, metakeratophyre and metapelite of the Holec Beds. Rocks are metamorphosed in greenschist and epidote-amphibolite facies or biotite zone (530–630 °C, ca 3 kbar) as a result of Permian overheating during the Variscan orogenic metamorphism in the Paleo-Gemeric domain (Fig. 1; Grecula et al., 2009, 2011). The metapelite contains an admixture of psammitic quartz as a passive component during the Variscan metamorphism (MV2; earlier designated as M1), dated from 275 to 262 Ma in the Permian. The clastic quartz of size about 0.5 cm in the pelitic matrix is the reason why this metapelite is traditionally called "porphyroid" in the literature (Fig. 1b., Radvanec et al., 2007).

The Holec Beds are composed of metapelite with the graphite admixture, lenses of lydites, crystalline limestones and rarely the dolomite bearing limestone in the Silurian Beliar Formation of graphitic phyllites of Lower Paleozoic age in the study area. In the stratigraphy of the Lower Paleozoic, the Holec Beds are underlain by keratophyre, basalt-spilite and the stratiform SedEx sulfide mineralization (Fig. 2; Grecula et al., 2009). In the Alžbeta mine field, the stratified SedEx mineralization was located in the upper part of the Holec Beds and the original limestone lenses there were metamorphosed to skarn. The course of Holec Beds with lydite, keratophyre, skarn and stratiform SedEx sulfidic mineralization is NE-SW with dip to the SE (Fig. 3; Kantor & Fusán, 1952).

The disseminated and stratiform sulfidic mineralization in the Gemeric unit was produced by sedimentary-exhalation (SedEx) process and is geotectonically related to bimodal, keratophyre and basalt-spilite magmatism in the seafloor of Late Silurian-Devonian rift (Figs. 1–2). The exhalations accompanying this magmatism have brought ore elements to the seafloor and caused crystallization of the zonal stratiform mineralization. After Devonian rift evolution, the SedEx mineralization was regionally metamorphosed mainly in the greenschists, less frequently in the biotite zone or epidote-amphibolite and amphibolite facies of Variscan orogenic MV2 metamorphism in Permian (275–262 Ma), and within subsequent Alpine orogenesis it underwent local greenschist MAp2 overprint along unroofing ApD2 shear zones (Grecula, 1982; Grecula et al., 1995, 2009, 2011; Radvanec et al., 2007; Radvanec & Grecula, 2016; Radvanec et al., 2017). For these geotectonic and metamorphic events in the Gemeric unit, the SedEx mineralization was modified in-situ to a mixture of original and new metamorphic sulfides, Sn-Pb-Zn-Cu oxides, sulfates, carbonates and other minerals, such are: pyrite, sphalerite, pyrrhotite, chalcopyrite, arsenopyrite, galena, glaucodote, cobaltite, arsenolite, claudetite, cosalite, bismuthinite, native Bi, Cu and Ag, dyscrasite, bournonite, boulangerite, jamesonite, bornite, tetrahedrite, ullma, stibnite, chalcotite, cubanite, quartz, K-feldspar, K-SO minerals, gypsum, white mica, actinolite, garnet,

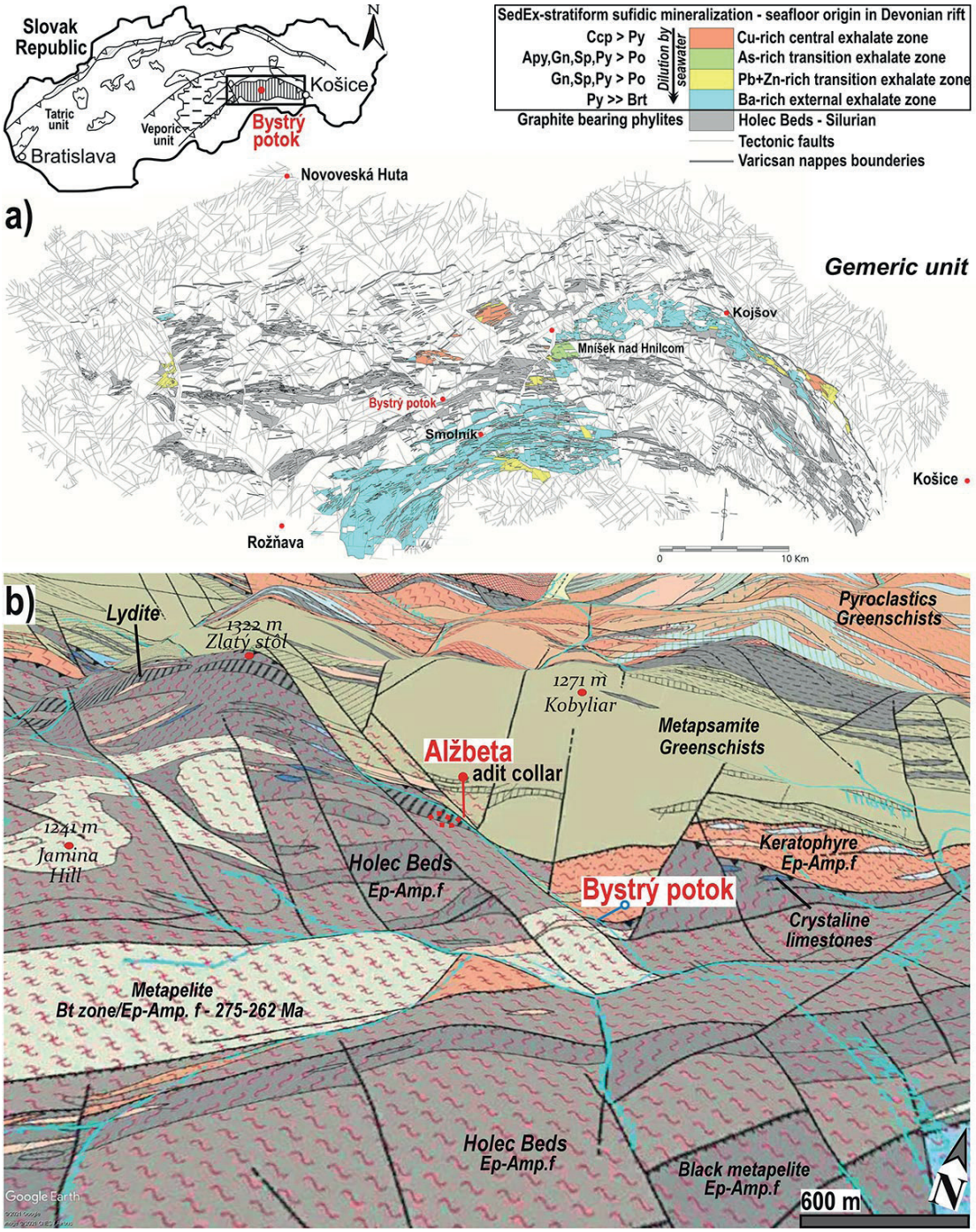

Fig. 1. The Smolník, Mníšek nad Hnilcom and Bystrý potok sites represent main localities of stratiform sulfidic mineralization formed by sedimentary-exhalation (SedEx) process in the Gemeric unit during Variscan riftogeneous phase VD0. The SedEx process is genetically associated with albite-quartz bearing keratophyre (trachyte sensu IUGS classif.) and basalt outflows on the seafloor at the bimodal magmatism of Late Silurian-Devonian rift. **1a** – The map of disseminated stratiform sulfidic mineralization classified from the central to external zones depending on the distance of the outflow place – i.e. where the exhalation fluids, enriched with various elements, reached the seafloor in the rift. Abbreviations: chalcopyrite (Ccp), pyrite (Py), arsenopyrite (Apy), galena (Gn), sphalerite (Sp), pyrrhotite (Po), baryte (Brt). These mineral zones were segmented during the Variscan and Alpine tectonic overprint together with the Holec Beds bedrock, being a part the Silurian Betliar Fm. This bedrock consists of crystalline limestone, sericite-graphite phyllites, graphite phyllites and lydite. **1b** – Geological map and metamorphic facies of the Bystrý potok area in a 3D model according to Grecula et al. (2009, 2011). The metapelite was metamorphosed in the Variscan MV2 Bt zone of epidote-amphibolite facies dated from 275 to 262 Ma, being a consequence of earlier collisional phase of Variscan orogeny and thermal overprint on hot line (Radvanec et al., 2007).

pyroxene, andesine, labradorite, epidote, chlorite, albite, cassiterite, hematite, molybdenite, sulphur, gold, anatase, rutile, apatite, fluorite, biotite, epidote, graphite, ilmenite, uraninite, scheelite, tourmaline, magnetite, topaz, zircon, baryte, talk, dolomite, ankerite, ankerite Mn, siderite, calcite, chalcocite, covellite, malachite, azurite, melanterite, chalcanthite, goethite, szomolnokite, halotrichite, jarosite, copiapite, coquimbite, voltaite, rhomboclase, epsomite, goslarite, cuprite, erythrite, cuprojarosite, kieserite, scorodite, zincite, hexahydrite, leucoxene, lepidocrocite, metavoltine and psilomelane (Bartalský et al., 1993; Grecula et al., 1995; Radvanec & Gonda, 2019). The new metamorphic association has not been clearly defined from the original stratiform SedEx mineralization in these studies, except by Radvanec & Gonda (2019).

According to the results of mineralogical, geochemical and isotope studies, exhalation zones of the SedEx mineralization were identified from central to external zones, depending on the distance of the place where the exhalations ore fluid reached the seafloor. The central Cu-rich exhalation zone was identified according to the amount and relationships of sulfides. Here, chalcopyrite predominates over pyrite. The arsenopyrite, galena, sphalerite and pyrite predominate over pyrrhotite in the transitions of As and Pb-Zn and rarely Ag-rich zones. In the external Ba-rich zone, the dilution of the exhalating fluid with seawater was significant. The disseminated pyrite predominates over rare occurred baryte in this zone (Fig. 1a). The temperature of exhaled fluids dropped from 412–320 °C in the central zone to 176 °C in the outer zone (Radvanec et al., 1993, 2004; Grecula et al., 1995).

The isotopic composition of galena from localities Smolník, Bystrý potok (Alžbeta) and Mníšek nad Hnilcom (Jalovičí hill) corresponds to the development of orogenic lead (Fig. 1). The lead isotope data for galena $^{207}Pb/^{204}Pb$ = 15.5–15.8; $^{208}Pb/^{204}Pb$ = 37.6–38.5; $^{206}Pb/^{204}Pb$ = 17.8–18.1 roughly agree with their Lower Paleozoic stratigraphic age in most applied models, with respect to uranogenic leads, while model calculation based on thorogenic ^{208}Pb gives significantly lower model ages. This higher proportion of thorogenic lead in stratiform mineralizations can be explained by the participation of some isotopically evolved lower crustal and/or metamorphic source during the formation of volcanic rocks on the seafloor. The complex sulfidic mineralization is characterized by values $\delta^{34}S$ = +5 to 15 ‰. It is well consistent to the genetic exhalation-sedimentary model of polymetallic mineralization genetically associated with the Late Silurian-Devonian rift in Gemeric unit (Grecula, 1982; Grecula et al., 1995; Radvanec et al., 2004). The bulk chemical compositions of SedEx mineralizations and their normalized REE contents show the upper crust source for the sulfide formation and subsequent metamorphic event in the chlorite zone on the Smolník locality (Radvanec & Gonda, 2019). The localities of Smolník and Mníšek nad Hnilcom represent typical stratiform SedEx mineralization in the Lower Paleozoic complex (Bartalský et al., 1993; Radvanec et al., 1993; Grecula et al., 1995, 2009). For other less significant localities of stratiform SedEx mineralization see Grecula et al. (1995).

In the studied area of Bystrý potok, the former fluid exhalations belong to the central and transition zones and the mineralization formed from exhalations is located stratigraphically in the upper part of Silurian graphitic phyllites without accompanying basalt volcanism, which occurs significantly in the Smolník locality. The sulfides formation in the Bystrý potok locality was accompanied with the albite-quatrz bearing keratophyre, spilite-keratophyre (chlorite bearing) and its pyroclastics shows the locality as the first manifestation of the fluid smoke exhalation into the seafloor before the main basalt volcanic activity in the Lower Silurian-Devonian rift (Fig 2).

The main mineral in the Bystrý potok locality is pyrite, which predominates over other sulfides. Pyrite commonly forms spheroids, ranging in size from 0.010 to 0.035 mm, with a grain-size of approximately 0.015 mm. Their shape is spherical, rarely elliptical or less regular. The individual pyrite spheroids are usually separated from each other by sphalerite or other sulfides. If the pyrite grains are in contact during growth, a matrix of various pyrite neoblasts formed on their spherical parts of the original individuals. In the combined spheroids of pyrite and pyrrhotite, the pyrrhotite always forms a core around which a new pyrite rim is developed. The pyrite thus forms regular **pyrite rings**. Sometimes the position of pyrrhotite is eccentric, so the hook-like or atoll-shaped pyrite and/or marcasite formations around that pyrrhotite nucleus were formed. In rare cases, marcasite has been found in atoll margins in the form of fine crystalline coatings resulting from the decomposition of pyrrhotite. The core of the annular formations is also formed by the sphalerite, more rarely by galena. **Irregularly shaped pyrite** is also common around pyrite spheroids. It is usually fine-grained. The occurrence of **skeletal pyrite** is also common. It is either in the form of isolated grains or forms aggregates. The free spaces between the individual "ribs" of pyrite are filled by other sulfides, mainly sphalerite or galena (Kantor & Fusán, 1952).

Positions with a monomineralic predominance of sulfides alternate in the SedEx lens. In addition to rolling into parallel strips, the pressure deformation is locally manifested by breccia. That breccia consists of pyrite, sphalerite, pyrrhotite, galena, arsenopyrite and chalcopyrite respectively. Of these, pyrite with sphalerite predominates, while the other sulphides are minor. The grey-black fragments of brecciated ore consist of fine-grained sulfides, which are surrounded by a predominantly coarser-grained matrix of pyrrhotite, sphalerite, chalcopyrite and idiomorphic pyrite. The size of pyrrhotite ranges from 0.05 to 1.0 mm. The size of the pyrite is from 0.1 to 1.0 mm or from 0.1 to 0.2 mm and the size of sphalerite with chalcopyrite has similar dimensions. The individual segments of the breccia are enclosed in cement, formed of coarser-grained sulfides, especially in pyrrhotite, sphalerite and chalcopyrite (Kantor & Fusán, 1952). This sulfide matrix is dark, coloured from brown to black by sphalerite and pyrrhotite. Pyrite is also often present in the form of macroscopically solid clusters or there is pyrite in the form of small idiomorphic grains. The chalcopyrite often occurs in these sulfide po-

sitions and in some parts the disseminated or even more continuous veins of galena were revealed. Veins of galena were also found along the marginal parts of the ore body. In the chalcopyrite or in the mixture of "whole sulfides" the rare gold occurs having size from 0.003 to 0.012 mm.

The quartz is rare in the lens. It is either fine-grained with a sugary appearance or is coarser-grained light grey to milky white. Carbonates seldom form continuous clusters or positions in sulfides that are at most cm thick. In some places of the marginal parts of the lens, the increased concentration of white micas was found (Kantor & Fusán, 1952). The cassiterite belongs to the sulfide association. The idiomorphic cassiterite forms long prismatic crystals up to 0.4 mm. It occurs in the pyrrhotite, sphalerite, chalcopyrite and galena. Irregular small grains of cassiterite were also found in these sulfides. The cassiterite is also present in those parts, where chalcopyrite predominates in the fine-grained quartz. Here it is surrounded by white mica, by quartz and carbonates (l.c.). White mica is a common mineral, sometimes overgrown with "muscovite" and is markedly pleochroic, clear or yellowish to brownish. Its *C*-axis parts are pink-brown in colour and have a low birefringence. According to this optical characteristic, Kantor & Fusán (1952) considered this mica to be the zinnwaldite. The apatite, chlorite and feldspar often occur in the association of cassiterite, sulfides, quartz and white mica. The host rock around the ore lens is silicified and impregnated by sulfides. There are frequent inclusions of idiomorphic pyrite, accompanied by its aggregates and veins (l.c.).

Methodology

Mineralogical and petrological data were obtained by studying samples of skarn, albite-quartz bearing metakeratophyre and samples of stratiform SedEx sulfidic mineralization from the Bystrý potok valley (Figs. 1, 2). Samples were collected from the adit at levels 2 (48° 45' 33.4" N, 20° 40' 31.6" E, Fig. 3) and 1 (dump-2; 48° 45' 33.7" N, 20° 40' 28.8" E and adit).

The relations among minerals were studied in polished thin sections. Chemical composition of minerals was determined by electron microprobe analyses (EMPA). The EMPA of minerals and their crystallization succession were obtained in the State Geological Institute of Dionýz Štúr, Department of microanalysis, Bratislava. The Cameca SX-100 electron microprobe was equipped with three spectrometers and Kevex delta IV EDS system. The natural and synthetic standards were used for calibration. Measuring conditions: acceleration voltages 15 kV and 25 kV, current 10 nA at analyses of carbonates or 20 nA at silicate analyses. The diameter of the electron beam was changed according to the type and size of minerals. Micas were measured by widened beam 7–10 μm, carbonates 10–15 μm and other minerals by 2–5 μm beam. The measurement time from 10 to 60 s was chosen aiming to achieve the required measurement accuracy of given element. Detection limit for individual elements is smaller than 0.05 wt. % with an error 2-sigma.

After study by optical microscope and subsequent measurement by microprobe, the EMPA results for all

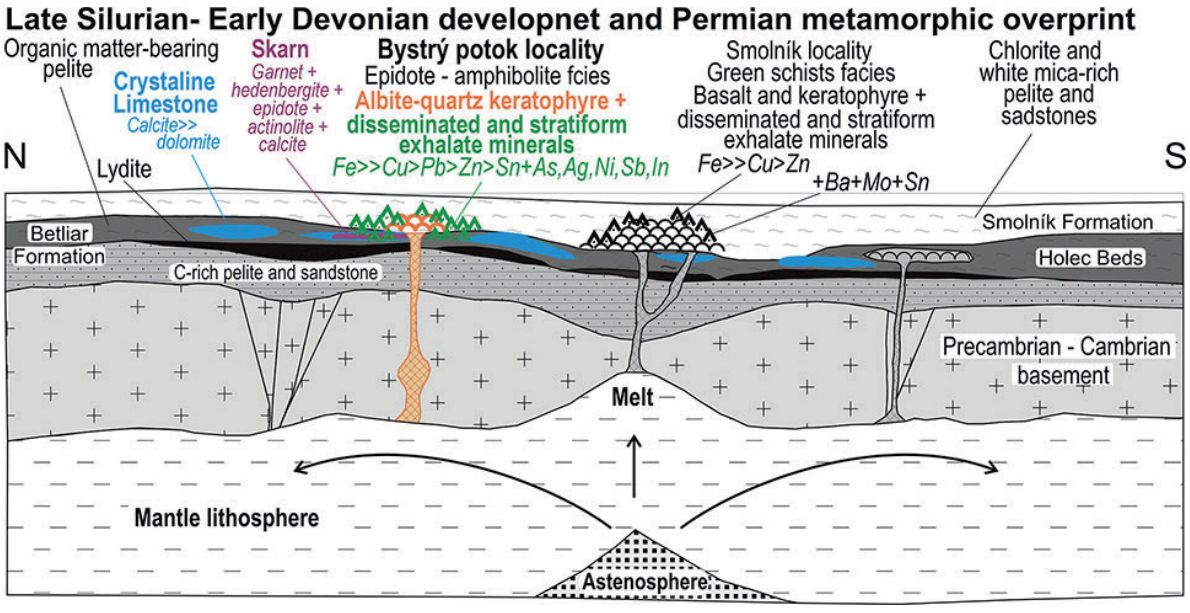

Fig. 2. The Late Silurian–Early Devonian development (VD0, MV0) and schematic Permian metamorphic overprint (MV2) without visualized tectonic arrangement of rocks by Variscan orogeny in Paleo-Gemeric area. The disseminated and stratiform sulfidic mineralization is formed by the sedimentary-exhalation processes (SedEx), related to the bimodal – keratophyre and basalt magmatism in the seafloor in the Late Silurian-Devonian rift. The skarn was formed in the epidote-amphibolite facies in the limestone protolith of the Holec Beds and this facies shows P-T conditions of the stratiform sulfidic mineralization overprint in the Bystrý potok area as well. The epidote-amphibolite and amphibolite facies accompanying the late (VD2, MV2) of Variscan orogeny is of Permian age in the Gemeric unit (Grecula et al., 2009, 2011). These data complement lithostratigraphic development of Gemeric unit proposed by Radvanec & Grecula (2016).

detected minerals were plotted in diagrams, triangle diagrams and in a tetrahedral projection (Figs. 5, 9, 10, 12, 17, 20 and 21). The chemical composition of the carbonates is shown in triangular diagrams between the end-members magnesite-siderite-calcite-cerussite. Chemical analyses of V-rich mica, V-rich chlorite and other minerals show the tetrahedral projection K = KfsFCaA, where the content of V_2O_3, Al_2O_3 and Cr_2O_3 is in the A according to the modified manual of Spear (1995). Mineral assemblages in the KAl = KfsFCA projection show the index minerals of epidote-amphibolite facies and chlorite-apatite zone (Fig. 5a). Projection of K = KfsVTiA (A = Al_2O_3) shows the position of V-rich muscovite-phengite and V-rich phengite-illite between the muscovite-roscoelite-illite-kaolinite end-members including projection of V-rich chlorite, schreyerite, rutile and titanite in this tetrahedral projection (Fig. 5b).

Analyses of sulfides, oxides and other minerals after recalculation to chemical formula were visualized in the individual tetrahedral projections: ZnFeCuIn, ZnFeCuSn, NiFeCoAs, NiSbFeAg, NiSbFeBi, SbFeBiPb, CuSbFeAg, CuSbFePb and CuSbFeAg, while S, O, CO_2 and OH contents were neglected (Figs. 17, 21). Projections of the mineral chemical formulae in each of these element systems show the relationships between the source SedEx minerals and the newly formed metamorphogenic minerals within the end-members.The interconnection of the end-members in the system of elements determines the plane in which the new metamorphogenic mineral was formed at the expense of the SedEx end-members. They are also planes of 22 empirical reactions. See text below and Figs. 5, 17, 20 and 21. The individual projections were combined to show the entire mineral crystallization system in the study area (Figs. 17, 21).

The 22 empirical reactions show reacting source minerals controlled by their chemical formulae, as well as new metamorphic mineral assemblages, also confirmed by their chemical formulae. The composition of the fluid phase has been calculated in the reactions. The relationship between the reacting source minerals in the reactions and the new mineral association is always confirmed by the BSE images (Figs. 4, 6–8, 11, 13–16, 18, 19).

Diagrams, triangle diagrams and a tetrahedron projection of the chemical composition were used for the chemical classification of sulfides rich in Pb, Bi, Sb, Cu, Ag and Fe. In figures all these sulfides are directly compared with reference mineral compositions published in the Mineralogy Database (webmineral.com; Figs. 20–21).

The summary types of formula ABX, $A_9B_2X_8$, A_3BX_3, A_2BX_3, $A_2B_2X_5$, $A_2B_3X_6$, $A_3B_3X_7$ and the term sulfides are used in this study for bournonite, plumosite-like and other sulfosalts composed of Pb, Bi, Sb, Cu, Ag, Fe and S. The contents of Ni, Co, Pb, Cu and Ag are bound in group ***A***, Sb, As and Bi are in group ***B***, and the position of Fe in both groups depends on whether Fe^{3+} is bound together with Sb and Bi in group ***B*** or as Fe^{2+} in group ***A***. This alternative Fe binding was inferred from correlations of element contents and their substitutions in the chemical formulas. The group ***X*** consists of S and Se (see Tables). The chemical formulae of the tetrahedrite group were calculated according to the procedure of Biagioni et al. (2020).

In addition to familiar mineral names such as tetrahedrite, bournonite, plumosite-like, bismuthinite, kobellite, wittite, etc., the rule of gradually decreasing number of *apfu* elements in their chemical formula was applied to the names of new sulfides. The PbBiSb- and PbSbBi-rich sulfides were named according to this rule, see text below.

In the investigated locality, the same sulfides usually have two modes of occurrence, e.g. pyrite 1 and pyrite 2, etc. These generations of sulfides vary according to location and chemical composition, see text and Tables. Only two modifications of chalcopyrite have not been correctly distinguished because they have the same chemical composition, although the position of the chalcopyrites in the mineral associations is obviously different, especially according to their place of occurrence. For this reason, altogether two chalcopyrite generations are collectively referred to as chalcopyrite.

In this study, the term sakuraiite is used for Sn sakuraiite (Sn-rich sakuraiite) and In sakuraiite (In-rich sakuraiite) depending on which element predominates in the sakuraiite formula. These terms also describe the finding that In sakuraiite does not contain Sn. To compare the chemical composition with sphalerite, the chemical formulae of In and Sn sakuraiite was calculated on the basis of 2 atoms and was used in the diagrams (Figs. 9, 10; Tabs. 5, 10).

In this study, we use the traditional term keratophyre in the sense of the rock classification of Grecula et al. (2009, 2011). In addition, the term keratophyre clearly captures the geotectonic background of its origin as a product of magma differentiation on the seafloor in the Late-Silurian and Devonian rift. According to the IUGS chemical classification of volcanic rocks, it is a quartz-albite bearing trachyte metamorphosed in epidote-amphibolite facies.

Mineralogical and petrological results

Mineralogical and petrological data were obtained studying the skarn, albite-quartz bearing metakeratophyre and disseminated and massive sulfide ore layers in the Bystrý potok locality (Figs. 1–3).

Garnet-clinopyroxenite skarn as a marker of P-T metamorphic conditions at the Bystrý potok locality

The common thin layers and small lenses of garnet-pyroxenite skarn with thickness up to 10 cm occur in the **graphite** bearing phyllite formation of Holec Beds (Figs. 2–3). The garnet-pyroxenite skarn represents mostly a fine-grained green avocado coloured rock with purple garnet bearing bands. Texture of skarn is most often fibro-granoblastic, less often granoblastic and frequently banded (Fig. 4). The skarn was formed under control of late Variscan ductile overprint of south-vergent unroofing kinematics VD2 (classification sensu Németh, 2021), being initiated by Variscan post-collisional overheating and tectono-metamorphic overprint MV2 (l.c.) above hot-line in Permian (Fig. 3).

During the gradual evolution of skarn, the limestone protolith was firstly changed by the Late Silurian-Devonian exhalations related to the formation of SedEx mineralization. This fluid SedEx alteration produced

chalcopyrite CuFeS, **galena 1** PbS and **cobaltite 1** $(Co_{0.91}Ni_{0.07}\ Fe_{0.05})_{1.03}As_{0.95}S$ as disseminated mineralization in **calcite** $CaCO_3$ matrix of limestone. Inclusions around 1 µm of galena 1 often occur in the cobaltite 1. The size of chalcopyrite reaches 120 µm, galena 1 around 5 µm and cobaltite 1 up to 20 µm. Only **millerite** $(Ni_{0.99}\ Co_{0.01})S$ of this SedEx mineralization forms aggregates up to 700 µm in size and these aggregates enclose chalcopyrite, galena 1 and the remnants of calcite (Fig. 4d). In limestones small layers and lenses, the calcite was locally accompanied by **dolomite** $Ca_{0.96\text{-}1}(Mg_{0.76\text{-}0.84}Fe_{0.14\text{-}0.2}Mn_{0.06\text{-}0.07})(CO_3)_2$ (Figs. 4c, 5, 11f and 12a).

After formation of disseminated SedEx mineralization, the calcite and locally dolomite bearing matrix of former limestone was metamorphosed and transformed into the skarn. The skarn finally composes of homogeneous **garnet** $Grs_{41.4\text{-}60.2}Sps_{19.8\text{-}32.8}Alm_{16.7\text{-}22.2}Adr_{0\text{-}8.5}$ usually from 50 to 500 µm in size, **hedenbergite** $Wo_{44.5\text{-}50.1}Fs_{31.6\text{-}38.2}En_{12.7\text{-}20.7}$ where MnO ranges from 1.49 to 6.07 wt. %, **epidote** Ps = 0.2–0.4, **actinolite**, **fluorapatite** $Ca_5(PO_4)_3F$, **titanite** $Ca_{1.03}Ti_{0.82}Al_{0.17}Fe_{0.04}Si_{1.02}O_{4.8}F_{0.2}$, **quartz**, **zircon** and remnants of calcite. Short veins of **pyrochroite** and **Mn-rich calcite** $Ca_{0.84\text{-}0.89}Mn_{0.09\text{-}0.12}Fe_{0.01\text{-}0.03}CO_3$ fill cracks in that mineral assemblage (Fig. 4b).

Projection of these minerals in the tetrahedron KAl = KfsFCA shows their relationship typical for epidote-amphibolite facies, which metasomatically formed the epidote-hedenbergite-grossular/almandine-actinolite-chlorite bearing skarn assemblage at a temperature range of 500–600 °C at approximately 2–7 kbar (Spear, 1995; Radvanec et al., 2017) and/or a calculated temperature of 526–546 °C at P = 3–6 kbar according to garnet-clinopyroxene geothermometer (Ravna, 2000; Fig. 5a). The input analyses for the garnet-clinopyroxene geothermometer of Ravna (2000) are given in Table 2. The obtained skarn P-T conditions are in good agreement with the epidote-amphibolite facies conditions found in the wider vicinity of the Bystrý potok locality (Fig. 1b; Grecula et al., 2009). The identical pyroxene, garnet, amphibole, epidote and plagioclase skarns containing magnetite, hematite and sulfides were also formed at the same temperature around 570 °C and by the same process of alteration of original limestone lenses in the Holec Beds on the Trochánka, Javor and Gondárska lúka localities. These skarns also originated in the Variscan orogeny (Faryad & Peterec, 1987).

Determination of the P-T conditions of the epidote-amphibolite facies is crucial in the study of the metamorphism of the Late Silurian–Devonian SedEx disseminated mineralization at the Bystrý potok locality.

Under P-T conditions of the epidote-amphibolite facies a new generation of sulfides has originated in the skarn. In silicates matrix of skarn the irregularly zoned **Ni-rich cobaltite 2** $(Co_{0.73}Ni_{0.22}Fe_{0.05})_1As_{0.97}S_{1.03}$ – $(Co_{0.82}Ni_{0.12}Fe_{0.07})_{1.01}As_{0.96}S_{1.03}$ with a size 20–40 µm was formed and the millerite was partly replaced by **hauchecornite** and by **hauchecornite-*(Sb)*** (Fig. 4d-e). This hauchecornite grain is zoned having Bi-rich parts of $(Ni_{8.56}Co_{0.38}Fe_{0.05})_{8.99}(Bi_{1.34}Sb_{0.47}Fe_{0.24})_{2.05}S_{7.95}$, Sb/Bi-rich $(Ni_{8.40}Co_{0.53}Fe_{0.05})_{8.98}(Sb_{1.44}Bi_{0.42}Fe_{0.17})_{2.03}S_{7.98}$ and Sb-rich

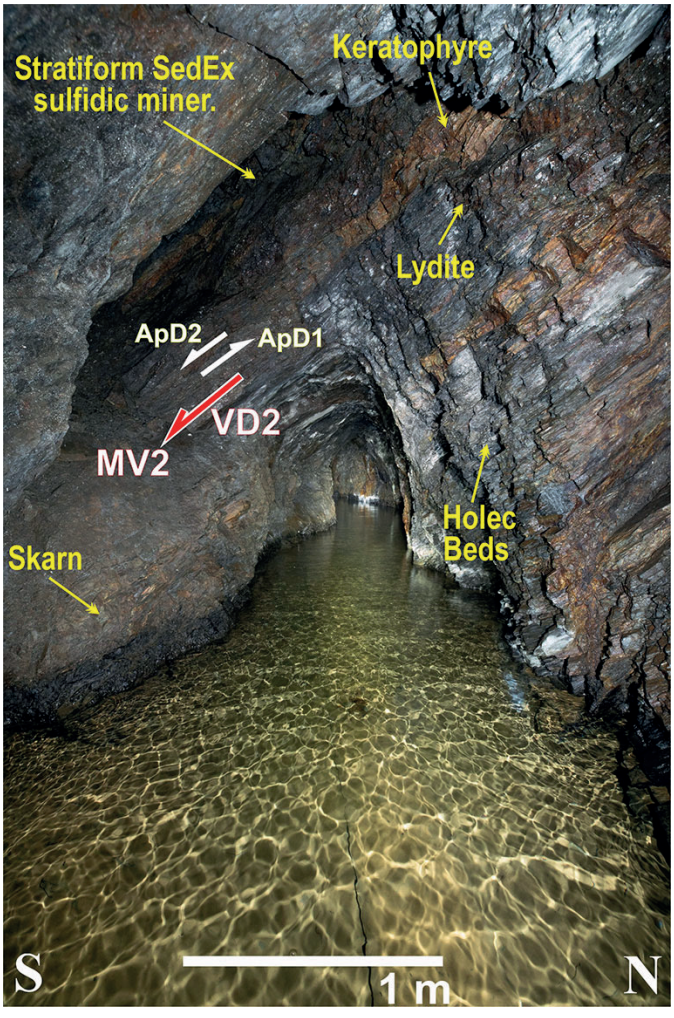

Fig. 3. The occurrence and relationship of stratiform SedEx sulfidic mineralization, albite and quartz bearing metakeratophyre and the skarn in the host Holec Beds found in the 2nd level of the Alžbeta adit in the Bystrý potok locality. The Holec Beds consist of sericite-graphite phyllites, lydite and limestone as a protolith of garnet-hedenbergite-epidote-actinolite bearing skarn. The rock sequence in this locality manifests late Variscan ductile overprint (MV2 metamorphism, in previous papers signed as M1; Radvanec & Gonda, 2019) of south-vergent unroofing kinematics VD2, being initiated by Variscan post-collisional overheating and tectono-metamorphic overprint MV2 above hot-line in Permian. It produced anticline setting and resulting south-vergent unroofing in this locality. Later Paleo-Alpine north-vergent thrusting ApD1 and south-vergent unroofing ApD2 are manifested by brittle-ductile secondary foliation and cleavage. Regional shearing during Neo-Alpine AnD3 phase produced sinistral Transgemeric shear zone trending ENE-WSW, which rotated CCW earlier foliation planes of VD2, ApD1 and ApD2 to direction of shear zone (present general dip is 154/68). Classification of orogenic and metamorphic phases sensu Németh (2021). Photo: Miloš Greisel

$(Ni_{8.23}Co_{0.50}Fe_{0.25})_{8.98}(Sb_{1.70}Fe_{0.14}Bi_{0.08})_{1.92}S_{8.09}$ part respectively. The Fe *(apfu)* is significantly bound in group B with Bi and Sb in these chemical formulae. The Sb* = (Sb + Fe^{3+})/(Sb + Bi + Fe^{3+}) ratios therein range from 0.34 to 0.96 showing the variable influence of $SbFe^{3+}S$ (gudmundite), Bi_2S_3 (bismuthinite) and/or native Bi molecules during the replacemnet of millerite to form zonal hauchecornite (Fig. 4d–e, Tab. 1). The formation of zonal hauchecornite is described by reactions 1, 2 and its formation is visualized in NiSbBiFe tetrahedron between millerite, gudmundite and bismuthinite/native Bi end-members. The SedEx processes produced those reacting source minerals for the formation of new hauchecornite (Fig. 21).

$$\underset{\text{Millerite}}{18NiS} + \underset{\text{Gudmundite}}{FeSbS} + \underset{\text{Bismuthinite}}{Bi_2S_3} + 6H_2O \rightarrow$$

$$\underset{\text{Hauchecornite-}(Sb)}{Ni_9(SbBiFe)_2S_8} + \underset{\text{Hauchecornite}}{Ni_9(BiSbFe)_2S_8} + 6H_2S + 3O_2 \quad (1)$$

$$\underset{\text{Millerite}}{18NiS} + \underset{\text{Gudmundite}}{FeSbS} + \underset{\text{Bi native}}{2Bi} + 3H_2O \rightarrow$$

$$\underset{\text{Hauchecornite-}(Sb)}{Ni_9(SbBiFe)_2S_8} + \underset{\text{Hauchecornite}}{Ni_9(BiSbFe)_2S_8} + 3H_2S + 3O \quad (2)$$

Further details on gudmundite, bismuthinite 1 and the native Bi formation are given in the text below.

In the skarn, the fluorapatite is accompanied by garnet, epidote, hedenbergite and actinolite, representing the major and indexed minerals formed during the replacement of former limestone in the beginning of epidote-amphibolite facies (Fig. 4). The homogeneous grains of fluorapatite do not contain any admixture of other elements and its chemical formula is close to end-member $Ca_5(PO_4)_3F$ (Tab. 2). In different localities of Gemeric unit the same pure fluorapatite in assemblage with tourmaline, biotite, phengitic muscovite, margarite, topaz, stilpnomelane, chlorite, quartz, fluorite, ankerite, dolomite, kutnohorite, rhodochrosite, siderite, magnesite, allanite, U-rich and In-rich minerals, columbite, cassiterite, molybdenite, goyazite and sulfides occur. In all these localities from greisen in direct contact with Permian S-type granite through skarns and veins in granite exocontacts to U-SedEx surface mineralization, the fluorapatite does not contain any admixture of other elements, however it was formed in different P-T conditions of the Permian hydrothermal mineralization. The assemblage where the fluorapatite occurs with phengitic muscovite and chlorite, was named the chlorite-apatite zone and the temperature range 420–540 °C of this zone has a regional enlargement in the Permian hydrothermal mineralization of Gemeric unit (Radvanec & Gonda, 2019, 2020).

The origin of the studied fluorapatite is conditioned by the existence of calcite lenses in the organic-bearing sediments of the Holec Beds, where limestone/calcite in the epidote-amphibolite facies reacted with a fluid phase containing H_3PO_4 and HF to form fluorapatite according to reaction 3.

$$\underset{\text{Limestone}}{5CaCO_3} + \underset{\text{P-F bearing fluid phase}}{3H_3PO_4 + HF} \rightarrow$$

$$\underset{\text{Apatite}}{Ca_5(PO_4)_3F} + 5H_2O + 5CO_2 \quad (3)$$

The position of fluorapatite enclosed in garnet, epidote and actinolite indicates its formation probably in the prograde zone of epidote-amphibolite facies (Figs. 4, 5a). However, it is irrelevant to consider the prograde and/or retrograde state of the chlorite-apatite zone in the study area, because the temperature range of 500–600 °C or 526–546 °C of the epidote-amphibolite facies and the temperature range of 420–540 °C of the chlorite-apatite zone partially overlap, indicating the chlorite-apatite zone as part of the epidote-amphibolite facies.

Texture of polymetallic mineralization

The mineralization of the Bystrý potok locality consists mainly of the basic and original stratiform SedEx-sulfidic mineralization and the new mineralization formed by the in-situ epidote-amphibolite facies and/or by the chlorite-apatite zone overprint. The mineral texture has a fine-grained form up to 1 mm in grain size generally. In this complex mineralization, the sulfide clusters of galena, sphalerite, pyrite, pyrrhotite, chalcopyrite and arsenopyrite predominate over the aggregates and individual disseminated grains of these sulfides. The disseminated form is usually present in graphite bearing phyllites, albite-quartz bearing metakeratophyre and in the skarn. The massive part of mineralization is formed of spots and pseudo-layers coloured brown, yellow and/or they are black. The galena bearing parts have a silver metallic luster and are matt grey to matt black. Spots of dolomite, ankerite, siderite, fluorapatite, chlorite and quartz up to 2 cm in size are enclosed in the sulfide mass. The phengitic V-rich mica has euhedric shape and the individual cassiterites have a hypidiomorphic shape and remnants of SedEx sulfides are always enclosed in this cassiterite aggregate. Both of these minerals reach about 1 mm in the sulfide matrix. The complex mineralization shows that sulfides stratification or layering was formed by the exhalations on the seafloor and also shows the subsequent ductile deformation acting in the epidote-amphibolite and chlorite-apatite zone (Fig. 6).

The original mineral assemblage of the stratiform SedEx mineralization

Sulfide aggregates, accompanied with chlorite with various Fe contents and rarely by quartz, represent a common composition of the SedEx mineralization originated from seafloor exhalations in the Late Silurian-Devonian rift. The original SedEx chlorites are classified according to the daphnite-ripidolite-pycnochlorite series and also the Si = 7.01–7.92 *(apfu)* with Fe^{2+} + Fe^{3+} = 5.01–5.84 bearing chlorite was found (Tab. 2). In addition to sulfides, quartz and chlorites, the allanite-*(Ce)*, monazite, thorite and rutile also occur in the volcanic part of former albite-quartz bearing keratophyre. If exhalations

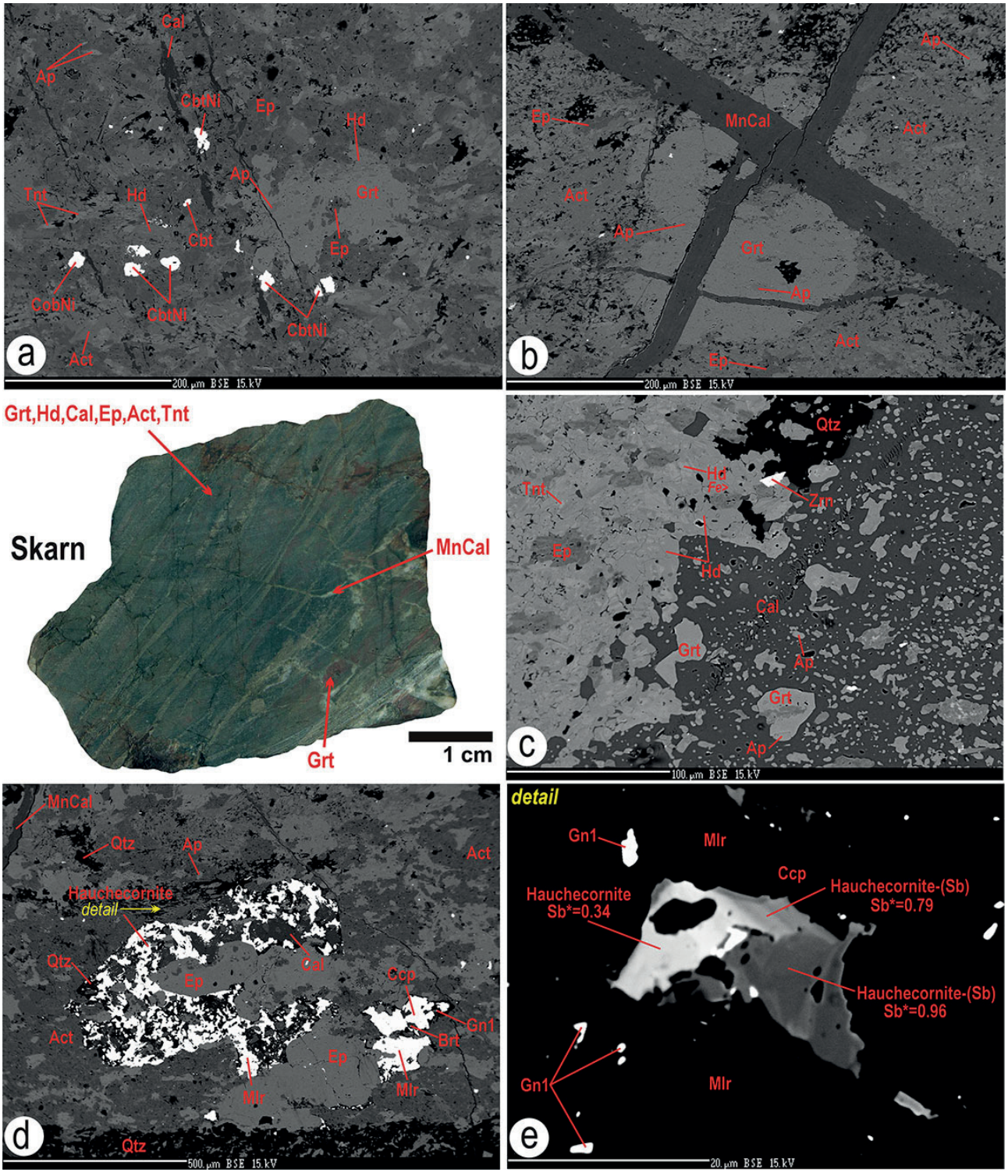

Fig. 4. The skarn minerals were formed in the Permian MV2 epidote-amphibolite facies metamorphism from the limestone protolith of the Holec Beds. ***a*** – The Ni-rich cobaltite (CbtNi) and cobaltite (Cbt) in the matrix composed by garnet (Grt), hedenbergite (Hd), epidote (Ep), titanite (Tnt), fluorapatite (Ap) and actinolite (Act). ***b*** – Mn-rich calcite (MnCal) short veins crosscut the matrix of garnet, epidote, actinolite and fluorapatite. ***c*** – The relationship of former limestone-calcite (Cal) and skarn minerals: quartz (Qtz), zircon (Zrn), garnet, epidote, titanite, hedenbergite. ***d*** – Aggregates of millerite (Mlr), zonal hauchecornite and chalcopyrite in the matrix of epidote, actinolite, fluorapatite, quartz, calcite, Mn calcite and baryte (Brt). ***e*** – Detail in figure ***(d)***. Zonal aggregate of hauchecornite, hauchecornite-*(Sb)* and chalcopyrite (Ccp) in millerite with inclusions of galena 1 (Gn1); Sb* = (Sb + Fe^{3+})/(Sb + Bi + Fe^{3+}). BSE images of mineral assemblages.

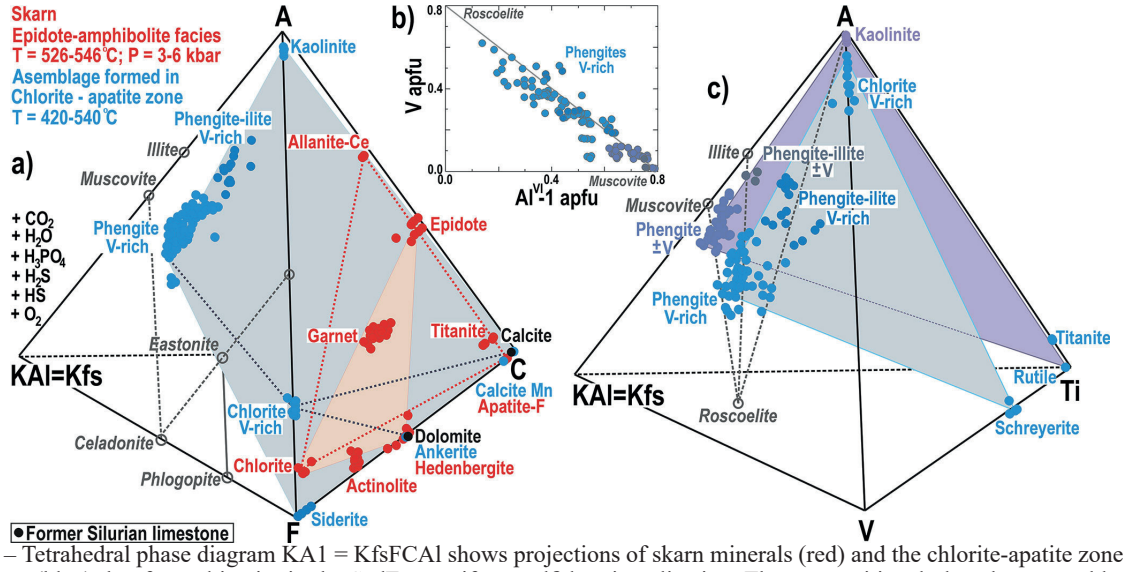

Fig. 5. ***a*** – Tetrahedral phase diagram KA1 = KfsFCAl shows projections of skarn minerals (red) and the chlorite-apatite zone mineral assemblage (blue) that formed in-situ in the SedEx stratiform sulfide mineralization. The compositional plane between chlorite, garnet, hedenbergite, amphibolite and epidote completely classifies the epidote-amphibolite facies according to the metamorphic facies classification criteria (Spear, 1995; Ravna, 2000). The calcite and dolomite (black) are remnants of Silurian limestones protolith, stratigraphically located in the Holec Beds from which the skarn was formed MV2 epidote-amphibolite facies. ***b*** – V-rich micas (phengites) projection and substitution V = Al^{VI} in plot V versus Al^{VI}-1 *(apfu)* based on 12 (O). ***c*** – Tetrahedral phase diagram for the KA1 = KfsVTiA system shows the positions of V-rich mica varieties, V-rich chlorite, kaolinite, schreyerite and titanite were formed by the chlorite-apatite zone.

were spilled into the limestone environment, the SedEx mineralization also includes remnants of calcite and dolomite (Figs. 4c, 11d–f, 13f and 14d).

Much of the SedEx mineralization typically consists of a mixture of monomineral and sulfide aggregates and the various coexisting sulfides are invariably enclosed within the host large sulfide (Figs. 6, 8). The **pyrite 1** $Fe_{1.01}S_{1.98-1.99}$ (Fe/S = 0.51) aggregate (1st pyrite generation) usually encloses **galena 1** $Pb_{0.97}Zn_{0.02}S$, **chalcopyrite** $(CuFe)S_2$, **pyrrhotite** FeS without admixtures of other elements (Fig 8a, 19b–c). Pyrite 1 and pyrrhotite contain Au up to 0.013 wt. % (Tab. 3). The pyrite 1 coexists with BiPb-rich sulfide, whose chemical formula is close to **kobellite** $Pb_{20.18-20.19}Cu_{2.07-2.22}Fe_{1.23-1.35}Ag_{0.61-0.62}Zn_{0.04}Cd_{0.06}Bi_{26.14}Sb_{4.76-4.77}(Se_{0.21-0.24}S_{69.53-69.57})$ with a ratio of Sb/(Sb + Bi) = 0.15 (Tab. 4). This kobellite contains inclusions of **native Bi** $(Bi_{0.85}Sb_{0.05}Fe_{0.05}Pb_{0.02}S_{0.04})$ and together with pyrite 1 is enclosed in an **albite** matrix which is a part of the keratophyre (Fig. 19a). In the albite matrix and in pyrrhotite aggregate with **quartz** the rounded remnants of **PbBiSb-rich sulfide** $(Pb_{1.44-1.48}Fe_{0.23-0.35}Cu_{0.11-0.33}Ag_{0.03-0.04})_2(Bi_{1.19-1.30}Sb_{0.77-0.97})_2(Se_{0-0.19}S_{4.91-4.94})_5$ were found. The size of this PbBiSb-rich sulfide ($A_2B_2S_5$ type) ranges up to 60 µm (Figs. 19c–d, Tab. 4). Several mm large remnants of **stephanite** $Ag_{4.80-5.01}Sb_{0.95-1.02}Fe_{0.01-0.08}Cu_{0-0.18}In_{0.01}S_{3.97-3.99}$ occur with coexisting galena 1 in the quartz matrix and stephanite was also found in the **gudmundite** $Fe^{3+}_{0.98-1.03}Sb_{0.99-1}S_{0.98-1.01}$ (Figs. 18a, c–d, Tab. 3). The always corroded gudmundite is usually associated with the galena 1 and chalcopyrite in the quartz matrix as well (Fig. 18a, e–f). In the gudmundite the Fe atoms are surrounded by 3 Sb atoms and 3 S atoms at the points of an irregular tetrahedron, where the Fe atom is packed between a large Sb atom and a small S atom. The ordinary gudmundite "crystal", in common with other members of the arsenopyrite group is actually a twinned composite simulating a single orthorhombic individual (Buerger, 1939). Therefore, the Fe atom in the chemical formula of gudmundite and also arsenopyrite binds as Fe^{3+} (http://webmin.mindat.org/). Unlike the corroded gudmundite, the **arsenopyrite** $(Fe^{3+}As_{0.97})S_{1.02}$ is stable and occurs together with chalcopyrite, pyrite 1, pyrrhotite and sphalerite 1 or else arsenopyrite is enclosed in galena 1 or sphalerite 1. Arsenopyrite usually forms momomineral aggregates and bands up to 1 cm thick in the SedEx mineralization (Figs. 6d, 8c, 14d; Tab. 3). Rare **bismuthinite 1** $(Bi_{1.78}Fe_{0.22})_2(Se_{0.01}S_{2.94})_{2.95}$ up to 20 µm in the size occurs as an inclusion usually in pyrite 1, pyrrhotite or in galena 1 (Fig. 8a). A number of its analysed grains consistently show a chemical composition with a uniform Fe content of approximately 0.22 *apfu*. The bismutinite 1 shows a Bi content of 1.78 *apfu*, giving a sum of Bi + Fe = 2, and where Bi is substitued by Fe, indicating a form of Fe^{3+} bond in its chemical formula, as in the gudmundite and arsenopyrite (Tab. 4).

The assemblage of pyrrhotite, chalcopyrite, chlorite, quartz, pyrite 1 and **sphalerite 1** $(Zn_{0.70-0.85}Fe_{0.11-0.16}Cu_{0.01-0.08}In_{0.01-0.08})S$ is usually present in the host galena 1 aggregates. However the sphalerite 1 in this association also formed monomineral pseudo-layers, bands and/or spots up to 5 cm thick (Fig. 6 and 8c–f). In that massive sphalerite 1, the indium content ranges irregularly from 0.61 to 8.78 wt. % and Cu from 0.33 to 4.68 (Figs. 15, 16a–b, Tab. 5). The indium content (up to 0.1 *apfu*) progressively correlates with Cu (up to 0.1 *apfu*) and the

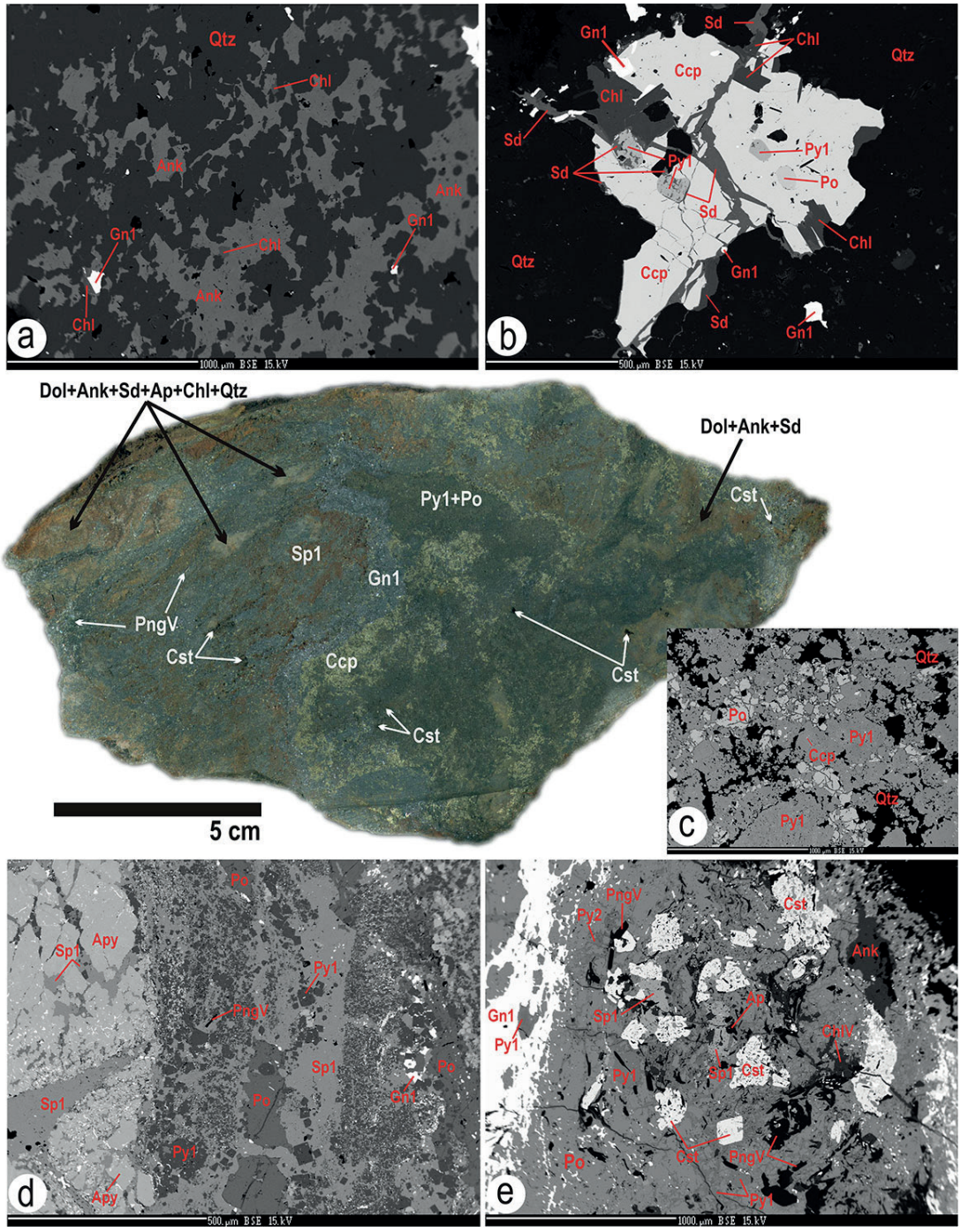

Fig. 6. The massive part of fine-grained mineralization in the Bystrý potok locality consists mainly of the basic VD0 stratiform SedEx sulfidic mineralization and new mineralization formed in-situ by the MV2 epidote-amphibolite facies and by chlorite-apatite zone. That complex mineralization is a mixture of galena 1 (Gn1), sphalerite 1 (Sp1), pyrite 1 (Py1), pyrrhotite (Po), chalcopyrite (Ccp), arsenopyrite (Apy) together with spots containing the dolomite (Dol), ankerite (Ank), siderite (Sd), fluorapatite (Ap), chlorite (Chl) and quartz (Qtz). The cassiterite (Cst) and euhedral V-rich mica (PngV) form disseminated grains and/or aggregates in the matrix of former SedEx sulfides. ***a*** – Ankerite, chlorite, quartz represent common assemblage in carbonates bearing spots. ***b*** – An aggregate of chalcopyrite in a matrix of quartz, chlorite, siderite and galena 1 encloses pyrite 1 and pyrrhotite inclusions. The inclusions of unstable pyrite 1 partially decomposed into siderite, and the siderite fills cracks in the chalcopyrite aggregate. ***c*** – The SedEx mineralization especially represents pyrite 1 with chalcopyrite inclusions, less pyrrhotite and quartz. ***d*** – The sphalerite 1 bearing part contains pyrite 1, pyrrhotite, arsenopyrite, V-rich mica (PngV), and galena 1. ***e*** – The cassiterite aggregates formed in assemblage of V-rich mica, fluorapatite, V-rich chlorite (ChlV), ankerite, pyrite 1, pyrite 2 (Py2), sphalerite 1, pyrrhotite and galena 1. Cassiterite always cemented the original SedEx sulfides. BSE images of mineral assemblages.

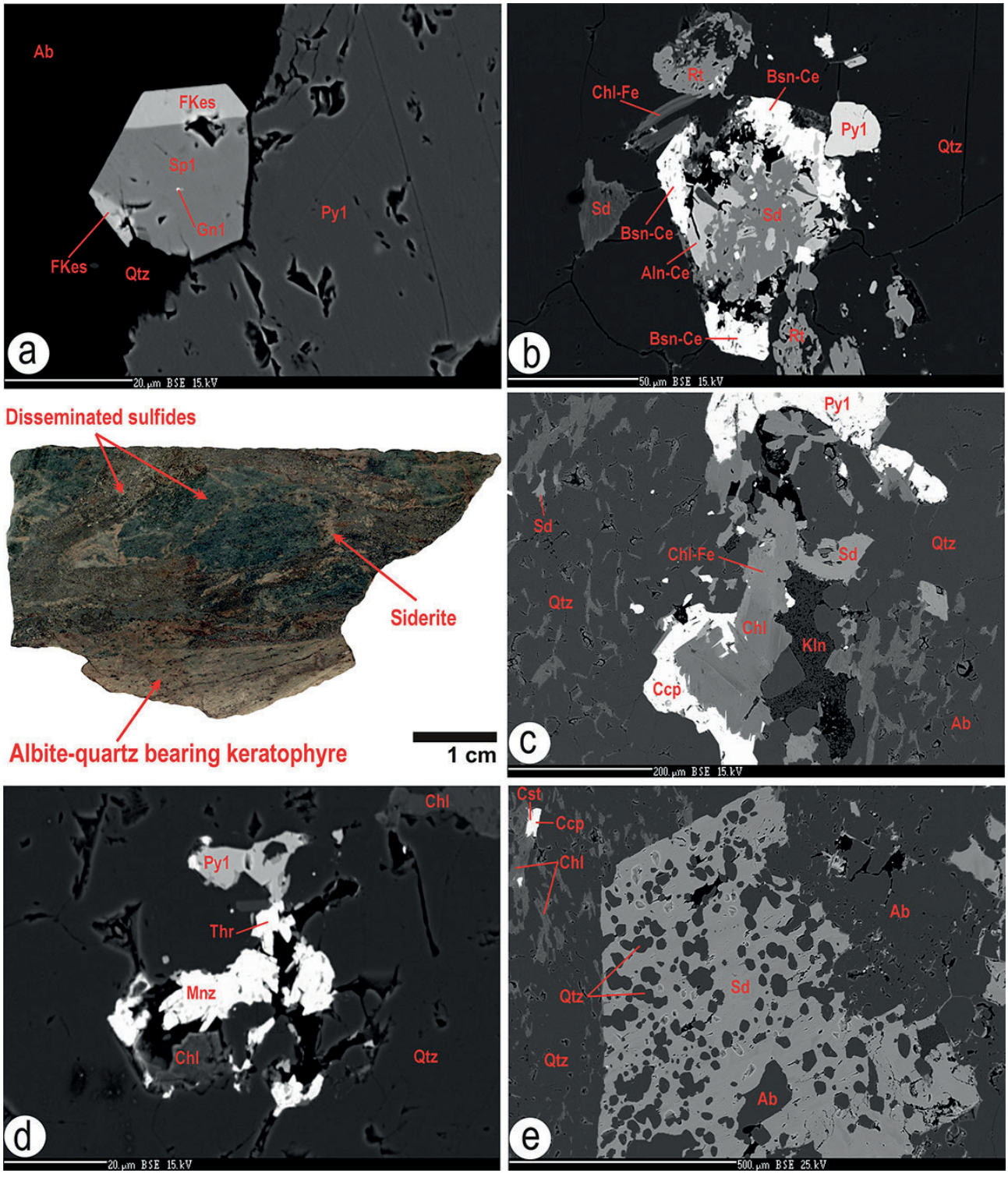

Fig. 7. Albite-quartz bearing metakeratophyre with disseminated SedEx sulfides and newly formed siderite, bastnäsite-*Ce* cassiterite in chlorite-apatite zone. ***a*** – The SedEx ferrokesterite (FKes), sphalerite 1 (Sp1), galena 1 (Gn1), quartz (Qtz) and pyrite 1 (Py1) in the albite part of metakeratophyre. ***b*** – Aggregate composed by Fe-rich chlorite (Chl-Fe), rutile (Rt), siderite (Sd), pyrite 1 (Py1) and the allanite-*Ce* (Aln-Ce) is replaced by bastnäsite-*Ce* (Bsn-Ce) in the quartz part of metakeratophyre. ***c*** – The relationship of siderite, Fe-rich chlorite, kaolinite (Kln), pyrite 1 and chalcopyrite (Ccp) in albite-quartz bearing matrix. ***d*** – Rare monazite (Mnz) and thorite (Thr) in the quartz, chlorite and pyrite 1 matrix. ***e*** – Siderite encloses albite (Ab) and quartz and their relationship to the albite-quartz bearing matrix with cassiterite (Cst) and chalcopyrite. BSE images of mineral assemblages.

sum of Cu + In also progressively correlates with Fe, however the Fe content has a negative trend with Zn, indicating a coupled (CuInFe) ↔ Zn substitution in the sphalerite 1. The chemical formula of sphalerite 1 shows the presence of roquesite ($CuInS_2$) molecule ranging from 1 to 15.6 mol. % and/or ishiharaite (CuFeInZn)S molecule presence according to the (CuInFe) ↔ Zn substitution (Fig. 9). Therefore, the Zn content of sphalerite 1 ranges from 0.7 to 1 *apfu* and this range is used for the term sphalerite in this study (Fig. 9d, 10e–f, Tab. 5).

Aggregates and massive SedEx parts of sphalerite 1 include galena 1 and arsenopyrite. That massive form of sphalerite 1 always includes homogeneous **ferrokesterite** $(Cu_{1.76\text{-}1.96}Fe_{0.88\text{-}0,96}Zn_{0.16\text{-}0.52}Sn_{0.88\text{-}0.92})_4S_4$ less often **In-rich ferrokesterite** $(Cu_{1.72\text{-}1.96}Fe_{0.68\text{-}1.08}Zn_{0.12\text{-}0.52}Sn_{0.84\text{-}1,04}In_{0.04\text{-}0.16})_4S_4$ where indium content ranges from 0.54 to 4.38 wt. % and **Sn-rich sakuraiite** $(Cu_{0.6\text{-}1.72}Fe_{0.6\text{-}0.92}Zn_{0.60\text{-}2.48}Sn_{0.28\text{-}0.84}In_{0\text{-}0.20})_4S_4$ with variable indium content from 0 to 6.02 wt. % (Figs. 8c and 15, Tab. 5). According to the obtained EMPA data, the contents of Cu, Fe, Zn, Sn ± In in the ferrokesterite – Sn sakuraiite – sphalerite 1 series are variable and can be evaluated according to the binary chemical plots in Fig. 10. The positive correlation between Cu versus Sn, Cu versus Fe and Cu+Sn versus Fe was found. The negative correlation is shown by Fe versus Zn and the chaotic correlation is between In versus Sn in the ferrokesterite – Sn sakuraiite – sphalerite 1 series. In these sulfide series, the incorporation of elements is following the Cu + Sn + Fe versus Zn substitution scheme. This substitution trend (CuFeSn) ↔ Zn is valid for ferrokesterite/In-rich ferrokesterite, Sn sakuraiite and it also applies for the coexisting sphalerite 1, if sphalerite 1 very rarely contains Sn (Fig. 10). By comparing the host In-rich sphalerite 1 and the coexisting inclusions of ferrokesterite and Sn sakuraiite, it can be concluded that the In and Sn content did not mix and/or was mixed only locally during the crystallization of sulfides from SedEx exhales on the seafloor. Only In-rich ferrokesterite and Sn sakuraiite contain sporadic amounts of In up to 0.04 *apfu* (Fig. 10a).

Coexisting stannite/ferrokesterite group and sphalerite are considered by many authors to be a reliable geothermometer and in this study it is used to estimate precipitation temperature of described phases. Using the equation of Nakamura & Shima (1982) on the partitioning of Fe and Zn between the sphalerite 1 and ferrokesterite, data were obtained to estimate the temperature of their formation on the seafloor. In sphalerite 1 the ratio Fe/Zn ranges from 0.14 to 0.21 and in ferrokesterite from 1.48 to 4.87. The log of these ratios range from –0.69 to –087 in sphalerite 1 and from 0.17 to 0.81 in ferrokesterite (Tab. 5). Using log (XFeS/XZnS) sphalerite versus log (XCu_2FeSnS_4/XCu_2ZnSnS_4) stannite, Nakamura & Shima (1982) proposed equations and temperature lines between coexisting sphalerite and stannite group. According to these data, ore-forming temperatures were obtained for the Bystrý potok locality from 280 to 340 °C. This temperature result fits well between the exhaled fluid temperature ranges from 412–320 °C in the central zone and to 176 °C in the outer zone, and this temperature is well related to the transition zone of the exhales from which SedEx mineralization formed on the seafloor (Radvanec et al., 1993, 2004; Grecula et al., 1995).

The above stratiform SedEx sulphides are the source mineralization that gave rise to the metamorphogenic minerals in the epidote-amphibolite facies or chlorite-apatite zone.

Decomposition and oxidation of stratiform SedEx mineralization in the epidote-amphibolite facies and related chlorite-apatite zone in situ

The original stratiform SedEx mineralization was metamorphosed in the epidote-amphibolite facies (500–600 °C, resp. 526–546 °C; see discussion in earlier chapter about garnet-clinopyroxenite skarn) and the chlorite-apatite zone (420–540 °C) in situ, causing the formation of skarn and indexed chlorite with apatite in the Bystrý potok locality (Fig. 5a). Like the Holec Beds including skarn and lydite also the SedEx mineralization is an integral part of the tectonic plan formed under control of late Variscan ductile overprint of south-vergent unroofing kinematics VD2, being initiated by Variscan post-collisional overheating and tectono-metamorphic overprint MV2 above hot-line in Permian (Fig. 3). Under the control of this tectono-metamorphic overprint the unstable SedEx minerals in the above temperature ranges have oxidized and decomposed by interaction with the fluid phase.

Decomposition of pyrrhotite, pyrite 1 and galena 1 by oxidation and dolomite replacement

Pyrrhotite and especially pyrite 1 are the basic minerals formed by SedEx processes. They were oxidized and decomposed in interaction with H_2O, O_2, H_2S and CO_2 bearing fluid phase to form **szomolnokite** $Fe_{1.1}S_{0.97}O_4.H_2O$, **pyrite 2** $Fe_{0.98}S_{2.02}$, **goethite** FeO(OH) and **siderite** $Fe_{0.83\text{-}0.98}Ca_{0.01\text{-}0.10}Mg_{0\text{-}0.03}Mn_{0.01\text{-}0.04}CO_3$. At the beginning of the gradual oxidation, szomolnokite and pyrite 2 formed at the expense of pyrrhotite according to reactions 4–5. The resulting szomolnokite fills the place of the former pyrrhotite and the ring around the szomolnokite forms a coexisting pyrite 2. In pyrite 2, the Fe content (45.58 wt. %) is lower and the S content (53.82) is higher compared to pyrite 1, and also the ratio Fe/S = 0.49 is lower compared to the value of 0.51 in the pyrite 1 (Tab. 3). The next oxidation step caused the formation of goethite and siderite on the pyrite 2 showing the complex and gradual decomposition of former pyrrhotite (Figs. 11a–b). In summary, the pyrrhotite bearing spots were alternatively decomposed once into szomolnokite or into szomolnokite and pyrite 2 or into szomolnokite, pyrite 2 and siderite or into szomolnokite, pyrite 2, goethite and siderite or sometimes only siderite according to reactions 6–8 (Figs. 11a–c, 13c, 14b). Macroscopically, this transformation is reflected in the samples as dark brown to black between the pyrite and chalcopyrite.

$$\underset{\text{Pyrrhotite}}{FeS} + H_2O + 2O_2 \rightarrow \underset{\text{Szomolnokite}}{FeSO_4.H_2O} \quad (4)$$

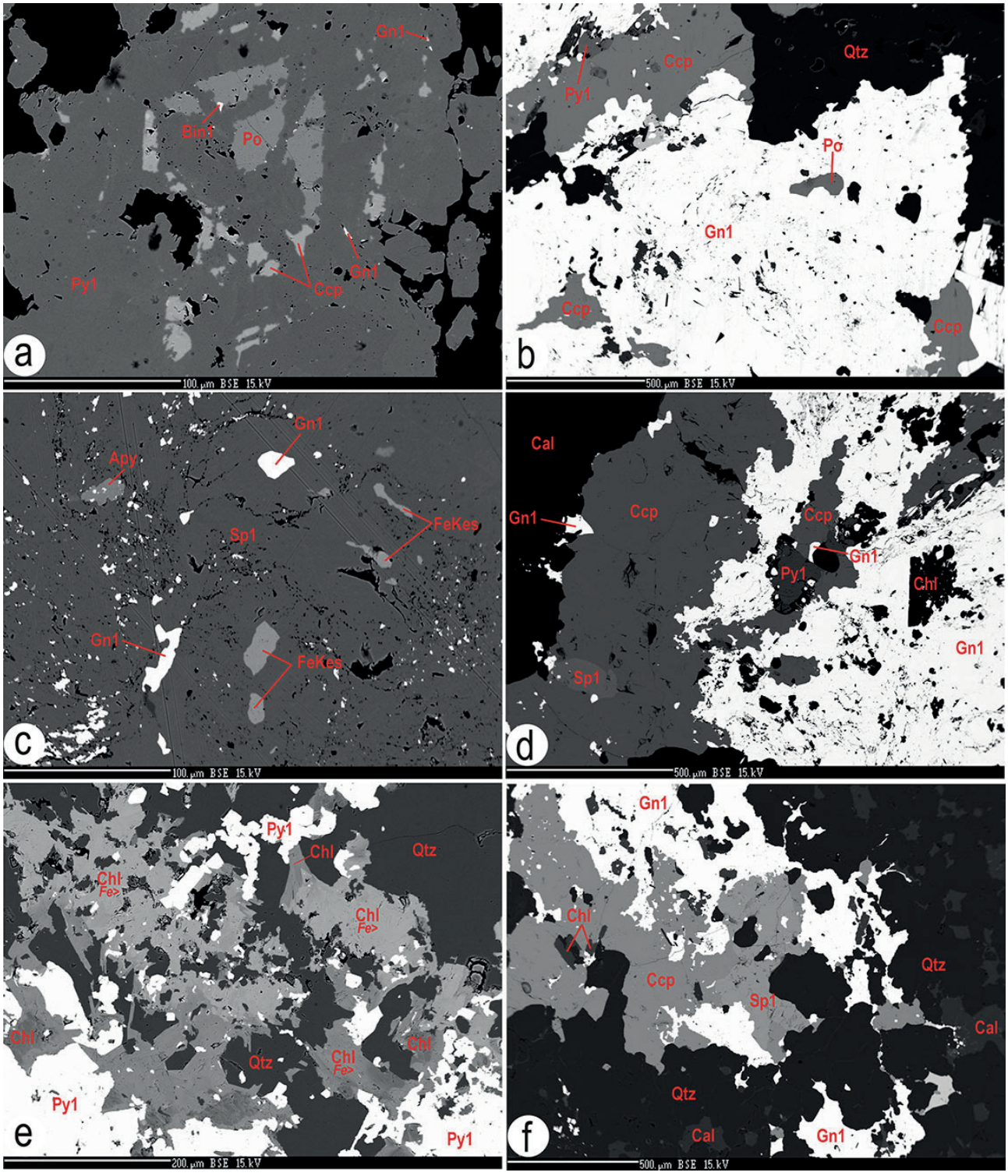

Fig. 8. The common composition and structure of stratiform SedEx sulfidic mineralization, which formed from seafloor exhalates in the Late Silurian-Devonian rift. ***a*** – Pyrite 1 (Py1) closes pyrrhotite (Po), chalcopyrite (Ccp), galena 1 (Gn) and bismuthinite 1 (Bin1). ***b*** – Pyrite 1, chalcopyrite, pyrrhotite, galena 1 and quartz (Qtz) mass assemblages. ***c*** – Inclusions of galena 1, arsenopyrite (Apy), ferrokesterite (FKes) in the host sphalerite 1 (Sp1). ***d*** – Calcite (Cal), chalcopyrite, sphalerite 1, pyrite 1, chlorite (Chl) and galena 1 assemblage. ***e*** – The relationship of pyrite 1, quartz (Qtz), Fe-rich chlorite (Chl, Fe >) and chlorite. ***f*** – Calcite, sphalerite 1, chalcopyrite, chlorite, galena 1and quartz assemblage. BSE images of mineral assemblages.

$$\underset{\text{Pyrrhotite}}{2FeS} + H_2S + 5O \rightarrow \underset{\text{Szomolnokite}}{FeSO_4.H_2O} + \underset{\text{Pyrite 2}}{FeS_2} \quad (5)$$

$$\underset{\text{Pyrrhotite}}{3FeS} + H_2O + CO_2 + 5O \rightarrow$$

$$\underset{\text{Szomolnokite}}{FeSO_4.H_2O} + \underset{\text{Pyrite 2}}{FeS_2} + \underset{\text{Siderite}}{FeCO_3} \quad (6)$$

$$\underset{\text{Pyrrhotite}}{4FeS} + 2H_2O + CO_2 + 3O_2 \rightarrow$$

$$\underset{\text{Szomolnokite}}{FeSO_4.H_2O} + \underset{\text{Pyrite 2}}{FeS_2} + \underset{\text{Goethite}}{FeO(OH)} + \underset{\text{Siderite}}{FeCO_3} + HS \quad (7)$$

$$\underset{\text{Pyrrhotite}}{FeS} + H_2O + CO_2 \rightarrow \underset{\text{Siderite}}{FeCO_3} + H_2S \quad (8)$$

In contrast to the pyrrhotite, the pyrite 1 is more stable phase in P-T conditions of chlorite-apatite zone. Pyrite 1 was only partially decomposed by oxidation to form siderite or goethite according to reactions 9 and 10 (Figs. 6b, 11a–b, 13b and 13f).

$$\underset{\text{Pyrite 1}}{FeS_2} + 2H_2O + CO_2 \rightarrow \underset{\text{Siderite}}{FeCO_3} + 2H_2S + 0.5O_2 \quad (9)$$

$$\underset{\text{Pyrite 1}}{FeS_2} + 3H_2O + HS \rightarrow \underset{\text{Goethite}}{FeO(OH)} + 3H_2S + 0.5O_2 \quad (10)$$

Dolomite, as the remnant of Silurian limestones in the SedEx mineralization, was gradually replaced by **ankerite** $Ca_{0.98\text{-}1}(Fe_{0.24\text{-}0.50}Mg_{0.48\text{-}0.66}Mn_{0.04\text{-}0.10})(CO_3)_2$, goethite and finally by the siderite according to the reaction 11 (Figs. 11d, f and 13f).

$$\underset{\text{Dolomite}}{MgCa(CO_3)_2} + \underset{\text{Pyrrhotite}}{3FeS} + 4H_2O + CO_2 + HS \rightarrow$$

$$\underset{\text{Goethite}}{FeO(OH)} + \underset{\text{Ankerite}}{FeCa(CO_3)_2} +$$

$$+ \underset{\text{Siderite}}{FeCO_3} + 0.5O_2 + 4H_2S + \underset{\text{in Chlorite}}{Mg^+} \quad (11)$$

Galena 1 aggregates were oxidized and decomposed to **anglesite** $Pb_{0.89}Bi_{0.07}SO_4$ and **cerussite** $PbCO_3$. Anglesite and cerussite partially replaced the margin of host galena 1 and/or replaced galena 1 around the cracks in it according to reaction 12 (Figs. 11c and 14d, Tab. 6, 7).

$$\underset{\text{Galena 1}}{2PbS} + H_2O + CO_2 + 2O_2 \rightarrow$$

$$\underset{\text{Anglesite}}{PbSO_4} + \underset{\text{Cerrusite}}{PbCO_3} + H_2S \quad (12)$$

V-rich micas, V-rich chlorite and schreyerite formation

Euhedral and prismatic **V-rich micas** up to 2 mm in size and **V-rich chlorites** crystallized omnidirectionally in various sulfide aggregates. These micas and chlorite were found along with the coexisting fluorapatite and cassiterite, although their main occurrences are in the galena 1, dolomite, allanite-*(Ce)* and pyrite 1 aggregates

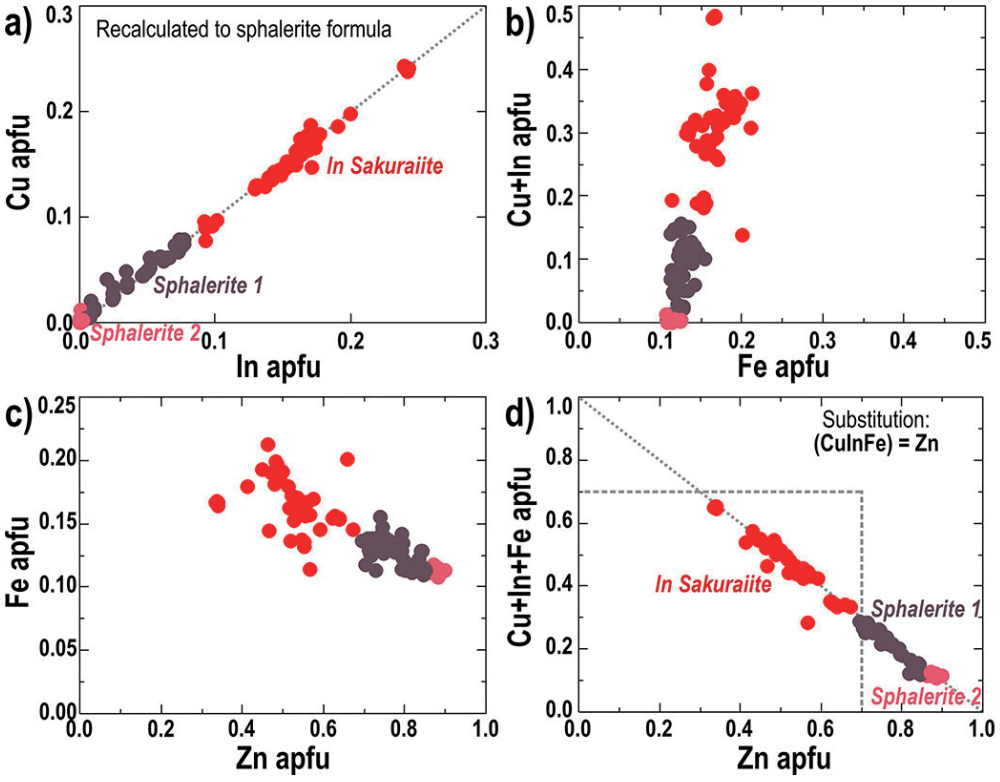

Fig. 9. Binary plots showing chemical composition *(apfu)* of In-rich sphalerite 1, In-rich sakuraiite and sphalerite 2: **a** – Cu *vs*. In; **b** – Cu + In *vs*. Fe; **c** –Fe *vs*. Zn; and **d** – Cu + In + Fe *vs*. Zn. The In-rich sphalerite 1 was formed by the SedEx exhales in Late Silurian – Devonian rift. The In-rich sakuraiite and sphalerite 2 were formed by the oxidation and decomposition of In-rich sphalerite 1 in the Permian chlorite-apatite zone according to reaction 16, see text.

(Figs. 13 and 14b). The optical characteristics of V-rich micas are close to zinnwaldite and the individual V-rich micas are zonal. The core of the prismatic grain is usually **V-rich muscovite-phengite** and the rim forms **V-rich phengite-illite** however their intergrowth were also found. V-rich chlorite forms the outer rim of V-rich mica but separate accumulations of V-rich chlorite were found as well (Fig. 6e, 13d–f, 14b, 15a). The V_2O_3 content ranges from 0.47 to 10.05 wt. % in V-rich muscovite-phengite, in the V-rich phengite-illite ranges from 1.18 to 9.35 and in V-rich chlorite from 0.72 to 2.46. In V-rich micas the variable Cr_2O_3 content reaches up to 3.11 wt. % (Tab. 9).

The chemical classifications of V-rich micas in K = KfsFCA projection, where A = $(Al^{Total}+V)/2-(K/2)$ shows their general position in mineral content assemblages formed by the chlorite-apatite zone near the end-members of muscovite and illite with affinity to kaolinite (Fig. 5a, Tab. 9). The chemical formulas of V-rich micas show $V = Al^{VI} - 1$ substitution in the range up to 0.8 apfu between muscovite and roscoelite end-member (Fig. 5b). The roscoelite $KV_2AlSi_3O_{10}(OH)_2$ represents vanadium analogue of muscovite where $V = Al^{VI}$ (Fleet, 2003). In the projection K = KfsVTiA, where $A = Al^{Total}/2-(K/2)$, two modes of V-rich micas were found. The low vanadium content up to 0.12 *apfu* in the phengite and phengite-illite classifies this mica near the muscovite and illite end-member, and this low-vanadium mica is coexistent with kaolinite, titanite, and rutile. The V-rich mica with vanadium content ranging from 0.16 to 0.62 *apfu* coexists with V-rich chlorite and Ti-V-rich oxide (Fig. 5c). That oxide $(V_{1.15}Fe^{3+}_{0.5}Cr_{0.21}Mn^{3+}_{0.08}Sc_{0.04}Al_{0.02})_2(Ti_{2.63}Sr_{0.13}U_{0.09}Pb_{0.07}Sn_{0.03}Zn_{0.03}Si_{0.01}Mg_{0.01})_3O_9(OH)_{0.5}$ is **schreyerite** close, belongs to the schreyerite group containing (OH) and has a varied association of elements according to its stoichiometry (Tab. 8). The schreyerite reaches a size of 30 μm and occurs with chalcopyrite, galena 1, V-rich mica and szomolnokite (Fig. 13c).

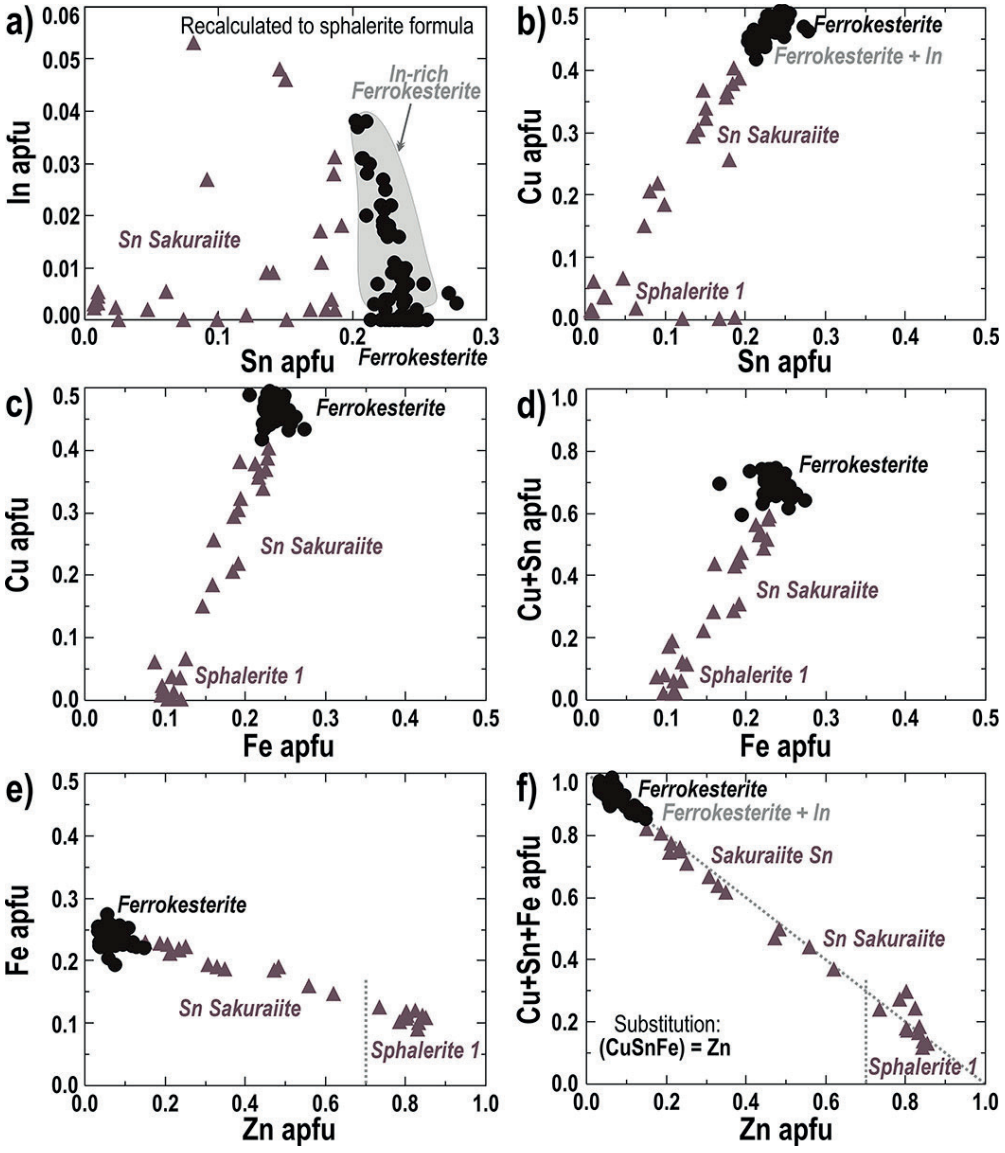

Fig. 10. Binary diagrams showing the chemical compositions of ferrokesterite, Sn-rich sakuraiite and sphalerite 1 formed from SedEx exhalates in the Late Silurian-Devonian rift. (**a**) In *vs*. Sn; (**b**) Cu *vs*. Sn; (**c**) Cu *vs*. Fe; (**d**) Cu + Sn *vs*. Fe; (**e**) Fe *vs*. Zn; and (**f**) Cu + Sn + Fe *vs*. Zn.

The EMPA data of V-rich micas show that their total contents range from 93.89 to 100.08 wt. % including H_2O and often K-deficient. Some V-rich micas appear to be mica phases with A2M structure and their total contents range around 100 wt. % including H_2O (Tab. 8). Other K-deficient analyses with total contents below 99 wt. % indicate H_2O enrichment of V-rich micas and they represent therefore likely the interlayer-deficient micas. Such a mica is also roscoelite with a total content of 93 to 95.44 wt. % (Fleet, 2003). The roscoelite and vanadium muscovite are associated with remobilization of vanadium from black shales and mafic rocks (Fleet, 2003). The V-rich micas studied compare well with the vanadium- and Cr-bearing phengite (containing up to 6.93 wt. % V_2O_3 and 1.52 wt. % Cr_2O_3) found in quartz-rich graphitic black shales (Morad, 1990).

In the Bystrý potok locality the sources of vanadium for V-rich mica, V-rich chlorite and schreyerite formations are from graphite-bearing phyllites of Holec Beds, where in the epidote-amphibolite facies and in the chlorite-apatite zone, the vanadium was released from the organic-rich layer during the conversion of the organic matter to graphite. Round graphite often occurs enclosed in fluorapatite and in galena 1 (Fig.16e). In the fluid phase of the chlorite-apatite zone, vanadium was transported and subsequently bound in close proximity to its source, and the binding of vanadium well explains the occurrence of V-rich micas, V-rich chlorite, and schreyerite in the studied mineralization, which lithostratigraphically overlies the source of the vanadium from the underlying Holec Beds (Fig. 2). However, the varied elements composition of the schreyerite shows mobilization of not only of V but also Cr, Fe, Mn, Sr, Sc and U from the underlying Holec Beds into the SedEx stratiform mineralization.

Cassiterite formation

Cassiterite SnO_2 forms individual, usually hypidiomorphic grains or aggregates as a common oxide formed at the expense of SedEx mineralization in situ (Figs. 6e, 14 and 15). Its chemical composition shows a simple SnO_2 content without the addition of other elements. It is typical for the composition of cassiterites in all localities of the Gemeric unit (Radvanec & Gonda, 2019; Tab. 8). Cassiterite aggregates enclose pyrrhotite, pyrite 1, fluorapatite and galena 1 and/or chalcopyrite or arsenopyrite, depending on spot where the cassiterite aggregate originated in the host SedEx mineralization. The occurrence of coexisting V-rich mica, fluorapatite and xenotime-*(Y)* in the cassiterite is also variable. Some cassiterite grains or aggregates contain them, others are devoid of them (Fig. 14). The formation of cassiterite in situ is conditioned by the occurrence, decomposition and oxidation of suitable Sn-rich source sulfides such as ferrokesterite and/or Sn sakuraiite. The ferrokesterite and Sn sakuraiite have originated by the SedEx processes and decomposed in the chlorite-apatite zone by oxidation. Figure 15 shows an unstable ferrokesterite residue surrounded by chalcopyrite, and cassiterite forms a thin ring around this chalcopyrite. This ferrokesterite oxidation can be described by reaction 13. Alternatively, the reaction of ferrokesterite, goethite and CO_2 shows the formation of chalcopyrite, cassiterite and siderite according to reaction 14.

$$\underset{\text{Ferrokesterite}}{Cu_2FeSnS_4} + \underset{\text{Pyrite 1}}{FeS_2} + 2H_2O \rightarrow$$
$$\underset{\text{Chalcopyrite}}{2CuFeS_2} + \underset{\text{Cassiterite}}{SnO_2} + 2H_2S \qquad (13)$$

$$\underset{\text{Ferrokesterite}}{Cu_2FeSnS_4} + 2\underset{\text{Goethite}}{FeO(OH)} + CO_2 \rightarrow$$
$$\underset{\text{Chalcopyrite}}{2CuFeS_2} + \underset{\text{Cassiterite}}{SnO_2} + \underset{\text{Siderite}}{FeCO_3} + H_2O \qquad (14)$$

Mineralogical results show that the oxidation of ferrokesterite and Sn sakuraiite proceeds from the margin in a stepwise manner and the unreacted ferrokesterite and Sn sakuraiite residues are always oval in the host chalcopyrite (Fig. 15). When ferrokesterite and Sn sakuraiite are in direct contact with cassiterite, the chemical formula of the relics is non-stoichiometric and their analyses are a mixture of the former Sn-rich sulfide and newly formed cassiterite reaching Sn up to 41 wt. % (Fig. 15b).

Valentinite formation

The decomposition of unstable former SedEx gudmundite caused **valentinite** $Sb_{1.99}Fe_{0.05}O_3$ and siderite formation according to the reaction 15 (Fig. 18f). Under the conditions of chlorite-apatite zone the gudmundite partly decomposed and its composition shows only Sb_2O_3 content except of FeO up to 0.95 wt. % (Tab. 6).

$$2FeSbS + 2H_2O + 2CO_2 \rightarrow$$
$$\underset{\text{Valentinite}}{Sb_2O_3} + \underset{\text{Siderite}}{2FeCO_3} + 2H_2S \qquad (15)$$

In-rich sakuraiite formation

The **In-rich sakuraiite** $(Zn_{0.34\text{-}0.64}Fe_{0.15\text{-}0.19}Cu_{0.09\text{-}0.2}In_{0.09\text{-}024})S_{0.98\text{-}1.02}$ was formed by decompositions of indium bearing sphalerite 1, ferrokesterite and Sn sakuraiite. These three carriers of In and Sn contents were formed in the SedEx mineralization and decomposed in the chlorite-apatite zone. By the thermal effect of the chlorite-apatite zone, the In-bearing sphalerite 1 decomposed into a mixture of In sakuraiite exsolution lamellae and **sphalerite 2** $(Zn_{0.89}Fe_{0.11})S$ (Fig. 16c). In addition to the lamellae, In sakuraiite also forms single grains up to 20 μm in size. These grains, usually having hypidiomorphic shape, are most commonly found at the rim of chalcopyrite, always in a quartz matrix. In sakuraiite inclusions are also rarely found in pyrite 1 cracks (Figs. 16d–f). The indium content ranges from 10.78 to 25.83 wt. % in both of these In sakuraiite modes (Tab. 10). The formation of lamellae represents the thermal decomposition of unstable sphalerite 1 in situ, but the second mode produces the partial and/or

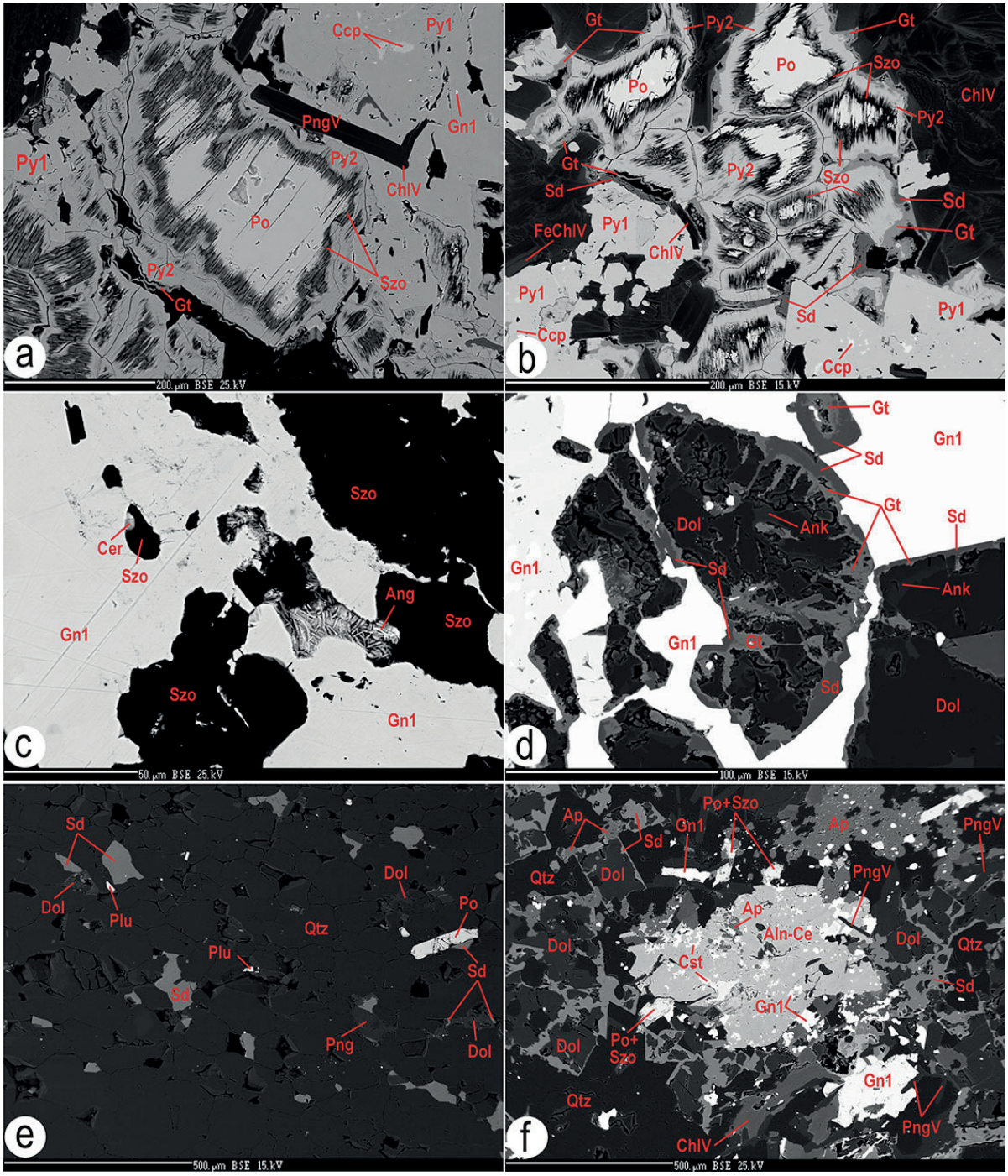

Fig. 11. Decomposition of the SedEx pyrrhotite (Po), galena 1 (Gn1) and pyrite 1 (Py1) by oxidation and dolomite (Dol) replacement by goethite (Gt), ankerite (Ank) and siderite (Sd) in the chlorite-apatite zone. ***a*** – Decomposition of pyrrhotite into szomolnokite (Szo), pyrite 2 (Py2) and goethite (Gt). Galena 1 (Gn1) and chalcopyrite (Ccp) inclusions in the host pyrite 1. The V-rich mica – phengite (PngV) and V-rich chlorite (ChlV) were formed between pyrite 1 and the pyrrhotite remnant. ***b*** – Gradual decomposition of the pyrrhotite aggregate by oxidation to form szomolnokite, pyrite 2, goethite and siderite according to the reaction 8, see text. The pyrite 1 contains chalcopyrite inclusions and the matrix consists of V-rich chlorite (ChlV) and V-Fe-rich chlorite (FeChlV). ***c*** – Galena 1 partially decomposed to form cerussite (Cer), anglesite (Ang) and pyrrhotite was completely replaced by szomolnokite. ***d*** – The remnant of the Silurian limestone – dolomite encloses with galena 1. The dolomite is gradually replaced by goethite, ankerite (Ank) and finally by the siderite (Sd) according to the reaction 9, see text. ***e*** – Dolomite and pyrrhotite remnants together with siderite and plumosite-like (Plu) formation in quartz matrix. ***f*** – The aggregate of allanite-*Ce* (Aln-Ce), cassiterite (Cst), fluorapatite (Ap), V-rich mica and galena 1 are found in a matrix consisting of dolomite remnants, quartz, V-rich mica, V-rich chlorite and fluorapatite. The rim of dolomite is replaced by siderite and pyrrhotite was decomposed to the szomolnokite (Po + Szo). BSE images of mineral assemglages.

complete decomposition of Sn(±In) sakuraiite and In-rich ferrokesterite by oxidation in the chlorite-apatite zone. This decomposition resulted in the indium transport by the fluid phase, away from the source minerals to form new In sakuraiite in the quartz matrix, according to reactions 16 and 17.

Temperature of chlorite-apatite zone

$$8Zn_{0.84\text{-}0.79}Fe_{0.11\text{-}0.13}Cu_{0.023}In_{0.023}S \rightarrow$$
Sphalerite 1

$$(Zn_{0.45}Fe_{0.19}Cu_{0.18}In_{0.18})S + 7Zn_{0.89}Fe_{0.11}S \quad (16)$$
In Sakuraiite – *lamellae in* Sphalerite 2

$$7(Cu_{0.34}Zn_{0.25}Fe_{0.22}Sn_{0.15}In_{0.05})S + FeS + H_2O + 0.5O_2 \rightarrow$$
Sn sakuraiite Pyrrhotite

$$2(Zn_{0.43}Fe_{0.22}Cu_{0.19}In_{0.18})S +$$
In sakuraiite

$$+ 2CuFeS_2 + SnO_2 + (Zn_{0.90}Fe_{0.10})S + H_2S \quad (17)$$
Chalcopyrite Cassiterite Sphalerite 2

The Cu, Fe, Zn and In contents in the In sakuraiite – sphalerite 2 series are variable and can be evaluated according to binary *apfu*-chemical plots in comparison to the sphalerite 1 created in the SedEx process (Fig. 5). For this comparison, the chemical formula of In sakuraiite was calculated to ZnS-sphalerite base in accordance with the crystalline structure of sakuraiite (Kissin & Owens, 1986). In In-rich sakuraiite, the indium content progressively correlates with Cu in the ideal In = Cu function of values from 0.1 to 0.25 *apfu*. This diagram shows the progressive In = Cu correlation trend that is also the same in sphalerite 1 with In = Cu values up to 0.08 *apfu* (Fig. 9a). The finding of an identical In = Cu correlation in former sphalerite 1 and in new In sakuraiite shows the preservation of the In = Cu function from the source sphalerite 1. This inherited In = Cu correlation does not change in In sakuraiite, which was formed by the decomposition of sphalerite 1 in the chlorite-apatite zone, and quantifies the content of the roquesite molecule ranging from 18.5 to 48.4 mol. % in In sakuraiite (Tab. 10). The sum of Cu + In *apfu* also progressively correlates with Fe, but the Fe content has a negative correlation with Zn and the coupled (CuInFe) ↔ Zn substitution was found in all samples from the source sphalerite 1 to new sphalerite 2 and In sakuraiite respectively (Fig. 9). The highest indium content in the In sakuraiite analyses is about 25.83 wt. % and their recalculation showed a more accurate arrangement of the elements in the chemical formula $(Zn,Fe)_2InCuS_4$ of that In sakuraiite based on 8 atoms.

The relationships between the source set of In-rich SedEx minerals, which are sphalerite 1, Sn sakuraiite, ferrokesterite and a newly formed association, such as sphalerite 2, In sakuraiite, cassiterite, show (CuSnFe) ↔ Zn and (CuInFe) ↔ Zn, as two independent substitution trends in the ZnFeCuSnIn system, where the composition planes between end members show reactions 13, 16 and 17. Evaluation of these independent substitutions reveals the relationship of the original (CuSnFe) ↔ Zn substitution created in Sn-rich sulfides with variable amounts of indium and the new In sakuraiite mineralization represented by the (CuInFe) ↔ Zn substitution, which originated by the decomposition of Sn-rich sulfides (± In) in the chlorite-apatite zone (Fig. 17).

Cu/Ag-rich tetrahedrite successive formation

The formation of tetrahedrite is closely related to the increasing content of Ag from the core to the rim of the tetrahedrite grains and aggregates (Fig. 18b). Tetrahedrites are found on SedEx sulfide remnants such as gudmundite, stephanite, chalcopyrite, galena 1 and are always associated with cassiterite, V-rich mica and siderite in the quartz matrix (Fig. 18). The core of tetrahedrite aggregates consists of **tetrahedrite 1** $Cu_7Ag_3Sb_4(FeZn)_2S_{13}$, where the Ag content ranges from 15.89 to 26.97 wt. % and its mineral formula is based on 29 atoms. It is tetrahedrite-*(Fe)* with a detailed chemical formula $Cu_6(Ag_{2.68\text{-}3.51}Cu_{0.35\text{-}1.34}Fe^{3+}_{0\text{-}0.11})_{3.90\text{-}4.02}(Fe^{2+}_{1.64\text{-}1.71}Zn_{0.29\text{-}0.36})_2Sb_{3.96\text{-}4.07}S_{12.95\text{-}13.05}$

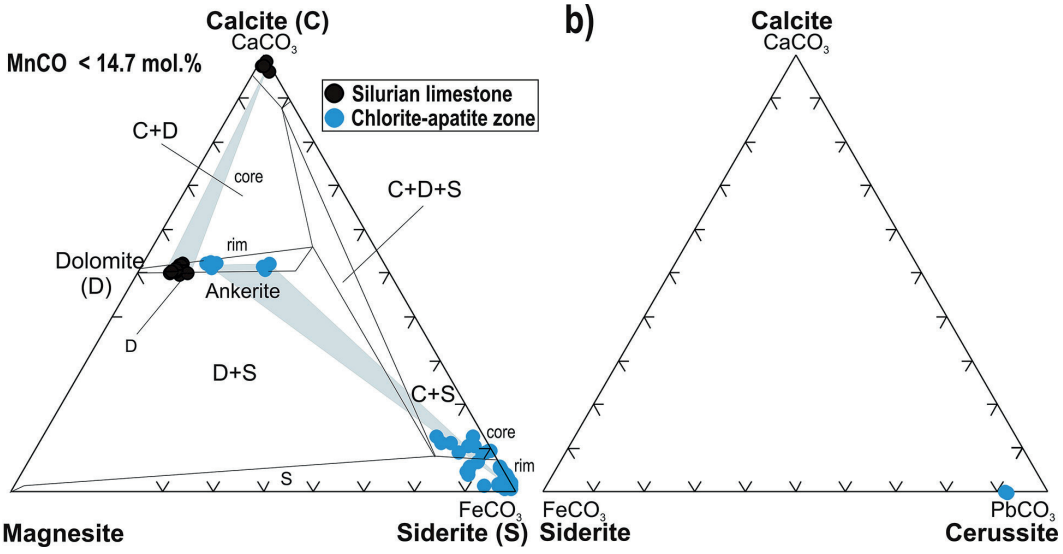

Fig. 12. Classification of carbonates. ***a*** – The triangular diagram shows the carbonate phase system and the projection of dolomite and calcite from the Silurian limestone layer of the Holec Beds. Composition of ankerite and siderite pair from the chlorite-apatite zone. ***b*** – Composition of cerrusite formed by the oxidation of galena 1 in the chlorite-apatite zone.

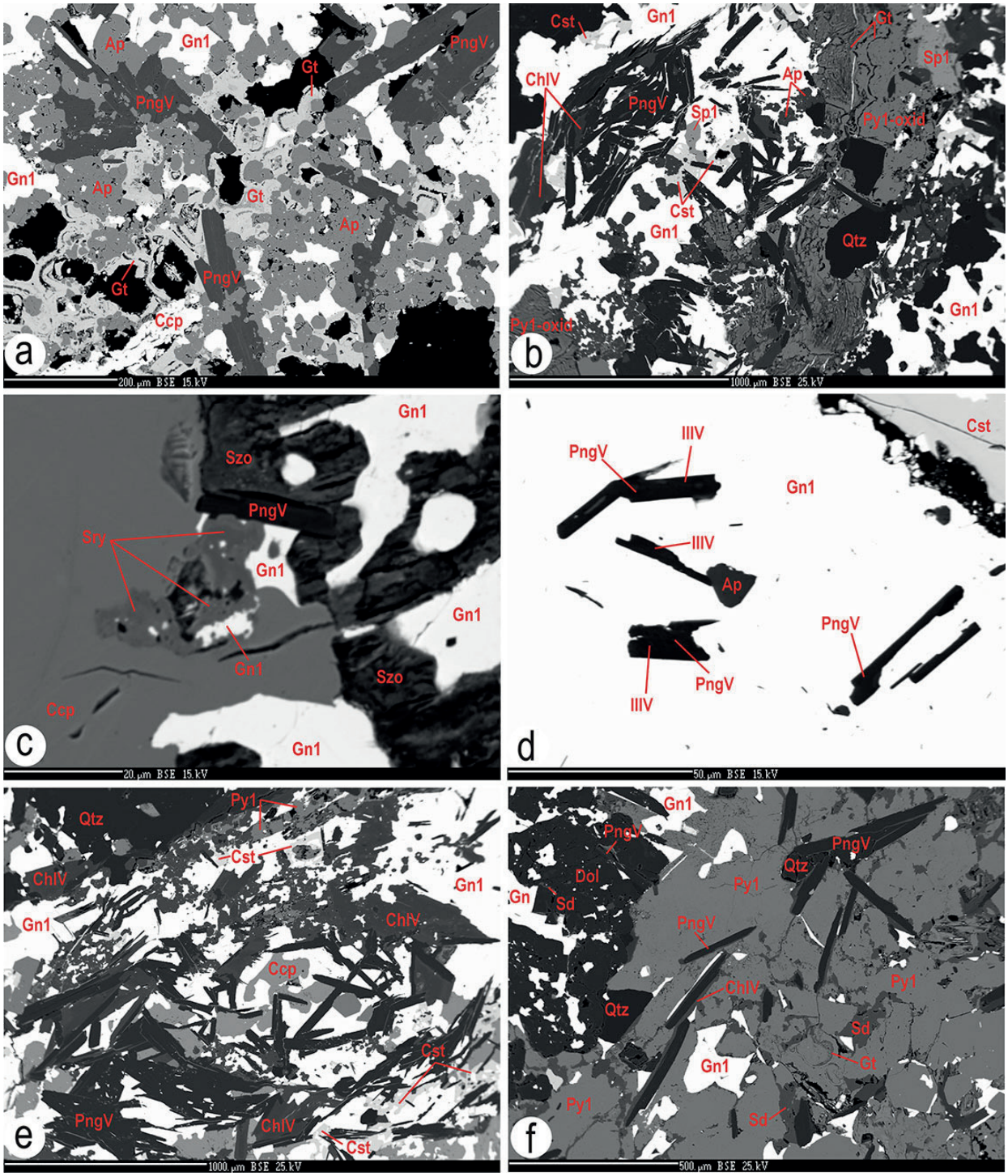

Fig. 13. Formation of V-rich micas (PngV), V-rich chlorite (ChlV), schreyerite and oxidation of SedEx sulfides in the chlorite-apatite zone. ***a*** – The relationship of euhedral V-rich mica, goethite (Gt), apatite (Ap) in the chalcopyrite (Ccp), quartz (Qtz) and galena 1 (Gn1) matrix. ***b*** – The aggregate consists of galena 1, oxidized pyrite 1 (Py1-oxide), goethite, V-rich mica, V-rich chlorite, fluorapatite, sphalerite 1 (Sp1) and cassiterite (Cst). ***c*** – Schreyerite (Sry) and galena 1 in host chalcopyrite (Ccp). That aggregate occurs with the contact with szomolnokite (Szo) and V-rich mica. ***d*** – The euhedral white micas are composed of V-rich muscovite-phengite and V-rich phengite-illite (IIIV) and these white micas with fluorapatite and cassiterite occur in galena 1. ***e*** – The quartz, chalcopyrite, pyrite 1 (Py1), cassiterite, V-rich micas and V-rich chlorite assemblage. ***f*** – Pyrite 1 aggregate was locally decomposed to goethite and siderite (Sd) by reactions 9 and 10, see text. The V-rich mica is surrounded by V-rich chlorite, and both were precipitated with quartz in host pyrite 1 and dolomite. Galena 1 is also present in pyrite 1. Dolomite is replaced by siderite and together with galena 1 form the matrix. BSE images of mineral assemblages.

according to classification of the tetrahedrite group (Biagioni et al., 2020). The inner rim 1 is formed by **tetrahedrite 2** $Ag_5Cu_5Sb_4(FeZn)_2S_{12}$ having the Ag content from 29.05 to 31.81 wt. % and its mineral formula is based on 28 atoms and shows kenoargentotetrahedrite-*(Fe)* $(Ag_{4.93\text{-}5.44}Cu_{0.56\text{-}1.07})_6(Ag_{3.83}Fe^{3+}_{0.09\text{-}0.13})_{3.93\text{-}3.96}(Fe^{2+}_{1.76\text{-}1.78}Zn_{0.22\text{-}0.24})_2Sb_{4.01\text{-}4.07}S_{11.96\text{-}12.04}$. The outer rim 2 in contact with the matrix forms rare **tetrahedrite 3** $Ag_9CuSb_4Fe_2S_{13}$ with the highest Ag content in the range from 42.45 to 49.26 wt. % and its mineral formula is based on 29 atoms and shows rozhdestvenskayite-*(Fe)* $Ag_6(Ag_{2.27\text{-}3.21}Cu_{0.69\text{-}1.71}Fe^{3+}_{0\text{-}0.17})_{3.91\text{-}4.15}(Fe^{2+}_{1.70\text{-}1.75}Zn_{0.25\text{-}0.31})_2Sb_{4.02\text{-}4.05}S_{12.80\text{-}12.98}$. In all three formulae of tetrahedrites, the Ag *apfu* content substitutes Cu in the sum of Cu + Ag = 10, Zn substitutes Fe^{2+} in the sum Fe^{2+} + Zn = 2, the excess Fe above 2 is Fe^{3+} and Sb content is uniformly 4 (Tab. 6).

Decomposition and oxidation in the chlorite-apatite zone of the original SedEx association of stephanite, gudmundite and ferrokesterite by the fluid phase resulted in the formation of tetrahedrite 1 to 3, cassiterite and siderite formation according to reaction 18. The increasing contents of Ag in tetrahedrite 1 to 3 from core to rim 2 in the tetrahedron projection of Ag-Sb-Fe-Cu system shows the immiscible gaps of tetrahedrites in the linear ordering of their composition and also shows the projection plane of reaction 18 between end members stephanite, gudmundite and ferrokesterite (Fig. 21).

$$\underset{\text{Stephanite}}{Ag_5SbS_4} + 3FeSbS + \underset{\text{Gudmundite}}{3Cu_2FeSnS_4} + 6H_2O + 5O + \underset{\text{Ferrokesterite}}{} + 5CO_2 \rightarrow \underset{\text{Tetrahedrite}}{Cu_6Ag_5Sb_4FeS_{13}} + \underset{\text{Cassiterite}}{3SnO_2} + 5FeCO_3 + 6H_2S \quad (18)$$

Bournonite and plumosite-like formation

Irregular **bournonite** $Pb_{0.98\text{-}0.99}Cu_{0.98\text{-}0.99}Sb_{0.94\text{-}0.96}Fe_{0.05\text{-}0.06}As_{0.04}S_{2.98\text{-}2.99}$ with a size of up to 20 μm is always occurring on galena 1. Together with galena 1, it occurs in association with cassiterite and siderite in the quartz matrix (Fig. 14c). Bournonite is homogeneous, containing Fe from 0.59 to 0.65 wt. % and As from 0.64 to 0.69 wt. % (Tab. 6). Rare **plumosite-like** $Pb_{2.78}Fe_{0.06}Bi_{0.02}As_{0.08}Sb_{3.09}S_{6.96}$ in similar size and position to the bournonite also occurs in the quartz matrix along with chalcopyrite, In sakuraiite, cassiterite, galena 1 and siderite (Fig.11e). The Fe and As contents in the plumosite-like chemical formula point to its common origin with bournonite. Both were formed by oxidation and decomposition of galena 1, gudmundite, and ferrokesterite in the chlorite apatite zone according to reaction 19 (Fig. 21).

$$\underset{\text{Galena1}}{4PbS} + 4FeSbS + \underset{\text{Gudmundite}}{Cu_2FeSnS_4} + H_2O + 4O_2\ 3CO_2 \rightarrow \underset{\text{Ferrokesterite}}{} \underset{\text{Bournonite}}{PbCuSbS_3} + \underset{\text{Plumosite-like}}{Pb_3Sb_3S_7} + \underset{\text{Chalcopyrite}}{CuFeS_2} + \underset{\text{Cassiterite}}{SnO_2} + 3FeCO_3 + \underset{\text{Goethite}}{2FeO(OH)} \quad (19)$$

PbSbBi-rich sufide, native Bi 2 and Se-rich galena 2 formation

The **PbSbBi-rich sulfide** $(Pb_{1.70\text{-}1.86}Cu_{0.14\text{-}0.31}Ag_{0.02\text{-}0.04})_{1.91\text{-}2.05}(Sb_{1.42\text{-}1.46}Fe^{3+}_{0.37\text{-}0.83}Bi_{0.84\text{-}1.13})_{2.95\text{-}3.09}(Se_{0\text{-}0.13}S_{5.90\text{-}5.99})_{5.95\text{-}6.08}$, in general $A_2B_3S_6$-type, **S-rich wittite** $(Bi_{3.61}Fe_{0.14}Sb_{0.07}Cu_{0.06}Ag_{0.04}Sn_{0.01})_{3.93}Pb_{3.01}(Se_{0.41}S_{8.65})_{9.06}$, **native Bi 2** $(Bi_{0.56}Sb_{0.09}Fe_{0.07}Pb_{0.08}Cu_{0.01}S_{0.19})$ and Se-rich **galena 2** $(Pb_{0.83\text{-}0.85}Fe_{0.08\text{-}0.10}Bi_{0.03\text{-}0.05}Sb_{0\text{-}0.03}Cu_{0\text{-}0.01}Ag_{0\text{-}0.01})(Se_{0.03\text{-}0.10}S_{0.90\text{-}0.99})$ are new minerals formed in chlorite-apatite zone (Fig. 19, Tab. 4). This assemblage originated from the decomposition of original PbBiSb-rich sulfide ($A_2B_2S_5$-type), kobellite and bismuthinite 1, which were formed by the SedEx process.

The original SedEx kobellite has been oxidized in the chlorite-apatite zone and its rim has partially decomposed to the native Bi 2 of size a few mm. The native Bi 2 there always contains sulphur residues up to 5.5 wt. % and varying contents of Cu, Fe, Pb and Sb up to 10 wt. %, indicating a mixture with kobellite remnant. Comparing two generations of native Bi, according to their composition, the inclusions found in the kobellite core coexist with kobellite and are free of other elements content (Fig. 19a, Tab. 4).

The original PbBiSb-rich SedEx sulfide ($A_2B_2S_5$ type) was partially decomposed and replaced by the Se-rich galena 2, bismuthinite 2 and respectively by the wittite and galena 2 that are found in albite and/or in the host pyrrhotite (Fig. 19c–d). Its decomposition is illustrated by reactions 20 and 21. The reactions plane is shown by the projection between the end-members in the Bi-Sb-Fe-Pb tetrahedron (Fig. 21). The generated wittite shows good agreement with the reference wittite and/or eclarite in the classification diagrams (Figs. 20 and 21).

$$\underset{\text{PbSbBi sulfide}}{2Pb_2BiSbS_5} + 3H_2O \rightarrow \underset{\text{Bismuthinite 2}}{Bi_2S_3} + \underset{\text{Galena 2}}{4PbS} + \underset{\text{Valentinite}}{Sb_2O_3} + 3H_2S \quad (20)$$

$$\underset{\text{PbSbBi sulfide}}{4Pb_2BiSbS_5} + 6H_2O \rightarrow \underset{\text{Wittite}}{Bi_4Pb_3S_9} + \underset{\text{Galena 2}}{5PbS} + 2Sb_2O_3 + 6H_2S \quad (21)$$

The new PbSbBi-rich sulfide ($A_2B_3X_6$-type) formed in chlorite-apatite zone up to 50 μm in size fills cracks in host pyrite 1 and chalcopyrite along with cassiterite (Fig. 19e–f). Plotting *apfu* compositions of Fe_{total} versus Bi and Fe_{total} versus Sb show inverse correlations and well defines the substitution $Sb + Fe^{3+} \leftrightarrow Pb + Cu + Ag$ at approximately the constant Bi about 1 (*apfu*) if Fe content ranges from 2 to 5 wt.% in that PbSbBi sulfide (Figs. 20 d–e; Tab. 4). In this case the chemical formula is $(Pb_{1.70\text{-}1.86}Cu_{0.14\text{-}0.31}Ag_{0.02\text{-}0.04})_{1.91\text{-}2.05}(Sb_{1.42\text{-}1.46}Fe^{3+}_{0.37\text{-}0.83})_{1.83\text{-}2.25}Bi_{0.84\text{-}1.13}(Se_{0\text{-}0.13}S_{5.90\text{-}5.99})_{5.95\text{-}6.08}$ as $A_2(B_2 + Bi)_3X_6$-type in detail. If Fe content ranges from 5 to more of 6 wt. %, the chemical formula changes to $(Pb_{1.56\text{-}1.64}Cu_{0.13\text{-}0.18}Ag_{0.02\text{-}0.03})_{1.71\text{-}1.85}$

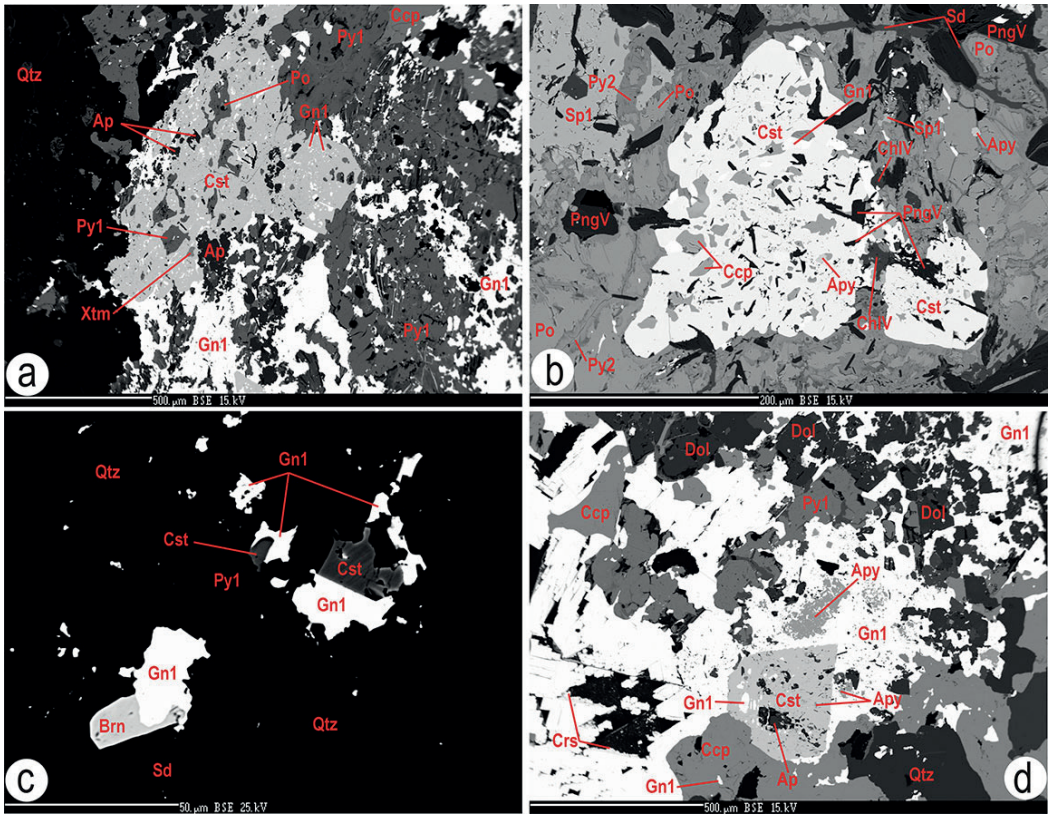

Fig. 14. ***a, b*** – Stratiform SedEx mineralization, such as galena 1 (Gn1), pyrrhotite (Po), xenotime (Xmt), pyrite 1 (Py1), chalcopyrite (Ccp), arsenopyrite (Apy), is cemented by cassiterite in aggregate, where V-rich mica-phengite (PngV), V-rich chlorite (ChlV) and fluorapatite (Ap) coexist with cassiterite. The matrix of the aggregate consists of quartz (Qtz), sphalerite (Sp1), pyrrhotite (Po), pyrite 1 and siderite (Sd). The pyrrhotite is replaced by pytite 2 (Py2). ***c*** – Galena 1 is partially replaced by bournonite (Brn) and cassiterite forming an aggregate with galena 1 in the quartz (Qtz) siderite (Sd) matrix. ***d*** – Assemblage of pyrite 1, pyrrhotite, quartz, arsenopyrite (Apy), chalcopyrite, galena 1, dolomite and hypidiomorphic cassiterite. Cassiterite closes arsenopyrite, galena 1, fluorapatite and the galena 1 rim is partially replaced by cerussite (Cer). BSE images of mineral assemglages.

$(Sb_{1.22-1.36}Bi_{0.84-0.95})_{2.06-2.31}Fe_{0.94-1.02}(Se_{0.08}S_{5.92})_6$ as $A_2(B_2 + Fe)_3X_6$-type in details. The high Fe in the chemical formula shows a depletion in A_2 of about 0.3 and an excess in B_2 of about 0.3, indicating a possible binding of the Fe content as Fe^{2+} around 0.3 *apfu* in A_2 according to the presented $A_2B_3X_6$-type, although a substantial fraction of the Fe is bound in the form of Fe^{2+} and Fe^{3+}in that PbSbBi rich sulfde (Tab. 4).

In the Sb-Bi-Pb triangle diagram, the new PbSbBi-rich sulfide translates to a tintinaite-wittite/eclarite trend, but the significant influence of the gudmundite ($Fe^{3+}SbS$) molecule in its composition can be clearly seen in (Sb + Fe_{total})-Bi-(Pb + Cu + Ag) triangle diagram and in Bi-Sb-Fe-Pb tetrahedron projection (Figs. 20a–b and 21). The formation of PbSbBi-rich sulfide can be explained by reaction 22 and the reaction plane is shown by the projection of reacted end-members in the Bi-Sb-Fe-Pb tetrahedron (Fig. 21).

$$\underset{\text{Gudmundite}}{FeSbS} + \underset{\text{Bismuthinite1}}{Bi_2S_3} + \underset{\text{Galena1}}{2PbS} + \underset{\text{Pyrrhotite}}{FeS} + 2O_2 + H_2O \rightarrow \underset{\text{PbSbBi sulfide}}{Pb_2SbBiFeS_6} + \underset{\text{native}}{Bi} + \underset{\text{Szomolnokite}}{FeSO_4.H_2O} \quad (22)$$

Discussion

In the Permian epidote-amphibolite facies and the related chlorite-apatite zone the graphite was formed from organic matter in the graphite-bearing phyllites and also skarn from limestone lenses of the Silurian Holec Beds in the Bystrý potok locality. That conversion of organic matter to graphite and limestone to garnet-hedenbergite-epidote-amphibole skarn released significant amount of CO_2 from the sourse organic matter and limestone into the fluid phase (Figs. 1, 2, 3, 5, 16e). During graphite and skarn formation, in addition to CO_2, as well O_2, H_2O and H_3PO_4 were released and this fluid phase also transported V and Ca to the stratigraphically overlying Late Silurian-Devonian stratiform SedEx sulphide mineralization, where V-rich micas-phengites, fluorapatite, V-rich chlorite and rarely schreyerite formed in the original SedEx sulfide matrix (Fig. 13). Besides graphite-bearing phyllites and limestone also the lydite from the Holec Beds demonstrated to be the source of Si, P, Rb, Cu, Cr, Ni, Ba, Sc, V, Cd, Se, Ti, Si, Fe, Mg, U, Zn, Pb, Sb, Tl, Hf, HREE and CO_2 that were released into the fluid phase in the Permian metamorphism (Radvanec & Gonda, 2019). According to the geological map, the Holec Beds cover approximately 1/4–1/5 of the

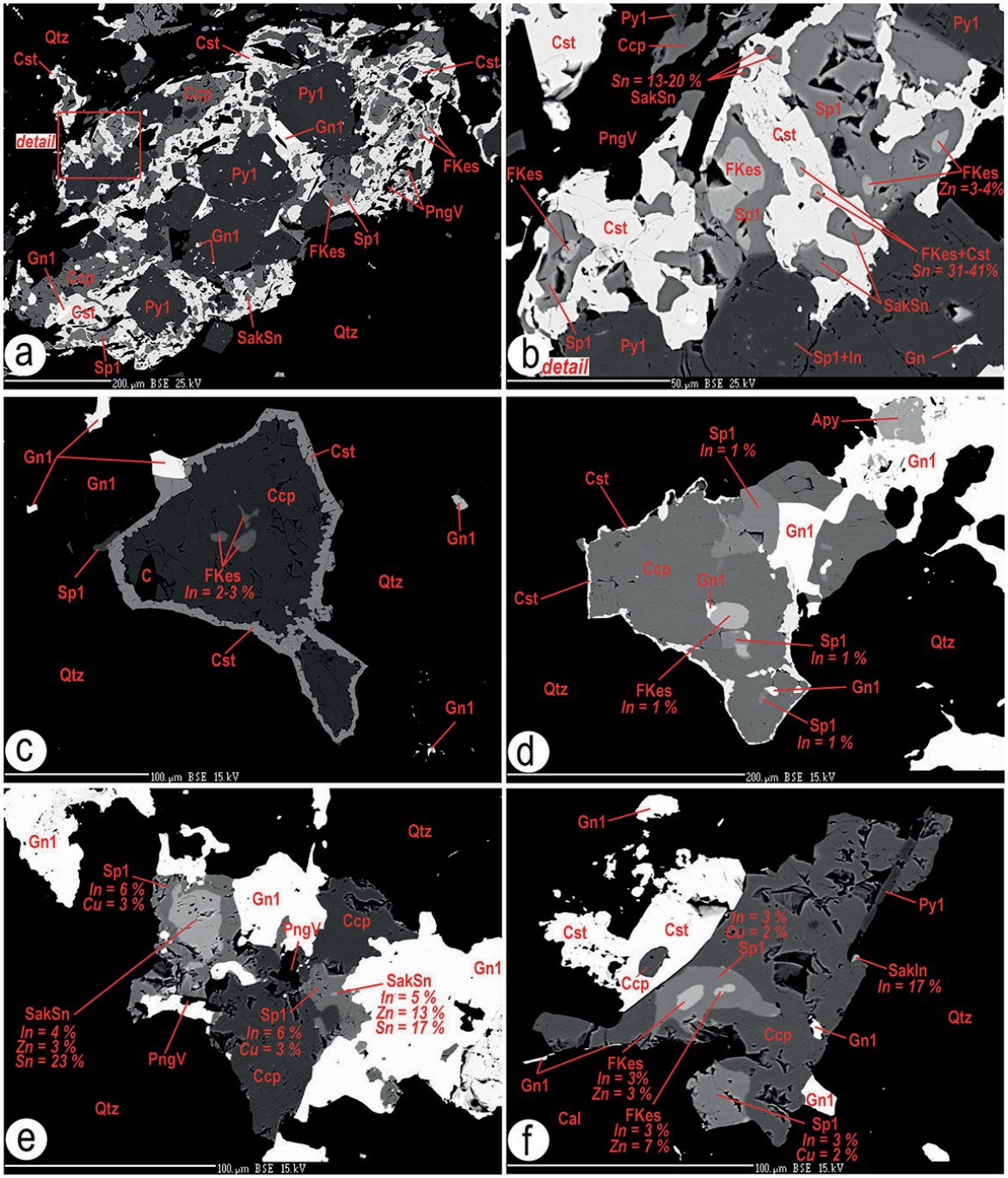

Fig. 15. ***a*** – Sulfides originated in the SedEx process, such as chalcopyrite (Ccp), pyrite 1 (Py1), galena 1 (Gn1), sphalerite 1 (Sp1), ferrokesterite (FKes), and Sn-rich sakuraiite (SakSn), are cemented by cassiterite (Cst) and V-rich mica-phengite (PngV) forming an aggregate in the quartz matrix (Qtz). ***b*** – The detail shows remnants of ferrokesterite and Sn-rich sakuraiite enclosed in the cassiterite aggregate. The disseminated inclusions of In-rich sphalerite 1 (Sp1 + In) and galena 1 occur in the host pyrite 1. The spots in cassiterite, where the Sn content ranges from 31 to 41 wt. % represents a mixture of unreacted ferrokesterite residues and new cassiterite (FKes + Cst). Analyses of these spots show a weak stoichiometry. ***c, d*** – The ferrokesterite with the In content from 1 to 3 wt. % was decomposed by oxidation to chalcopyrite and cassiterite according to the reaction 13, see text. The chalcopyrite encloses sphalerite 1, galena 1 and that chalcopyrite also contains residues of ferrokesterite and sphalerite 1 with the same content of In = 1 wt. %. Arsenopyrite (Apy) occurs in galena 1. ***e*** – The SedEx aggregate consists of variable Sn-rich sakuraiite, galena 1, chalcopyrite and sphalerite 1. The In content of the Sn-rich sakuraiite ranges from 4 to 6 wt. % and in sphalerite 1 the same amount of In = 6 % was found. ***f*** – The SedEx aggregate of Sn-rich sakuraiite, ferrokesterite, galena 1, chalcopyrite, cassiterite, pyrite 1 and sphalerite 1 in the quartz matrix with new cassiterite. The content of In = 3 wt. % is the same in ferrokesterite, Sn-rich sakuraiite and also in sphalerite 1. In-rich Sakuraiite (SakIn) was formed on the chalcopyrite. BSE images of mineral assemglages.

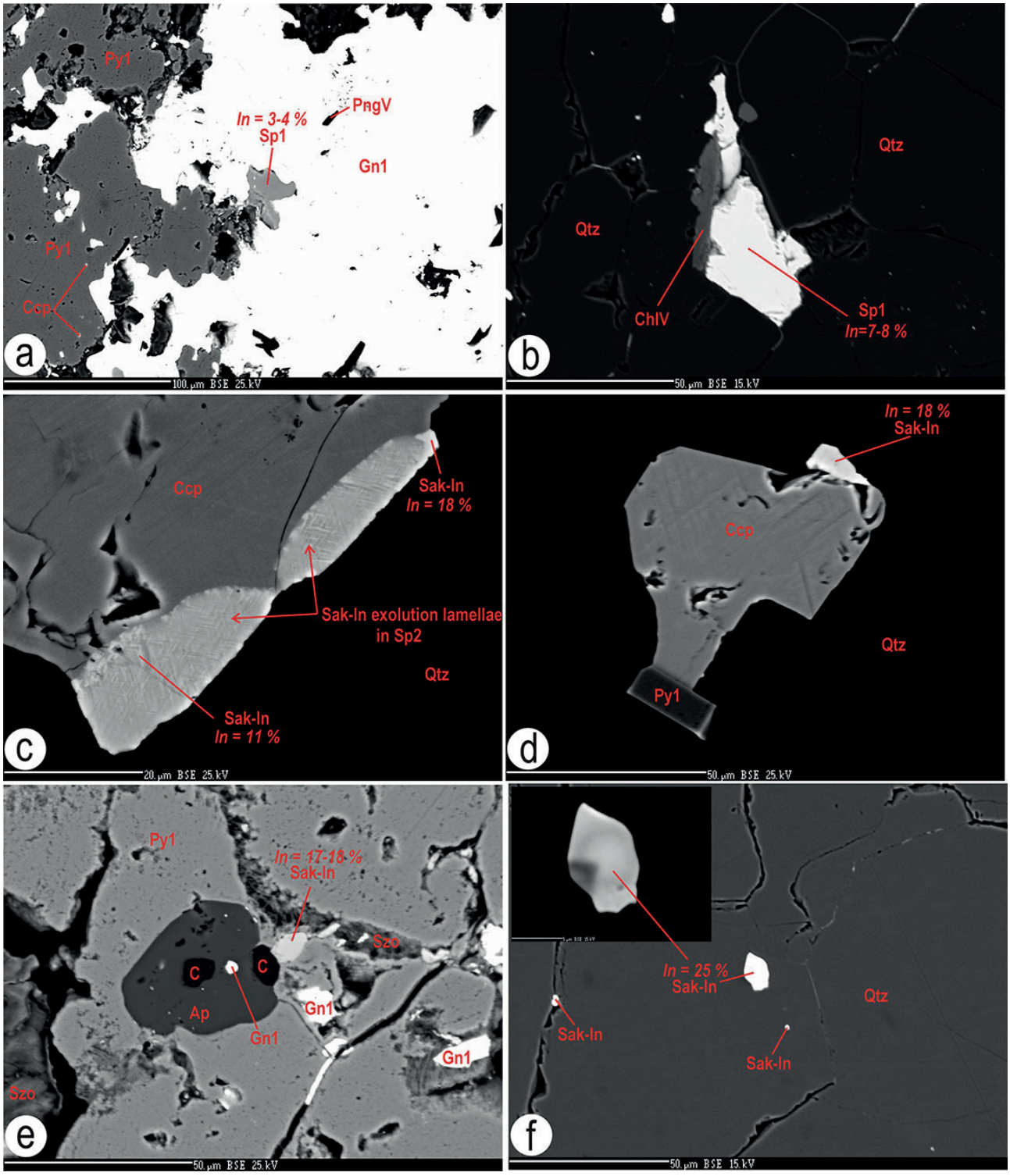

Fig. 16. The formation and occurrence of In-rich sulfides. ***a, b*** – In-rich sphalerite 1 originated and belongs to the mineral assemblage of the stratiform SedEx sulfidic mineralization. The In content in sphalerite 1 ranges from 3 to 8 wt. %. This sphalerite 1 is accompanied by pyrite 1 (Py1) with the chalcopyrite (Ccp) inclusions, by the V-rich mica (PngV), galena 1(Gn1), V-rich chlorite (ChlV) and by the quartz (Qtz). ***c*** – The In-rich sphalerite 1 (Sp1) decomposition caused the formation of In sakuraiite (InSak) lamellae in the indium-free sphalerite 2 (Sp2) according to reaction 16, see text. ***d*** – Homogeneous In-rich sakuraiite was formed on the rim of chalcopyrite. ***e*** – Host pyrite 1 (Py1) encloses graphite (C), fluorapatite (Ap), galena 1, szomolnokite (Szo) and In-rich sakuraiite there contains indium from 17 to 18 wt. %. ***f*** – In-rich sakuraiite with indium content of 25 wt. % in the quartz matrix. BSE images of mineral assemblages.

entire area in the Gemeric unit and this area of occurrence with Permian metamorphism shows release of CO_2 and elements into the fluid phase during the considerable regional extent of Variscan orogeny (Figs. 1–3).

The released fluid phase decomposed and oxidized the original stratiform SedEx sulfides in the chlorite-apatite zone, which partially coincides with the epidote-amphibolite facies (500–600 °C; 526–546 °C; 3–7 kbar) in the Bystrý potok locality. That chlorite-apatite zone is identical to the P-T conditions of the chlorite-apatite zone (420–540 °C) found throughout the Gemeric unit (Radvanec & Gonda, 2019, 2020).

The fluid phase that formed at these P-T conditions consists of CO_2, O_2, H_2O, H_3PO_4, obtained from Holec Beds and moreover from H_2S and HF after enrichment of the fluid phase due to decomposition and oxidation of the SedEx sulfides according to 22 empirical reactions. All reactions are derived from the relationships between the reactants and the newly formed mineral associations based on their relationships confirmed by BSE images (Figs. 4, 6–8, 11, 13–16, 18, 19). The resulting reactions explain the formation of new cassiterite, valentinite, anglesite, schreyerite, szomolnokite, goethite, V-rich mica, V-rich chlorite, Fe-Mn-Pb carbonates, and new generation of In-Sn-Ag-Sb-Pb-Bi-Zn-Fe-As-Cu-Ni-Co sulfides at the expense of the original SedEx mineralization in the crystallization systems were the oxidation is the main process formed those new minerals in situ (Figs. 5, 12, 17, 21).

The present study and previously published data point to oxidation as the main decomposition process of Lower Paleozoic rocks by fluid phase originated in Permian metamorphism. The epidote-amphibolite facies with a related chlorite-apatite zone represent the lower

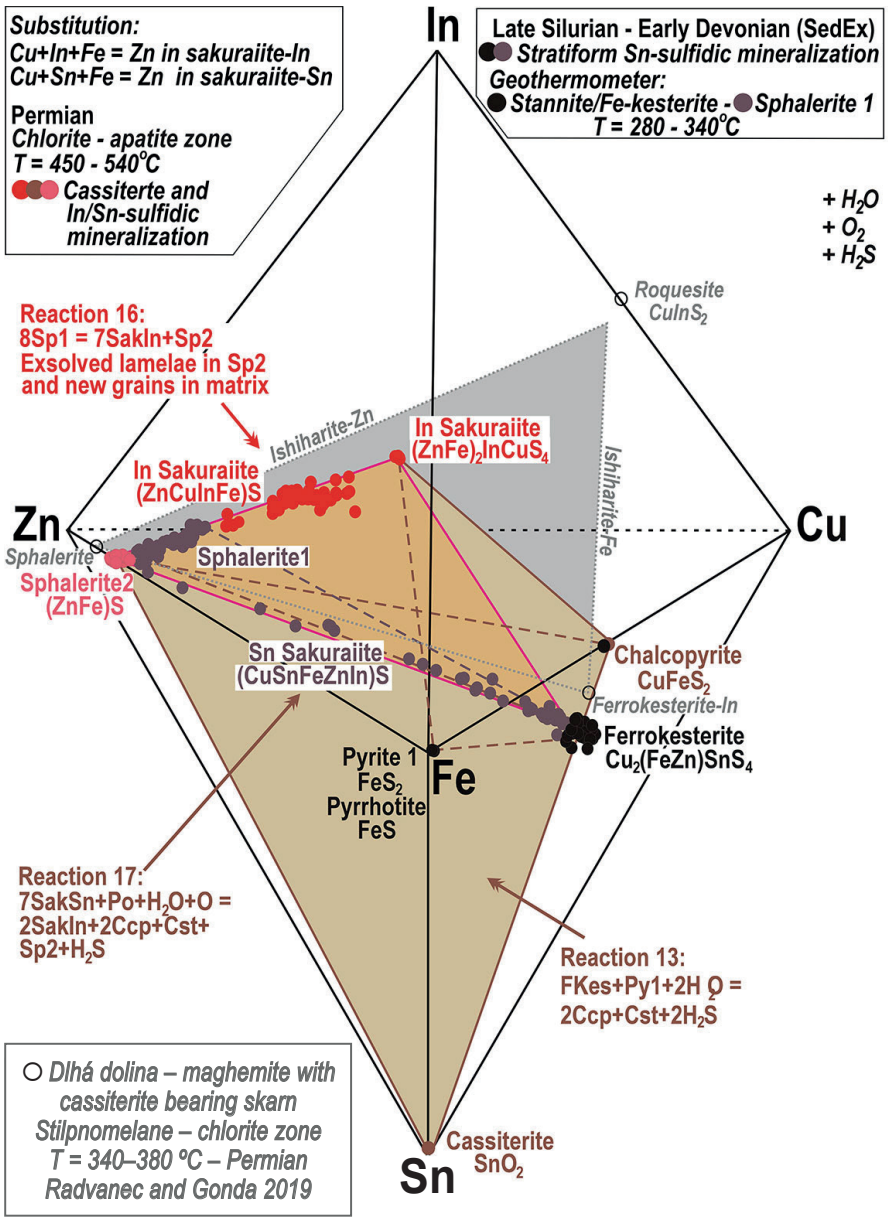

Fig. 17. Two interconnected tetrahedral phase diagrams for the system ZnFeCuSnIn, showing the plotting positions of the sphalerite 1 (Sp1), sphalerite 2 (Sp2), Sn-rich sakuraiite (SakSn), In-rich sakuraiite (SakIn), chalcopyrite (Ccp), ferrokesterite (FKes), pyrite 1 (Py1), pyrrhotite (Po), and cassiterite (Cst). The composition planes showing reactions 13, 16 and 17 see the text. The studied In-Sn mineralization is compared with sphalerite, ishiharaite-*Zn*, ishiharaite-*Fe*, roquesite and In-rich ferrokesterite-*In* mineralization from the maghemite-cassiterite skarn at the Dlhá dolina locality described by Radvanec & Gonda (2019).

temperature limit (420–540 °C) for the presence of in situ oxidation. Not only the epidote-amphibolite facies and the related chlorite-apatite zone, but also the temperature 600–650 °C of the amphibolite facies and/or the biotite zone show the oxidation as the main decomposition process of the source minerals, as evidenced by the formation of Fe-Mn skarns with Fe-Mn oxides at the Čučma locality (Radvanec & Gonda, 2020).

The upper temperature part of the amphibolite facies in the Gemeric unit, with above 650 °C, caused anatectic melting of all Lower Paleozoic rocks on two Permian metamorphic hot lines. Anatectic melting on the hot lines produced granitic magma and part of it also differentiated to form varieties of S-type granites with $^{87}Sr/^{86}Sr$ ratios ranging from 0.7110 to 0.7142 (Radvanec et al., 2004, 2007, 2009; Grecula et al., 2009, 2011).

Based on this study and published data, the chlorite-apatite zone, epidote-amphibolite facies and biotite zone with proven anatectic melting are those facies in the Gemeric unit, where oxidation in the Permian is the main decomposition process of minerals found in the Lover Paleozoic rocks, including the Late Silurian-Devonian stratiform SedEx sulfidic mineralization (Radvanec et al., 2004, 2010; Radvanec & Gonda, 2019, 2020).

Within the Holec Beds of Gemerc unit, the stratiform SedEx sulfide mineralization represents a significant occurrence (Figs. 1, 2) and its decomposition owing to its metamorphic overprint in zones and facies mentioned above, including its anatectic melting, released Fe, Cu, Sb, Ag, Pb, Zn, In, Bi As, Ni, Co, V, Ca and Sn into the fluid phase. The same elements, as well as B, F, Sn, Mo, K and Li were released into the fluid phase from SedEx mineralization in the Smolnik locality (Radvanec & Gonda, 2019). These elements were transported by the complex fluid phase rich in CO_2, O_2, H_2O, H_3PO_4, HS and H_2S to newly developed Variscan structures, ranging from greisen derivated by the granite magma in the amphibolite facies, skarns and stockwors in the epidote-amphibolite facies and/or in the chlorite-apatite zone to veins located in the greenschist facies. The Variscan structures are filled with oxides, sulfides and Fe-Mn-Mg carbonates, depending on the zones and/or conditions of the metamorphic facies in which the structure has formed (Radvanec et al., 2007, 2010; Radvanec & Gonda, 2019, 2020).

Concerning the sequence of Variscan tectonometamorphic events in papers referred above (l.c.), there were distinguished the Carboniferous-Lower Permian metamorphism **M1a** of Variscan **VD1** convergent / collisional phase (348–275 Ma) and (2) Middle-Upper Permian metamorphic overprint **M1b** (275–262 Ma; monazite and uraninite ages – Konečný in Radvanec et al., 2007) produced by the heat imput from the hot line and causing the active metamorphic core complex formation and related **VD2** uplift in the axial zone of collisional belt as well as related synmetamorphic and ongoing unroofing processes. In present concept of "XD labelling" (Németh, 2021) for better unification and understandability, the Carboniferous **VD1** related metamorphism **M1a** is designated **MV1 (348–275 Ma)** and Permian **VD2** related metamorphism **M1b** is designated **MV2 (275–262 Ma)**. This new designation is used also in this paper.

The **MV2** thermal processes and later Permian evolution contributed markedly to origin of orogen-parallel extensional fan-like structures with input of fluids, producing Permian mineralized veins.

The cassiterite is the index oxide in the metallogeny of the Gemeric unit. The main occurrence of cassiterite is related to cassiterite bearing greisen with the topaz, tourmaline, löllingite, fluorapatite, white mica, biotite, Bi-rich minerals, margarite, fluorite, molybdenite, uraninite Fe-Mn carbonates and siderite formation in the epidote-amphibolite facies and/or in the biotite zone (Hnilec locality) were the Re-Os age of molybdenite is ~ 263 Ma (Kohút & Stein, 2005). Less cassiterite occurs in the cassiterite-tourmaline-Fe carbonates bearing greisen of the chlorite-apatite zone (Dlhá dolina locality) and least in the maghemite-cassiterite-Fe carbonate/siderite-FeZnCuBiTeIn sulfides skarn formed in the stilpnomelane-chlorite zone (Dlhá dolina locality). The relationship and abundance of cassiterite formation show its consistently decreasing abundance in metamorphic facies and zones from greisen to skarn. The formation of cassiterite covers a temperature range from about 500–600 °C in greisen to 300–370 °C in skarn (Radvanec & Gonda, 2019). However, the data from present study explain the formation of cassiterite by oxidation of Sn-rich source sulfides in-situ under P-T conditions of the chlorite-apatite zone (420–540 °C) without the evidence of the greisen formation in the host stratiform SedEx mineralization. The oxidation of Sn-rich sufides in the epidote-amphibolite phase or decomposition of Sn-rich sulfides during anatectic melting in the amphibolite facies leads to the formation of cassiterite in situ, or cassiterite is formed in greisens as a part of granite apophyses or near the granite, or cassiterite is formed in skarn with maghemite. Data from this study confirm that the source of tin for cassiterite formation in greisen and skarn is Sn-rich sulfides from the Late Silurian-Devonian SedEx mineralization.

In addition to greisen and skarn mineralization, the short quartz veins and stockwork occurring near porphyritic, medium-grained S-type granites and in P-enriched leucogranites, originating at the Hnilec and Dlhá dolina localities, are considered to represent a root zone of the vein formation and the initial hydrothermal activity related to and dated to the Permian as well. Veins are generally up to 15 cm thick and up to 5 m long. They contain variable amounts of albite, muscovite, Li-bearing micas, chlorites, biotite, tourmaline, rutile, fluorite, polycrase-*(Y)* to uranopolycrase, uraninite, columbite-*(Mn,Ta,Fe)*, bastnäsite-*(Ce)*, carbonates (Mn-rich siderite, rhodochrosite, calcite and dolomite), phosphates (fluorapatite, triplite, xenotime, goyazite-*(REE)*, fluorarrojadite-*(Ba,Na)*, fluorarrojadite-*(Ba,Fe)*, fluordickinsonite-*(Ba,Na)*, viitaniemiite), molybdenite, tungstene, topaz, Bi, Bi-Te, Pb-Bi, Pb-Sb, Sb, As-Co-Ni sulfides and sulfides like pyrite, arsenopyrite, sphalerite, chalcopyrite, tetrahedrite, galena, etc. (Grecula et. al., 1995; Radvanec et al., 2019; Števko & Sejkora, 2021).

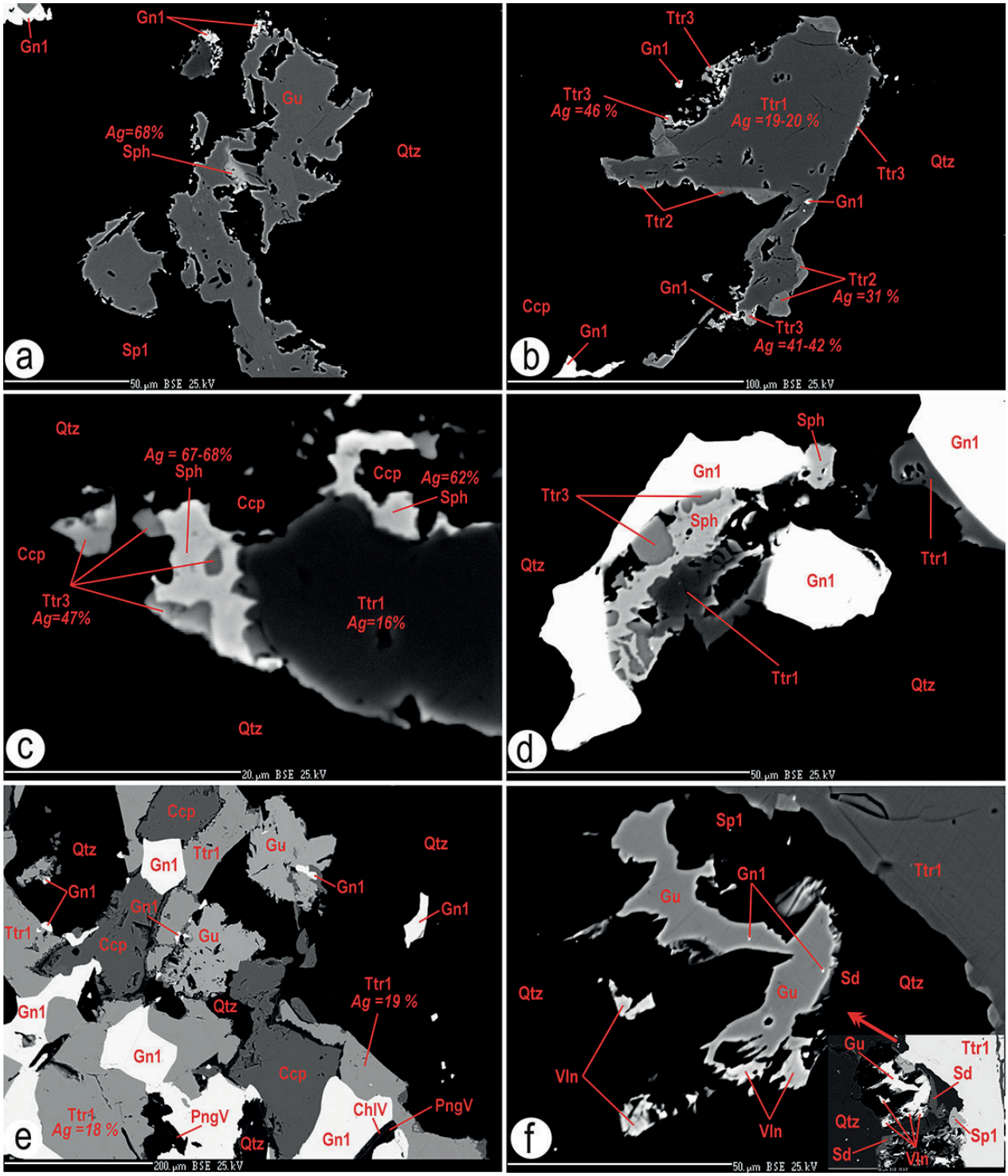

Fig. 18. The successive formation of Ag-rich sulfides. ***a*** – The corroded remnants of stephanite (Sph), gudmundite (Gu) and galena 1 (Gn1) occur in the matrix of quartz (Qtz). ***b*** – The gradual formation of tetrahedrites from tetrahedrite 1 (Tth1) in the core through tetrahedrite 2 (Tth2) at the rim 1 and final formation of tetrahedrite 3 (Tth3) at rim 2, showing a gradual increase in Ag content from core to the rim 2. The matrix consists of chalcopyrite (Ccp), quartz and galena 1. Zonal tetrahedrites were formed according to reaction 18, see text and Fig. 21. ***c, d*** – The relationship between stephanite, tetrahedrite 1 and tetrahedrite 3 in the quartz and chalcopyrite matrix. ***e*** – The corroded grains of gudmundite and their relationship to the quartz, galena 1, tetrahedrite 1, chalcopyrite, V-rich mica (PngV) and V-rich chlorite (ChlV). ***f*** – Gudmundite partially oxidized to valentinite (Vln) and siderite according to the reaction 15, see text. This gudmundite occurs in the association of tetrahedrite 1 (Tth1), sphalerite 1 (Sp1) and quartz (Qtz). BSE images of mineral assemblages.

The In-rich sakuraite is another index mineral occurring with cassiterite outside the greisen formation. In-rich sulfides associated with coexisting maghemite and cassiterite were formed in the stilpnomelane-chlorite zone in maghemite-cassiterite-Fe carbonate/siderite-FeZnCu-BiTeIn sulfides skarn in the Dlhá dolina locality (Radvanec & Gonda, 2019). There, in the immediate skarn contact with the calcite-ankerite-dolomite lens (former Silurian limestone), the chalcopyrite contains inclusions of ishiharaite-*(Fe)*, sakuraiite and sakuraiite-*(Zn)*. Inclusions of these In-rich sulfides are in chalcopyrite inhomogeneous and often form a mixture of In-rich sphalerite, sakuraiite and stilpnomelane or it is the mixture of In-rich sphalerite, sakuraiite-*(Zn)* and roquesite. Rarely the ishiharaite-*(Fe)* forms individual inclusions in host chalcopyrite (l.c.). These In-rich sulfides, coexisting with chalcopyrite and sphalerite, show crystallization from the fluid phase along with a maghemite-cassiterite-siderite matrix. In the Zn-FeCuInSn system, the In-rich sulfides exhibit a complete substitution series between the sphalerite-roquesite-In-rich ferrokesterite end-members, leading to the formation of ishiharaite-*(Zn),* ishiharaite-*(Fe)* and/or sakuraiite in the host chalcopyrite. All In-rich sulfides formed in the stilpnomelane-chlorite zone, where T = 300–370 °C and P = 4.3–5.7 kbar (Fig. 17; Radvanec & Gonda, 2019).

This study qualifies the formation of coexisting sphalerite 2 and In-rich sakuraiite in the chlorite-apatite zone with 520–540 °C at higher temperature. The sphalerite 2 and In-rich sakuraiite assemblage originated at the expense of the original In-rich sphalerite 1, Sn (± In) sakuraiite and In-rich ferrokesterite formed in stratiform SedEx mineralization (Figs. 9, 10 and 17). The formation of sphalerite 2 and In sakuraiite is accompanied by the formation of coexisting cassiterite and siderite as it is also in the stilpnomelane-chlorite zone. The different thermal formation of In-rich sulfides are also indicated by the Fe content in sphalerites where the Fe content ranges from 0.97 to 3.62 wt. % in sphalerite of the stilpnomelane-chlorite zone and sphalerite 2 formed at a higher temperature in the chlorite-apatite zone contains Fe ranging from 6.25 to 6.68 wt. % (Radvanec & Gonda, 2019; Tab. 10). The different temperatures of the chlorite-apatite and stilpnomelane-chlorite zones are also manifested by parallel projection planes between the end-members in the ZnFeCuInSn system (Fig. 17).

In addition to the stratiform SedEx sulfide mineralization, greisen, skarn, Mg-Fe-Mn metasomatic mineralization and stockwork mineralization, the siderite-sulfide veins represent the typical and predominant form of mineralization in the Gemeric unit, of which about 1 200 were verified, being located in greeschis facies (Grecula et al., 1995). The mineralization of the veins consists of siderite, ankerite, baryte, chalcopyrite, pyrite, quartz, as well as tetrahedrite, stibnite and sulfides rich in As, Sb, Pb, Bi, Co, Ni and others minerals. Present study data reveal a process whereby the fluid phase of the chlorite-apatite zone oxidized the original stratiform SedEx sulphide mineralization and its decomposition released elements that were subsequently locally transported. The higher temperature of the ore-bearing fluid associated with the amphibolite facies transported the released elements into the vein structures and caused vertical zonation from the quartz- and sulfide-dominated root zone to the siderite- and barite-dominated main vein structure (Grecula et al., 1995; Radvanec et al., 2004). The siderite always forms the central part and baryte only the upper part of vein mineralization in the Gemeric unit (Grecula et al., 1995). In the baryte the $^{87}Sr/^{86}Sr$ ratio ranges from 0.7104 to 0.7154 (Radvanec et al., 1990, 2004). At the Gemerská Poloma locality the magnesite has a ratio of $^{87}Sr/^{86}Sr = 0.71124 – 0.71148$. The $^{87}Sr/^{86}Sr$ data in baryte and magnesite agree well with the $^{87}Sr/^{86}Sr$ ratio ranges from 0.7119 to 0.7144 in the S-type Permian granite reflecting their simultaneous generation in the Variscan MV2 metamorphic-magmatic-hydrothermal (MMH) cycle (Radvanec et al., 2004, 2010; Žák et al., 2005; Radvanec & Gonda, 2019).

The siderite veins are dissected by faults and fissures and the individual vein segments often changed from E-W to NW-SE directions due to Alpine tectonic overprint (Radvanec et al., 1988). The vein structures were locally re-metamorphosed at most in greenschist facies which has rejuvenated the former mineralization. At the Gemerská Poloma locality a part of the magnesite body was converted to talk by a SiO_2-rich fluid phase in the Alpine ApD2 unroofing structures (Radvanec et al., 2010; Smolárik & Németh, 2015). At the Rudňany locality the celestine nests located in cracks in the momomineralic baryte and celestine found in cracks from the baryte and ankerite matrix have a ratio of $^{87}Sr/^{86}Sr = 0.721757–0.721893$. Also strontianite hemispheres with $^{87}Sr/^{86}Sr = 0.718536$ at a fracture in the host rock of the siderite-sulfide vein have $^{87}Sr/^{86}Sr$ values compared to these data in the celestine. The $^{87}Sr/^{86}Sr$ data for late-stage Sr minerals from siderite-sulfide veins are significantly higher than the range obtained by Radvanec et al. (1990, 2004) for main-stage baryte. The data on the formation of strontianite, celestine and talc, together with tectonic evolution, reflect a younger and rejuvenating hydrothermal phase of the Alpine metamorphism MAp2, which applies only locally, while the data on baryte, magnesite and granite reflect the main Variscan magmatic-metamorphic-hydrothermal (MMH) cycle in the Paleo-Gemeric domain (Radvanec et al., 2004).

The data from this study complete the genetic relationship between source Late Silurian-Devonian stratiform SedEx sulfidic mineralization and greisen-stockwork-skarns and siderite-sulfide mineralization localized in veins summarized the Permian (MMH) cycle in the Paleo-Gemeric domain (Grecula et al., 1995; Radvanec et al., 2010; Radvanec & Gonda, 2019, 2020). The genetic relationship between the source SedEx stratiform sulphide mineralization and the siderite-sulphide mineralization in veins is supported also by stable isotope data (Radvanec et al., 2004; Žák et al., 2005). The MMH cycle summarizes the genetic connection between mineralization, anatectic melting with the formation of S-type granites in the amphibolite facies and metamorphic facies ranging from epidote-amphibolite facies, biotite zone, chlorite-apatite zone, chlorite-stilpnomelane zone to chlo-

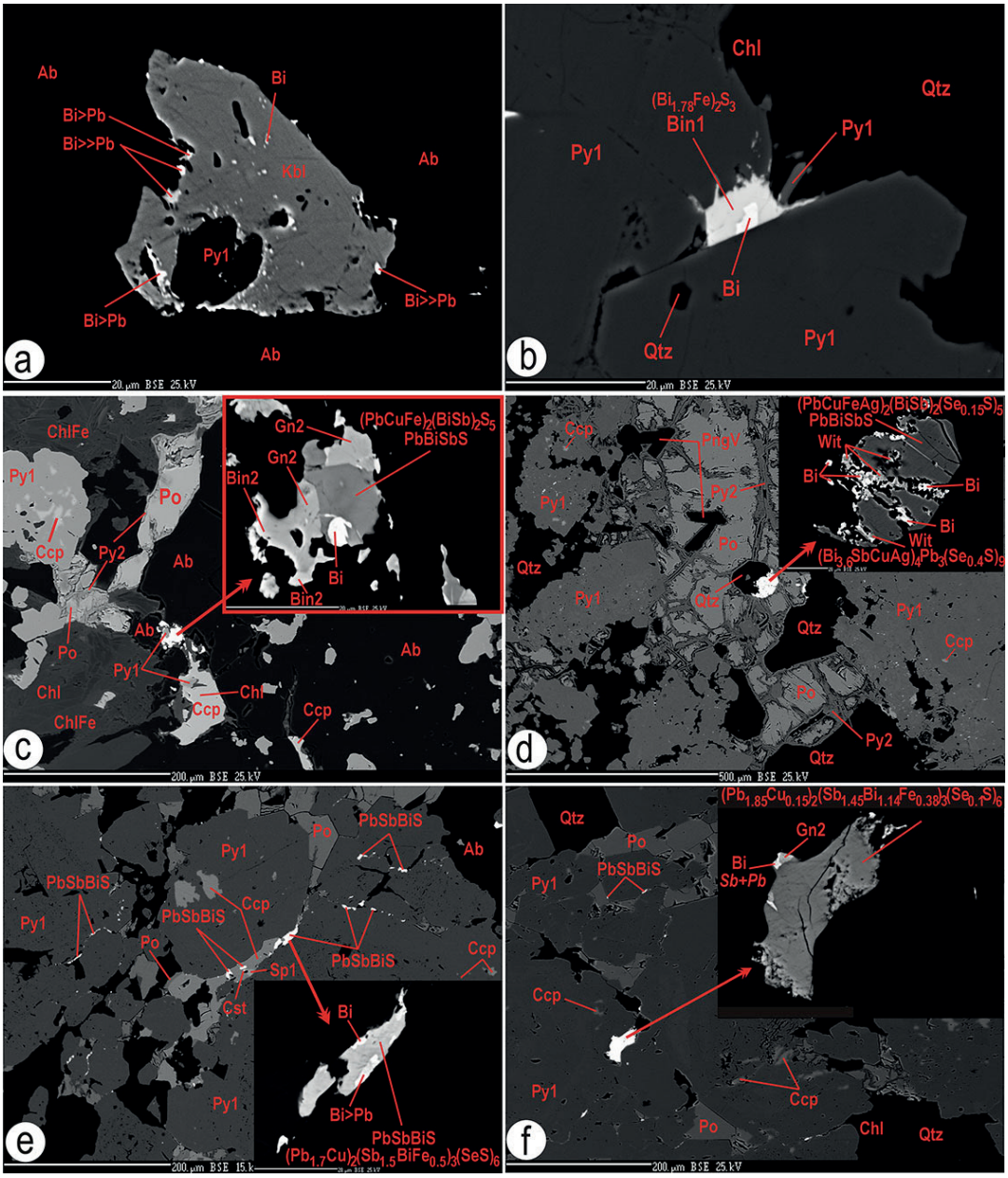

Fig. 19. The PbBiSb-rich and PbSbBi-rich sufides, bismuthinite, galena 2 and native Bi relationships in the Bystrý potok locality. ***a*** – Kobellite (Kbl) contains a number of native Bi (Bi) inclusions, and its rim was decomposed by oxidation in the chlorite-apatite zone into a mixture of native Bi-Pb-rich phase (Bi > Pb) with varying residual sulphur content. Kobellite was formed by the SedEx process together with pyrite 1 (Py1) in the albite (Ab) matrix. ***b*** – Bi bearing aggregate composed of bismuthinite 1 (Bin1) and native Bi in the pyrite 1, are regarded to be the SedEx mineral assemblage. ***c*** – Bi-rich sulfide aggregate in albite and the accompanying SedEx mineralization of the matrix consisting of chlorite (Chl), Fe-rich chlorite (FeChl), pyrite 1 with chalcopyrite (Ccp) inclusions. The pyrrhotite (Po) is replaced by pyrite 2 (Py2). The detail shows a composition of the aggregate, where the PbBiSb-rich sulfide with native Bi inclusions is replaced by selenium-rich galena 2 (Gn2) and bismuthinite 2 (Bin2) formed in the chlorite-apatite zone. ***d*** – The Bi-rich aggregate formed by the SedEx process closes the pyrrhotite. The matrix consists of pyrite 1 with chalcopyrite inclusions. In the pyrrhotite the V-rich mica (PngV) and quartz (Qtz) was formed and the rim of the pyrrhotite that is replaced by pyrite 2. The detail shows the decomposition of PbBiSb-rich sulfide (PbBiSbS) by chlorite-apatite zone into a mixture of wittite (Wit) and native Bi. ***e*** – Occurrence of chalcopyrite, cassiterite (Cst), sphalerite 1 (Sp1) pyrrhotite, albite and pyrite 1, where cracks in pyrite 1 are filled by new PbSbBi-rich sulfide (PbSbBiS). The detail shows the composition of the PbSbBi-rich sulfide, which is replaced by the native Bi at the rim and also by a mixture of BiPb-rich native phase (Bi > Pb) with different residual sulphur content. ***f*** – In crack of pyrite 1 the new PbSbBi-rich sulfide is accompanied by galena 2 and native Bi containing Pb and Sb (Sb + Pb). BSE images of mineral assemblages.

rite zone in the Permian regional metamorphism of the paleo-Gemeric unit (Grecula et al., 2009, 2011; Radvanec & Gonda, 2019, 2020). These facies and zones produced a fluid phase that contained and transported CO_2, O_2, H_2S, H_2O, HF, BO_3, HCl, H_3PO_4, K, Na, Ca, Al, Si, Fe, Mg, Mn, Sn, F, V, REE, U, Ti, Y, Cu, Sb, Te, Bi, Ag, Zn, In, Ta, Nb, Pb, Ni, Co and As into the structures, where, depending on where these structures originated, different mineralization has formed, ranging from high-temperature greisen and skarns in the amphibolite or in epidote-amphibolite facies to low-temperature veins in the chlorite zone (Radvanec & Gonda, 2019, 2020). The heat source for the Permian metamorphism and related mineralization was provided by the Variscan subduction zone, which created two hot lines in the upper crust of the Paleo-Gemeric unit. Anatectic melting of the upper crust and the formation of S-type granites with accompanying cassiterite mineralization in greisens and Mn skarns occurred in the amphibolite facies on these hot lines (Radvanec & Gonda, 2019, 2020). In addition to the formation of the S-type anatectic granite from melting of the upper crust in the amphibolite facies above the hot lines, this anatectic melting also gave rise to interconnected andesite-rhyolite volcanism on the surface. The andesite-rhyolite volcanism has the island-arc geochemical characteristics and occurs in a belt arrangement in the northern part of Gemeric unit. Andesite has the characteristics of upper crust and rhyolite characteristics of the mantle (Radvanec & Gonda, 2019). Basalts form separate outflows and occur outside the Gemeric unit (Vozárová & Vozár, 1988). The formation of S-type granitic melt together with the formation of magmatic chambers of Permian calc-alkaline / K-calc-alkaline volcanism (andesite, rhyolite,

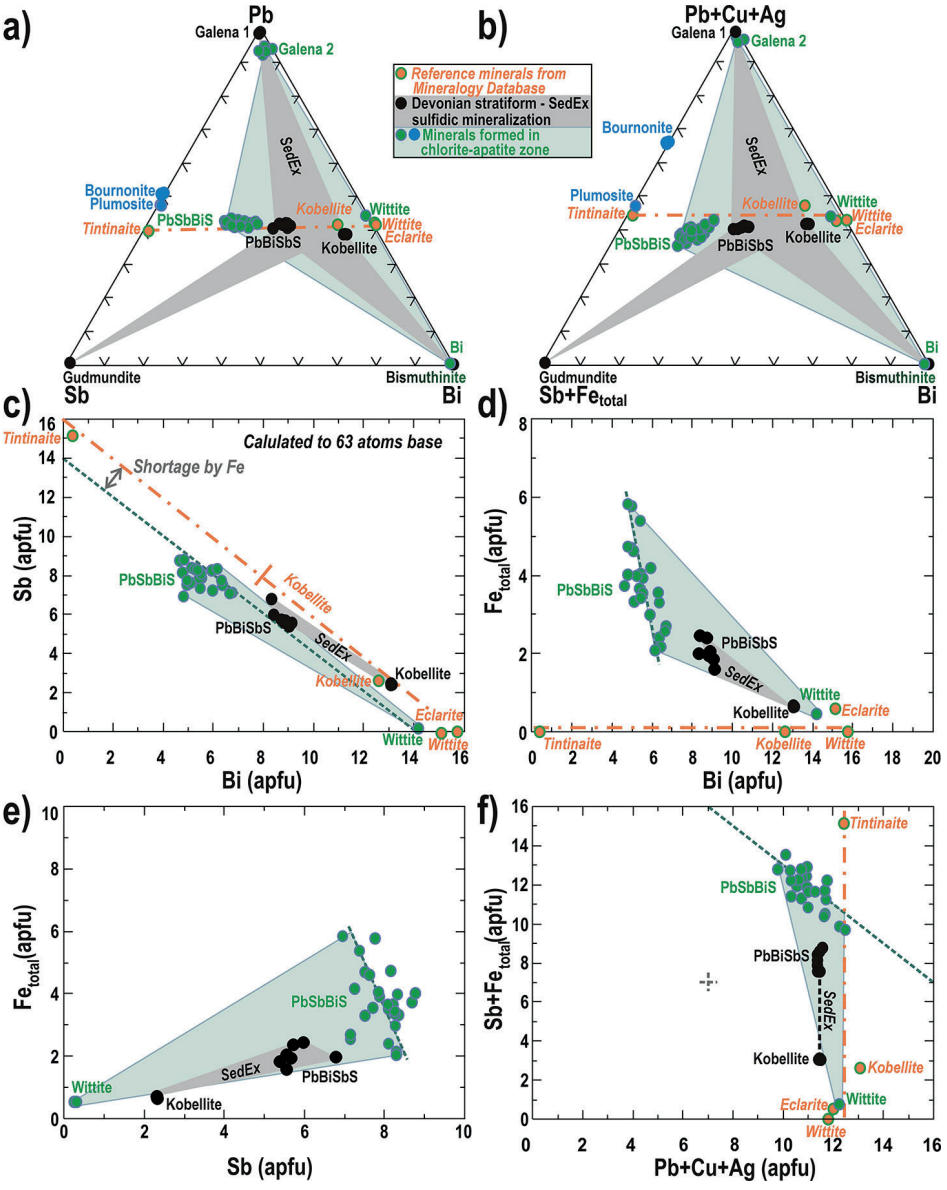

Fig. 20. Chemical classification of stratiform PbBiSb-rich sulfides formed by the SedEx process in the Late Silurian–Early Devonian and their comparison with the new PbSbBi-rich sulfides formed by the chlorite-apatite zone in the diagrams. ***a*** – Composition of sulfides formed by SedEx in the Sb-Bi-Pb system and their comparison to the new sulfides generation show a rough approximation of Pb-Bi-Sb and Pb-Sb-Bi-rich sulfides from the wittite/eclarite end member to tintinaite in the triangle diagram. ***b*** – The triangle diagram Sb + Fe_{total} – Bi – Pb + Cu + Ag shows a more accurate sulfides classification of both generations and shows the effect of FeSbS molecule in PbSbBi-rich sulfides being formed in the chlorite-apatite zone. ***c*** – Substitution of Bi versus Sb, with the exception of kobellite, shows a shortage in the new sulfides of chlorite-apatite zone studied when compared them with ideal Bi and Sb contents of the end-members betwen the wittite/eclarite to tintinaite. ***d*** – Bi versus Fe_{total} shows trends in the correlation beyond the wittite/eclarite – tintinaite end-members and demonstrates the relationship between sulfides formed by the SedEx process and new sulfides formed in the chlorite-apatite zone. ***e*** – Relationship of the two sulfide generations in the Fe_{total} versus Sb diagram with their correlation trends. ***f*** – The sum of Pb + Cu + Ag contents versus Sb + Fe_{total} shows the constant distribution of Pb + Cu + Ag contents in sulfides formed by the SedEx process in contrast to PbSbBi-rich sulfides where the sum of Pb + Cu + Ag substituted the sum of Sb + Fe_{Total}.

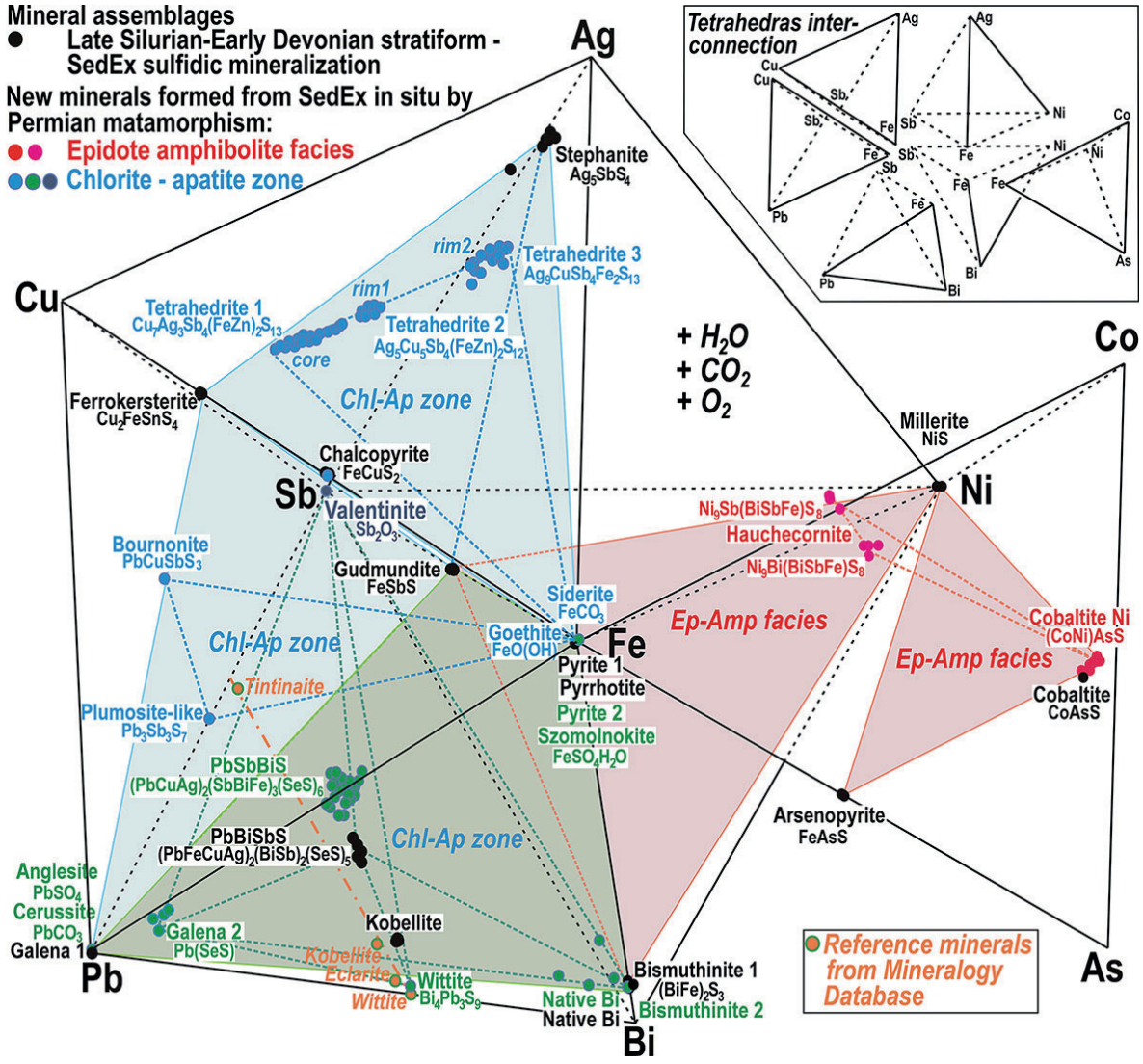

Fig. 21. Projections of mineral chemical formulas in the individual tetrahedral phase diagrams linked in the CuAgSbFePbBiAsCoNi system show a relationship between the source Late Silurian-Early Devonian stratiform SedEx sulfidic mineralization and new mineral assemblages formed in Permian epidote-amphibolite facies and related Permian chlorite-apatite zone including the reaction planes.

dacite) in the island arc magmatism caused the bulging of the upper crust above the hot line, which is considered by some authors to be a manifestation of extension related to the Permian rift (Vozárová et al., 2009, 2009a, 2012, 2013, 2015).

Acknowledgements

Authors express their thanks to Ministry of Environment of Slovak Republic for funding several long lasting regional metallogenetic projects in the Western Carpathians. The remarks and suggestions of two anonymous reviewers and Zoltán Németh (SGUDS) are greatly appreciated. This study is also a contribution to EuroGeoSurveys HORIZON-CSA project Geological Service for Europe WP2 Critical Raw Materials and WP6 Geological framework for the European geological data & information systems.

References

Bartalský, J., Ilavský, J., Bartalský, B., Čiško, V., Grecula, P., Hock, M., Kellner, M., Kladivík, E., Magula, R., Návesňák, D., Popreňák, J., Radvanec, M., Szabó, R. & Žifčák, F., 1993: Smolník – mesto medenorudných baní. Geológia ložiska polymetalických rúd, ich využitie a vplyv na mesto a okolie. *Bratislava, Miner. Slov., ISBN 80-967010-0-0.*

Biagioni, C., George L. L., Cook, N. J., Makovicky, E., Moëlo, Y., Pasero, M., Sejkora, J., Stanley, C. J., Mark, D., Welch, M. D. & Bosi, F., 2020: The tetrahedrite group: Nomenclature and classification. *Amer. Mineralogist, 105, 109–122.*

Buerger, M. J., 1939: The crystal structure of gudmundite (FeSbS) and its bearing on the existence field of the arsenopyrite structural type. *Z. Kristallogr. Crystall. Mater., 101, 1–6, 290–316.*

Faryad, S. W. & Peterec, D., 1987: Manifestations of skarn mineralization in the eastern part of the Spišsko-gemerské rudohorie Mts. *Geol. Carpath., 38, 111–128.*

Fleet, M. E., 2003: Sheet silicates: Micas, Rock forming minerals. *Volume 3A Sec. ed.*

Grecula, P., 1982: Gemericum – segment of the Paleotethyan riftogenous basin. *Bratislava, Miner. Slov – Monogr., Alfa, 1–263.*

Grecula, P., Abonyi, A., Abonyiová, M., Antaš, J., Bartalský, B., Bartalský, J., Dianiška, I., Drnzík, E., Ďuďa, R., Gargulák, M., Gazdačko, Ľ., Hudáček, J., Kobulský, J., Lörincz, L., Macko, J., Návesňák, D., Németh, Z., Novotný, L., Radvanec, M., Rojkovič, L., Rozložník, O., Varček, C. & Zlocha, J., 1995: Mineral deposit of the Slovak Ore Mountains. Vol. 1. *Bratislava, Miner. Slov. – Monogr., 1–834.*

Grecula, P. (ed.), Kobulský, J., Gazdačko, Ľ., Németh, Z., Hraško, Ľ., Novotný, L. & Maglay, J., 2009: Geologická mapa Spišsko-gemerského rudohoria 1 : 50 000. *Bratislava, Ministerstvo* život. *prostr. Slovenskej republiky – Št. Geol. Úst. D. Štúra.*

Grecula, P., Kobulský, J., Gazdačko, Ľ., Németh, Z., Hraško, Ľ., Novotný, L., Maglay, J., Pramuka, S., Radvanec, M., Kucharič, Ľ., Bajtoš, P. & Záhorová, Ľ., 2011: Vysvetlivky ku geologickej mape Spišsko-gemerského rudohoria 1 : 50 000. *Bratislava, Št. Geol. Úst. D. Štúra (in Slovak).*

Ilavský, J., 1961: Výhľadová štúdia o Cu rudách do roku 1980. Centrálna časť gemeríd. Kýzové a impregnačné polymetalické typy zrudnení. *Manuscript. Bratislava, archive St. Geol. Inst. D. Štúr.*

Kantor, J. & Fusán, O., 1952: Pyritové ložisko v Bystrom potoku. *Manuscript. Bratislava, archive St. Geol. Inst. D. Štúr* (3495).

Kissin, S. A. & Ovens, D. R., 1986: The crystallography of sakuraiite. *Canad. Mineralogist, 24, 679–683.*

Kohút, M. & Stein, H., 2005: Re-Os molybdenite dating of granite-related Sn-W-Mo mineralization at Hnilec, Gemeric Superunit, Slovakia. *Mineral. Petrol., 85, 117–129.*

Morad, V. J., 1990: High chromium and vanadium in andalusite, phengite and retrogressive margarite in contact metamorphosed Ba-rich slate from the Abercrombie Beds, New South Wales, Austria. *Min. Mag., 54, 381–391.*

Navesňák, D., 1994: Izotopické zloženie olova galenitov Spišsko-gemerského rudohoria a interpretácia. *Manuscript. Bratislava, archive St. Geol. Inst. D. Štúr.*

Nakamura, Y. & Shima, H., 1982: Fe and Zn partitioning between sphalerite and stannite. In: Proceedings of the Joint Meeting of Society of Mining Geologists of Japan; The Japanese Association of Mineralogists, Petrologists and Economic Geologists and the Mineralogical Society of Japan, *Sendai, Japan* (in Japanese).

Németh, Z., 2021: Lithotectonic units of the Western Carpathians: Suggestion of simple methodology for lithotectonic units defining, applicable for orogenic belts world-wide. *Miner. Slov., 53, 2, 81–91*.

Radvanec, M., Piovarcsy, K. & Böhmová, I., 1988: Vzťah slovinskej Hrubej, Gelnickej a Krížovej žily v slovinsko--gelnickom rudnom poli. *Miner. Slov.,20, 239–248.*

Radvanec, M., Žák, K. & Grecula, P., 1990: Izotopický pomer $^{87}Sr/^{86}Sr$ v baryte gemerika. *Miner. Slov.,22, 219–224.*

Radvanec, M., Grecula, P., Návesňák, D. & Kobulský, J., 1993: Zonálnosť submarinno-exhalačnej mineralizácie v oblasti Mníška nad Hnilcom a Prakoviec, staršie paleozoikum gemerika. *Miner. Slov., 25, 249–262*.

Radvanec, M., Grecula, P. & Žák, K., 2004: Siderite mineralization of the Gemericum superunit (Western Carpathians, Slovakia): review and revised genetic model. *Ore. Geol. Rev., 24, 3–4, 267–298.*

Radvanec, M., Konečný, P., Németh, Z. & Grecula, P., 2007: P-T-t path and local anatectic melting of the Lower Paleozoic metapelite with the admixture of psammitic quartz in Variscan metamorphism in Gemericum. *Miner. Slov. 39, 1–44* (in Slovak with English resume).

Radvanec, M., Konečný, P., Ondrejka, M., Putiš, M., Uher, P. & Németh, Z., 2009: Granity gemerika ako indikátor extenzie kôry nad neskorovariskou subdukčnou zónou a pri ranoalpínskej riftogenéze (Západné Karpaty): interpretácia podľa veku monazitu a zirkónu datovaného metódou CHIME a SHRIMP. *Miner. Slov., 41, 381–394*.

Radvanec, M., Németh, Z. & Bajtoš, P. (eds.), Koděra, P., Prochaska, W., Roda, Š., Tréger, M., Baláž, P., Grecula, P., Cicmanová, S., Kráľ, J. & Žák, K., 2010: Magnesite and Talc in Slovakia – Genetic and Geoenvironmental Models. *Bratislava, Št. Geol. Úst. D. Štúra, 189 p. ISBN 978-80--89343-31-7.*

Radvanec, M. & Grecula, P., 2016: Geotectonic and metallogenetic evolution of Gemericum (Inner Western Carpathians) from Ordovician to Jurassic. *Miner. Slov., 48, 104–118.*

Radvanec, M., Németh. Z., Kráľ, J. & Pramuka, S., 2017: Variscan dismembered metaophiolite suite fragments of Paleo-Thetys in Gemeric unit, Western Carpathians. *Miner. Slov., 49, 1–48.*

Radvanec, M. & Gonda, S., 2019: Genetic model of Permian hydrothermal mineralization in Gemeric unit (Western Carpathians) from the deep-seated zone of anatectic melting to volcanic-exhalative SedEx mineralization on the surface. *Miner. Slov., 52, 109–156.*

Radvanec, M. & Gonda, S., 2020: Successive formation of Fe and Mn skarns in the Čučma locality (Gemeric unit, W. Carpathians): from metasomatic stage through the amphibolite facies overprint with Ti-rich tephroite to retrograde stilpnomelane-chlorite zone. *Miner. Slov., 52, 2, 103–132.*

Ravna, K., 2000: The garnet-clinopyroxene Fe^{2+}-Mg geothermometer: an updated calibration. *J. Metamorp. Geol., 18, 2, 211–219,* doi:10.1046/j.1525-1314.2000.00247.x.

Spear, F. S., 1995: Metamorphic Phase Equilibria and Pressure-Temperature-Time Paths. Monogr. *Mineral. Soc. Amer.*

Smolárik, M. & Németh, Z., 2015: Talc genesis related on tectonometamorphic evolution: Preliminary results from the Gemerská Poloma deposit (Gemericum, Western Carpathians). Mineralogicko-petrologická konferencia Petros 20105. Zborník recenzovaných abstratkov a príspevkov. *Bratislava, Univ. Komenského, Prírodoved. fakulta, 54–57.*

Števko, M. & Sejkora, J., 2021: Bismuth, lead-bismuth and lead-antimony sulfosalts from the granite-hosted hydrothermal quartz veins at the Elisabeth mine, Gemerská Poloma, Spišsko-gemerské rudohorie Mts., Slovakia. *J. Geosci., 66, 157–173.*

Vozárová, A. & Vozár, J., 1988: Late Paleozoic in West Carpathians. *Bratislava, Geol. Úst. D. Štúra, 1–314.*

Vozárová, A., Šmelko, M. & Paderin, I., 2009: Permian single crystal U-Pb zircon ages of the Rožňava Formation volcanites (Southern Gemeric Unit, Western Carpathians, Slovakia). *Geol. Carpath., 60, 6, 439–448.*

Vozárová, A., Ebner, F., Kovács, S., Kräutner, H.-G., Szederkenyi, T., Krstić, B., Sremac, J., Aljinović, D., Novak, M. & Skaberne, D., 2009a: Late Variscan (Carboniferous to Permian) environments in the Circum Pannonian Region. *Geol. Carpath., 60, 71–104.*

Vozárová, A., Šmelko, M., Paderin, I. & Larionov, A., 2012: Permian volcanics in Northern Gemericum and Bôrka Nappe system: U-Pb zircon dating and implication to geodynamic evolution (Western Carpathians, Slovakia). *Geol. Carpath., 63, 191–200.*

Vozárová, A., Laurinc, D., Šarinová, K., Larionov, A., Presnyakov, S., Rodionov, N. & Paderin, I., 2013: Pb ages of detrital zircons in relation to geodynamic evolution: Paleozoic of the Northern Gemericum (Western Carpathians, Slovakia). *J. Sed. Res., 83, 915–927.*

Vozárová, A., Presnyakov, S., Šarinová, K. & Šmelko, M., 2015: First evidence for Permian-Triassic boundary volcanism in the Northern Gemericum: geochemistry and U-Pb zircon geochronology. *Geol. Carpath., 66, 5, 375–391.*

Žák, K., Radvanec, M. & Grecula, P., 2005: Siderite mineralization of the Gemericum Superunit (Western Carpathians, Slovakia): review and a revised genetic model [Ore Geology Reviews, 24, 267–298] – a reply. *Ore Geol. Rev., 26, 173–180.*

Tab. 1
Representative analyses of millerite, cobaltite and hauchecornite.

Mineral	Millerite	Cobaltite 1	Cobaltite 2	Cobaltite 2	Cobaltite 2	Hauchecornite	Hauchecornite-(Sb)	Hauchecornite-(Sb)
Enriched			**Ni**	**Ni**	**Ni**	**Bi**	**Bi. Sb**	**Sb**
Process	**SedEx**	**SedEx**	**Ep-Amp**	**Ep-Amp**	**Ep-Amp**	**Ep-Amp**	**Ep-Amp**	**Ep-Amp**
S	35.65	20.26	19.87	20.42	20.24	22.62	24.35	25.60
Fe	0.67	1.67	1.50	2.64	1.51	1.42	1.13	2.12
Co	0.29	32.73	25.78	27.49	32.49	1.97	2.96	2.89
Ni	64.18	0.98	7.81	4.94	3.09	44.62	46.92	47.65
Cu	0.09	0.00	0.01	0.02	0.00	0.03	0.08	0.06
Sb	0.00	0.36	0.25	0.74	0.53	5.06	16.72	20.41
As	0.02	42.87	43.85	42.07	42.79	0.00	0.00	0.05
Pb	0.10	0.06	0.01	1.48	0.00	0.22	0.34	0.34
Se	0.00	0.00	0.00	0.00	0.00	0.07	0.00	0.01
Bi	0.00	0.03	0.01	0.02	0.04	24.94	8.27	1.55
Total (wt %)	101.00	98.96	99.09	99.82	100.69	100.95	100.77	100.68
S	1.000	1.047	1.030	1.055	1.030	7.940	7.975	8.086
Se	0.000	0.000	0.000	0.000	0.000	0.010	0.000	0.001
X group	***1.000***	***1.047***	***1.030***	***1.055***	***1.030***	***7.950***	***7.975***	***8.087***
Cu	0.001	0.000	0.000	0.001	0.000	0.005	0.013	0.010
Co	0.004	0.921	0.727	0.773	0.900	0.376	0.528	0.497
Ni	0.983	0.028	0.221	0.140	0.086	8.559	8.397	8.225
Pb	0.000	0.000	0.000	0.012	0.000	0.012	0.017	0.017
Fe^{2+}	0.011	0.050	0.045	0.078	0.044	0.048	0.045	0.251
A group	***0.999***	***0.999***	***0.993***	***1.004***	***1.030***	***9.000***	***9.000***	***9.000***
Sb	0.000	0.005	0.003	0.010	0.007	0.468	1.442	1.698
As	0.000	0.949	0.973	0.931	0.932	0.000	0.000	0.007
Bi	0.000	0.000	0.000	0.000	0.000	1.343	0.416	0.075
Fe^{3+}	0.000	0.000	0.000	0.000	0.000	0.238	0.168	0.134
B group	***0.000***	***0.954***	***0.976***	***0.941***	***0.939***	***2.049***	***2.026***	***1.914***
Sum (atom.)	1.999	3.000	2.999	3.000	2.999	18.999	19.001	19.001
Fe (Sum)	0.011	0.05	0.045	0.078	0.044	0.286	0.213	0.385

Tab. 2
Representative analyses of garnet pyroxene (hedenbergite), epidote, actinolite, chlorite, titanite and apatite in the skarn.

Mineral	Garnet	Pyroxene	Pyroxene	Epidote	Actinolite	Chlorite	Titanite-F	Apatite-F
Rock	Skarn	Skarn	Skarn	Skarn	Skarn	Skarn	Skarn	Skarn
Process	Ep-Amp.f.	Ep-Amp.f.	Ep-Amp.f.	Ep-Amp.f.	Ep-Amp.f.	Ep-Amp.f.	Chl-Ap	Chl-Ap
SiO_2	37.85	50.77	49.21	38.02	52.35	31.96	31.32	0.00
TiO_2	0.33	0.07	0.04	0.04	0.02	0.00	33.44	0.00
Al_2O_3	20.71	0.29	0.53	24.92	1.28	9.31	4.46	0.00
Cr_2O_3	0.01	0.00	0.00	0.01	0.00	0.00	0.00	0.00
Fe_2O_3	0.00	0.00	0.00	11.58	0.00	0.00	0.00	0.00
FeO	8.85	18.22	16.42	0.00	21.84	31.83	1.36	0.01
MnO	13.02	3.55	6.02	0.34	1.51	0.74	0.03	0.04
MgO	0.03	4.95	4.32	0.00	8.99	12.98	0.03	0.01
CaO	19.28	22.40	22.52	23.06	12.12	0.56	29.43	56.22
SrO	0.00	0.00	0.00	0.00	0.00	0.00	0.00	0.21
Na_2O	0.00	0.26	0.11	0.00	0.22	0.03	0.04	0.00
K_2O	0.00	0.00	0.00	0.00	0.11	0.03	0.00	0.00
P_2O_5	0.00	0.00	0.00	0.00	0.00	0.00	0.00	41.37
F	0.24	0.00	0.00	0.00	0.00	0.03	1.31	4.47
Cl	0.01	0.00	0.00	0.00	0.01	0.00	0.02	0.01
Total	100.32	100.51	99.17	97.97	98.45	87.47	100.82	100.46
Si	2.980	2.004	1.979	3.003	7.834	7.012	1.019	0.000
Al^{IV}	0.020	0.000	0.021	0.000	0.166	0.988	0.000	0.000
Sum_T	3.000	2.004	2.000	3.003	8.000	8.000	1.019	0.000
Al^{VI}	1.899	0.013	0.004	2.318	0.060	1.417	0.171	0.000
Fe^{3+}	0.000	0.000	0.023	0.688	0.144	0.000	0.000	0.000
Ti	0.020	0.002	0.001	0.002	0.002	0.000	0.819	0.000
Cr	0.001	0.000	0.000	0.001	0.000	0.000	0.000	0.000
Fe^{2+}	0.583	0.601	0.529	0.000	2.590	5.840	0.037	0.001
Mg	0.004	0.291	0.259	0.000	2.006	4.245	0.002	0.001
Mn	0.868	0.119	0.205	0.023	0.191	0.138	0.001	0.003
Ca	1.626	0.947	0.970	1.952	1.943	0.132	1.026	5.088
Sr	0.000	0.000	0.000	0.000	0.000	0.000	0.000	0.01
Na	0.000	0.020	0.009	0.000	0.064	0.013	0.003	0.000
K	0.000	0.000	0.000	0.000	0.021	0.008	0.000	0.000
P	0.000	0.000	0.000	0.000	0.000	0.000	0.000	2.959
Sum	8.000	4.000	4.000	7.987	15.021	19.793	3.078	8.062
O	12	6	6	13	23	36	5	13
O-F-Cl	0.00	0.00	0.00	0.00	0.00	0.00	0.56	1.88

Tab. 3

Representative analyses of pyrite generations, chalcopyrite, arsenopyrite, galena, stephanite and gudmundite.

Mineral	Pyrite 1	Pyrite 1	Pyrrhotite	Chalcopyrite	Arsenopyrite	Gudmundite	Galena 1	Stephanite	Pyrite 2
Process	**SedEx**	**SedEx**	**SedEx**	**SedEx**	**SedEx**	**Sedex**	**SedEx**	**SedEx**	**Chl-Ap**
S	52.88	52.77	38.83	34.81	19.98	15.65	13.63	15.93	53.82
Cd	0.00	0.00	0.00	0.00	0.00	0.01	0.00	0.00	0.00
Ag	0.02	0.07	0.04	0.05	0.00	0.03	0.05	66.72	0.00
Zn	0.00	0.00	0.00	0.05	0.18	0.04	0.44	0.02	0.00
Fe	47.14	46.80	60.07	30.65	34.50	26.68	0.00	0.08	45.58
Co	0.00	0.13	0.00	0.00	0.00	0.00	0.00	0.00	0.00
Au	0.00	0.12	0.13	0.00	0.00	0.00	0.00	0.00	0.00
Cu	0.04	0.00	0.00	33.84	0.00	0.10	0.00	0.16	0.00
In	0.00	0.00	0.00	0.16	0.00	0.00	0.00	0.12	0.00
Sn	0.00	0.00	0.00	0.06	0.00	0.00	0.00	0.00	0.00
Sb	0.07	0.05	0.00	0.00	0.00	57.83	0.17	15.47	0.00
As	0.05	0.08	0.09	0.04	44.43	0.00	0.00	0.00	0.00
Pb	0.00	0.00	0.00	0.00	0.00	0.09	85.22	0.67	0.00
Bi	0.05	0.00	0.14	0.00	0.00	0.08	0.25	0.04	0.00
Total (wt %)	100.25	100.02	99.30	99.66	99.09	100.51	99.76	99.21	99.4
S	1.982	1.984	1.058	2.000	1.018	1.014	1.005	3.970	2.018
Cd	0.000	0.000	0.000	0.000	0.000	0.000	0.000	0.000	0.00
Ag	0.000	0.001	0.000	0.001	0.000	0.001	0.001	4.944	0.00
Sn	0.000	0.000	0.000	0.001	0.000	0.000	0.000	0.000	0.00
Cu	0.001	0.000	0.000	0.981	0.000	0.003	0.000	0.020	0.00
Zn	0.000	0.000	0.000	0.001	0.004	0.001	0.016	0.002	0.00
Fe	1.015	1.010	0.940	1.011	*1.009	*0.992	0.000	0.011	0.982
In	0.000	0.000	0.000	0.003	0.000	0.000	0.000	0.008	0.00
Sb	0.001	0.000	0.000	0.000	0.000	0.987	0.003	1.016	0.00
As	0.001	0.001	0.001	0.001	0.969	0.000	0.000	0.000	0.00
Pb	0.000	0.000	0.000	0.000	0.000	0.001	0.972	0.026	0.00
Bi	0.000	0.000	0.001	0.000	0.000	0.001	0.003	0.002	0.00
Co	0.000	0.003	0.000	0.000	0.000	0.000	0.000	0.000	0.00
Au	0.000	0.001	0.001	0.000	0.000	0.000	0.000	0.000	0.00
Sum (atom.)	3	3	2	4	3	3	2	10	3
Fe/S	0.51	0.51							0.49

(*) – Fe^{3+}

Tab. 4
Representative analyses of kobellite, PbBiSb-sulfide, bismuthinite, native Bi, wittite, PbSbBi-sulfide and Se-rich galena.

Mineral	Kobellite	Kobellite	PbBiSbS	PbBiSbS	PbBiSbS	Bismuthinite 1	Bismuthinite 2	native Bi 1	Wittite	PbSbBiS	PbSbBiS	PbSbBiS	PbSbBiS	PbSbBiS	native Bi 2	Galena 2	Galena 2
Enriched			Se	Se	Se				Se	Fe. Se	Fe. Se	Fe. Se	Fe. Se	Fe. Se		Se	Se
Process	SedEx	SedEx	SedEx	SedEx	SedEx	SedEx	Chl-Ap	Chl-Ap	Chl-Ap	Chl-Ap	Chl-Ap	Chl-Ap	Chl-Ap	Chl-Ap	Chl-Ap	Chl-Ap	Chl-Ap
S	17.49	17.56	18.38	18.47	18.58	19.39	19.59	0.62	16.24	18.41	19.13	19.78	19.85	20.31	3.86	13.88	12.63
Se	0.13	0.15	0.68	0.72	0.58	0.18	0.00	0.00	1.87	0.73	1.00	0.94	0.77	0.73	0.04	1.13	3.41
Te	0.00	0	0.00	0.08	0.00	0.00	0.00	0.00	0.00	0.00	0.02	0.03	0.00	0.00	0.00	0.00	0.09
Cd	0.06	0.04	0.07	0.00	0.02	0.02	0.04	0.08	0.02	0.10	0.08	0.06	0.07	0.08	0.10	0.01	0.00
Ag	0.52	0.52	0.45	0.36	0.35	0.02	0.00	0.07	0.24	0.33	0.36	0.30	0.31	0.25	0.03	0.37	0.12
Zn	0.02	0.02	0.00	0.02	0.03	0.00	0.00	0.00	0.00	0.00	0.00	0.00	0.04	0.00	0.00	0.00	0.00
Fe	0.59	0.54	2.21	1.90	2.28	2.57	1.76	1.32	0.47	2.03	3.50	4.06	5.48	6.02	2.56	2.37	2.06
Mn	0.00	0	0.00	0.00	0.00	0.01	0.00	0.00	0.00	0.00	0.00	0.00	0.00	0.00	0.00	0.00	0.00
Cu	1.03	1.11	0.84	0.82	0.82	0.14	0.18	0.19	0.22	0.95	0.95	1.00	0.86	1.21	0.49	0.15	0.34
In	0.00	0	0.00	0.00	0.00	0.02	0.02	0.00	0.00	0.00	0.03	0.00	0.03	0.04	0.00	0.00	0.00
Sn	0.00	0	0.00	0.00	0.00	0.05	0.10	0.04	0.04	0.00	0.08	0.00	0.00	0.00	0.00	0.00	0.00
Sb	4.54	4.57	11.64	11.28	12.25	0.13	0.63	3.05	0.52	17.17	16.55	19.39	16.37	17.67	7.10	1.28	0.08
Pb	32.79	32.93	35.54	35.75	35.78	0.75	0.90	1.78	36.51	37.37	35.27	36.57	35.55	34.65	10.87	76.36	76.71
Bi	42.83	43.01	30.29	30.98	29.42	76.55	76.53	92.97	44.13	23.07	23.24	18.29	20.72	19.38	75.94	3.67	4.51
Total (wt. %)	100.00	100.45	100.10	100.37	100.11	99.84	99.79	100.14	100.27	100.16	100.22	100.41	100.05	100.33	101.00	99.22	99.95
S	69.567	69.533	4.906	4.939	4.927	2.943	2.986	0.037	8.652	5.900	5.915	5.931	5.921	5.915	0.185	0.970	0.902
Se	0.210	0.241	0.073	0.079	0.062	0.011	0.000	0.000	0.405	0.095	0.125	0.114	0.094	0.086	0.001	0.032	0.099
Te	0.000	0.000	0.000	0.005	0.000	0.000	0.000	0.000	0.000	0.000	0.002	0.002	0.000	0.000	0.000	0.000	0.002
group X	69.777	69.774	4.979	5.023	4.989	2.954	2.986	–	9.057	5.995	6.042	6.047	6.015	6.001	–	1.002	1.003
Cd	0.068	0.045	0.005	0.000	0.002	0.001	0.002	0.001	0.003	0.009	0.007	0.005	0.006	0.007	0.001	0.000	0.000
Ag	0.615	0.612	0.036	0.028	0.027	0.001	0.000	0.001	0.038	0.031	0.033	0.027	0.027	0.022	0.000	0.008	0.003
Cu	2.068	2.218	0.113	0.110	0.110	0.011	0.014	0.006	0.058	0.154	0.149	0.151	0.129	0.177	0.012	0.005	0.012
Zn	0.039	0.039	0.000	0.003	0.004	0.000	0.003	0.000	0.005	0.000	0.000	0.000	0.006	0.000	0.000	0.000	0.000
Mn	0.000	0	0.000	0.000	0.000	0.001	0.000	0.000	0.000	0.000	0.000	0.000	0.000	0.000	0.000	0.000	0.000
In	0.000	0	0.000	0.000	0.000	0.001	0.001	0.000	0.000	0.000	0.003	0.000	0.003	0.003	0.000	0.000	0.000
Pb	20.187	20.182	1.468	1.479	1.468	0.018	0.021	0.016	3.010	1.854	1.688	1.698	1.641	1.562	0.081	0.826	0.848
Fe^{2+}	1.348	1.228	0.339	0.291	0.347	0.000	0.000	0.045	0.142	0.000	0.075	0.075	0.173	0.228	0.071	0.095	0.084
grupe A	–	–	1.961	1.911	1.958	0.033	0.041	–	–	2.048	1.955	1.956	1.985	1.999	–	–	–
Fe^{3+}	–	–	–	–	–	0.224	0.154	–	–	0.374	0.547	0.624	0.766	0.778	–	–	–
Sb	4.757	4.767	0.819	0.794	0.855	0.005	0.025	0.048	0.073	1.449	1.348	1.532	1.286	1.356	0.090	0.024	0.002
Sn	0.000	0	0.000	0.000	0.000	0.002	0.004	0.001	0.006	0.000	0.007	0.000	0.000	0.000	0.000	0.000	0.000
Bi	26.143	26.135	1.241	1.271	1.197	1.782	1.790	0.845	3.607	1.135	1.103	0.842	0.948	0.866	0.559	0.039	0.049
grupe B	–	–	2.060	2.065	2.052	2.013	1.973	–	–	2.958	3.005	2.998	3.000	3.000	–	–	–
Sum (atom.)	125	125	9	9	9	5	5	1	16	11	11	11	11	11	1	2	2
Fe sum-at.	1.348	1.228	0.339	0.291	0.347	0.224	0.154	0.045	0.142	0.374	0.622	0.699	0.939	1.006			
The balance of Fe^{2+} and Fe^{3+} calculated according to element substitutions (Fig. 20) and according to chemical formulae divided into groups A. B. X																	

Tab. 5

Representative analyses of In-rich sphalerite 1, ferrokesterite and Sn-rich sakuraiite.

Mineral	Sphalerite 1	Sphalerite 1	Sphalerite 1	Sphalerite 1	Fe-kesterite	Fe-kesterite	Fe-kesterite	Fe-kesterite	Fe-kesterite	Fe-kesterite	Sn sakuraiite	Sn sakuraiite	Sn sakuraiite	Sn sakuraiite	Sn sakuraiite	Sn sakuraiite	Sn sakuraiite	Sn sakuraiite
Enriched					Zn	Zn	In	In	In	In	In	In	Sn	Sn	In	In	In	In
Process	SedEx	SedEx	SedEx	SedEx	SedEx	SedEx	SedEx	SedEx	SedEx	SedEx	SedEx	SedEx	SedEx	SedEx	SedEx	SedEx	SedEx	SedEx
S	34.01	32.74	32.78	31.84	30.01	29.45	30.03	29.41	29.99	29.96	29.36	30.19	30.12	32.30	29.82	30.46	30.11	31.41
Cd	0.26	0.39	0.49	0.00	0.03	0.00	0.03	0.00	0.00	0.00	0.00	0.03	0.00	0.13	0.03	0.04	0.00	0.00
Ag	0.04	0.01	0.01	0.04	0.02	0.03	0.05	0.00	0.00	0.12	0.09	0.12	0.05	0.05	0.04	0.06	0.07	0.08
Zn	57.64	55.12	49.87	46.21	3.86	7.26	4.03	2.05	6.66	3.61	3.46	9.28	9.17	40.62	11.61	14.53	15.63	30.17
Fe	6.67	7.19	7.85	6.94	12.11	11.90	12.11	12.71	13.35	13.05	13.56	12.08	11.55	8.21	12.01	11.55	11.76	10.04
Mn	0.01	0.00	0.02	0.00	0.04	0.00	0.00	0.00	0.00	0.00	0.00	0.00	0.00	0.01	0.00	0.01	0.00	0.00
Cu	0.33	1.46	2.95	4.98	28.59	26.18	27.53	27.60	25.85	26.61	26.10	24.23	24.98	9.51	23.25	21.54	20.33	12.78
In	0.63	2.82	5.63	8.78	0.00	0.00	0.54	2.34	3.36	4.06	4.31	3.07	0.00	0.00	1.95	1.87	5.03	5.91
Sn	0.00	0.00	0.00	0.00	25.23	24.91	26.12	25.09	21.12	22.51	23.00	20.87	23.86	8.81	21.49	19.90	16.91	9.44
Pb	0.00	0.00	0.61	0.21	0.00	0.00	0.00	0.00	0.00	0.00	0.00	0.06	0.04	0.00	0.41	0.38	0.00	0.00
Se	0.00	0.00	0.00	0.00	0.00	0.00	0.00	0.00	0.00	0.00	0.00	0.11	0.00	0.00	0.00	0.00	0.00	0.00
Bi	0.03	0.00	0.03	0.00	0.03	0.04	0.00	0.00	0.00	0.00	0.00	0.00	0.00	0.05	0.00	0.00	0.00	0.00
Total (wt %)	99.68	99.73	100.24	99.00	99.92	99.77	100.44	99.20	100.33	99.92	99.89	100.08	99.77	99.69	100.61	100.34	99.84	99.83
S	1.022	0.999	1.008	1.003	0.998	0.985	0.999	0.996	0.990	1.000	0.987	0.998	0.999	1.006	0.984	0.997	0.991	1.003
Cd	0.002	0.003	0.004	0.000	0.000	0.000	0.000	0.000	0.000	0.000	0.000	0.000	0.000	0.001	0.000	0.000	0.000	0.000
Ag	0.000	0.000	0.000	0.000	0.000	0.000	0.000	0.000	0.000	0.001	0.001	0.001	0.000	0.000	0.000	0.001	0.001	0.001
Sn	0.000	0.000	0.000	0.000	0.227	0.225	0.235	0.229	0.188	0.203	0.209	0.186	0.214	0.074	0.192	0.176	0.150	0.081
Cu	0.005	0.022	0.046	0.079	0.480	0.442	0.462	0.472	0.430	0.448	0.443	0.404	0.418	0.150	0.387	0.356	0.338	0.206
Zn	0.849	0.825	0.752	0.714	0.063	0.119	0.066	0.034	0.108	0.059	0.057	0.150	0.149	0.621	0.188	0.233	0.252	0.472
Mn	0.000	0.000	0.000	0.000	0.001	0.000	0.000	0.000	0.000	0.000	0.000	0.000	0.000	0.000	0.000	0.000	0.000	0.000
Fe	0.115	0.126	0.139	0.126	0.231	0.229	0.231	0.247	0.253	0.250	0.262	0.229	0.220	0.147	0.228	0.217	0.222	0.184
In	0.005	0.024	0.048	0.077	0.000	0.000	0.005	0.022	0.031	0.038	0.040	0.028	0.000	0.000	0.018	0.017	0.046	0.053
Pb	0.000	0.000	0.003	0.001	0.000	0.000	0.000	0.000	0.000	0.000	0.000	0.000	0.000	0.000	0.002	0.002	0.000	0.000
Se	0.000	0.000	0.000	0.000	0.000	0.000	0.000	0.000	0.000	0.000	0.000	0.001	0.000	0.000	0.000	0.000	0.000	0.000
Bi	0.000	0.000	0.000	0.000	0.000	0.000	0.000	0.000	0.000	0.000	0.000	0.000	0.000	0.000	0.000	0.000	0.000	0.000
Sum (atom.)	1.998	1.999	2.000	2.000	2.000	2.000	1.998	2.000	2.000	1.999	1.999	1.997	2.000	1.999	1.999	1.999	2.000	2.000
Sphalerite	84.9	82.5	75.2	71.4														
Pyrrhotite	11.5	12.6	13.9	12.6														
Roquesite	1	4.6	9.4	15.6														

Tab. 6
Representative analyses of Ag-rich tetrehedrite, bournonite, plumosite-like, valentinite and anglesite.

Mineral	Tetrahedrite 1	Tetrahedrite 1	Tetrahedrite 1	Tetrahedrite 2	Tetrahedrite 2	Tetrahedrite 3	Tetrahedrite 3	Tetrahedrite 3	Bournonite	Plumosite-like	Valentinite	Anglesite
	Tetrahedrite-*(Fe)*			Kenoargento--tetrahedrite-*(Fe)*		Rozhdestvenskayite-(*Fe*)						
Process	Chl-Ap	Chl-Ap	Chl-Ap	Chl-Ap	Chl-Ap	Chl-Ap	Chl-Ap	Chl-Ap	Chl-Ap	Chl-Ap	Chl-Ap	Chl-Ap
S	23.40	23.40	22.90	21.08	20.65	20.17	20.00	20.17	19.80	18.86	0.08	8.91
Cd	0.00	0.00	0.00	0.00	0.00	0.00	0.00	0.00	0.00	0.00	0.04	0.00
Ag	16.26	18.51	20.90	29.05	31.60	43.86	46.78	48.59	0.00	0.12	0.02	0.00
Zn	1.16	1.33	1.06	0.74	0.86	0.81	0.96	0.93	0.00	0.00	0.01	0.01
Fe	5.38	5.19	5.59	5.63	5.67	5.25	4.57	5.13	0.65	0.27	0.48	0.00
Mn	0.01	0.00	0.00	0.00	0.00	0.00	0.00	0.00	0.00	0.00	0.00	0.00
Cu	26.20	24.19	22.25	17.00	15.01	5.35	2.68	2.15	13.00	0.00	0.08	0.00
In	0.04	0.05	0.02	0.06	0.10	0.05	0.07	0.08	0.00	0.00	0.00	0.00
Sn	0.00	0.00	0.05	0.00	0.04	0.00	0.00	0.00	0.00	0.00	0.00	0.00
Sb	27.09	27.41	27.29	27.03	26.59	24.02	23.48	24.12	23.61	31.78	83.93	0.00
As	0.00	0.00	0.00	0.00	0.00	0.00	0.00	0.00	0.67	0.52	0.00	0.00
Pb	0.08	0.13	0.00	0.00	0.00	0.28	0.73	0.08	42.26	48.67	0.03	70.22
Bi	0.00	0.00	0.00	0.00	0.00	0.00	0.05	0.12	0.21	0.33	0.06	0.08
O	0.00	0.00	0.00	0.00	0.00	0.00	0.00	0.00	0.00	0.00	16.00	20.23
Total (wt %)	99.62	100.21	100.06	100.59	100.52	99.79	99.32	101.37	100.20	100.55	100.73	99.45
S	12.980	13.050	12.951	12.039	11.961	12.798	12.981	12.853	2.984	6.958	0.007	0.886
Cd	0.000	0.000	0.000	0.000	0.000	0.000	0.000	0.000	0.000	0.000	0.001	0.000
Ag	2.682	3.069	3.514	4.932	5.442	8.274	9.027	9.205	0.000	0.013	0.001	0.000
Sn	0.000	0.000	0.008	0.000	0.006	0.000	0.000	0.000	0.000	0.000	0.000	0.000
Cu	7.335	6.809	6.349	4.900	4.388	1.713	0.878	0.691	0.989	0.000	0.004	0.000
Zn	0.316	0.364	0.294	0.207	0.244	0.252	0.306	0.291	0.000	0.000	0.000	0.001
Mn	0.003	0.000	0.000	0.000	0.000	0.000	0.000	0.000	0.000	0.000	0.000	0.000
Fe	1.714	1.662	1.817	1.846	1.886	1.913	1.703	1.877	0.056	0.059	0.025	0.000
In	0.006	0.008	0.003	0.010	0.016	0.009	0.013	0.014	0.000	0.000	0.000	0.000
Sb	3.958	4.027	4.065	4.066	4.057	4.014	4.014	4.049	0.937	3.091	2.024	0.000
Te	0.000	0.000	0.000	0.000	0.000	0.000	0.000	0.000	0.000	0.000	0.000	0.000
As	0.000	0.000	0.000	0.000	0.000	0.000	0.000	0.000	0.043	0.081	0.000	0.000
Pb	0.007	0.011	0.000	0.000	0.000	0.027	0.073	0.008	0.986	2.779	0.000	1.080
Bi	0.000	0.000	0.000	0.000	0.000	0.000	0.005	0.012	0.005	0.020	0.001	0.075
O	–	–	–	–	–	–	–	–	–	–	3	4
Sum (atom.)	29	29	29	28	28	29	29	29	6	13	5	6
Other elements analysed: Se, Te												

Tab. 6 – Continuation.

Mineral	Tetrahedrite 1	Tetrahedrite 1	Tetrahedrite 1	Tetrahedrite 2	Tetrahedrite 2	Tetrahedrite 3	Tetrahedrite 3	Tetrahedrite 3
	Tetrahedrite-*(Fe)*			Kenoargento--tetrahedrite-*(Fe)*		Rozhdestvenskayite-(*Fe*)		
Process	**Chl-Ap**	**Chl-Ap**	**Chl-Ap**	**Chl-Ap**	**Chl-Ap**	**Chl-Ap**	**Chl-Ap**	**Chl-Ap**
Ag	0.000	0.000	0.000	4.932	5.442	6.000	6.000	6.000
Cu	6.000	6.000	6.000	1.068	0.558	0.000	0.000	0.000
A group	***6.000***	***6.000***	***6.000***	***6.000***	***6.000***	***6.000***	***6.000***	***6.000***
Cu (B group)	1.335	0.809	0.349	3.832	3.830	1.713	0.878	0.691
Ag (B group)	2.682	3.069	3.514	0.000	0.000	2.274	3.027	3.205
Pb	0.007	0.011	0.000	0.000	0.000	0.027	0.073	0.008
Sn	0.000	0.000	0.008	0.000	0.006	0.000	0.000	0.000
In	0.006	0.008	0.003	0.010	0.016	0.009	0.013	0.014
Mn^{2+} (C group)	0.003	0.000	0.000	0.000	0.000	0.000	0.000	0.000
Fe^{3+}(C group)	0.030	0.026	0.111	0.053	0.130	0.165	0.009	0.168
Fe^{2+} (C group)	1.684	1.636	1.706	1.793	1.756	1.748	1.694	1.709
Zn (C group)	0.316	0.364	0.294	0.207	0.244	0.252	0.306	0.291
B+C group	***6.063***	***5.923***	***5.985***	***5.934***	***5.982***	***6.188***	***6.000***	***6.086***
Zn+Fe^{2+}	***2.000***	***2.000***	***2.000***	***2.000***	***2.000***	***2.000***	***2.000***	***2.000***
Sb^{3+} (D group)	3.958	4.027	4.065	4.066	4.057	4.014	4.014	4.049
Bi^{3+}(D group)	0.000	0.000	0.000	0.000	0.000	0.000	0.005	0.012
D group	***3.958***	***4.027***	***4.065***	***4.066***	***4.057***	***4.014***	***4.019***	***4.061***
S (Y.Z group)	12.980	13.050	12.951	12.039	11.961	12.798	12.981	12.853
Sum (atom.)	29	29	29	28	28	29	29	29

Tab. 7
Representative analyses of dolomite, ankerite, siderite, cerussite and Mn-rich calcite.

Mineral	Dolomite	Dolomite	Ankerite	Ankerite	Siderite	Siderite	Siderite	Siderite	Cerussite	Calcite Mn	Calcite Mn
Process	Limestone	Limestone	Chl-Ap	Chl-Ap	Chl-Ap	Chl-Ap	Chl-Ap	Chl-Ap	Chl-Ap	Chl-Ap	Chl-Ap
FeO	5.24	4.97	9.01	17.62	61.16	58.57	59.77	52.37	2.58	2.06	0.81
MnO	3.28	2.46	3.71	1.34	0.29	2.23	0.44	2.35	0	8.2	6.71
MgO	16.82	17.72	13.66	9.5	0.29	0.1	0	1.19	0	0.44	0.07
CaO	28.48	28.9	28.32	27.75	0.25	0.77	1.79	5.09	0	45.81	49.08
SrO	0.09	0.07	0.08	0.14	0.01	0.02	0.02	0	0	0.09	0.04
PbO	0	0	0	0	0	0	0	0	79.65	0	0
CO_2	45.99	46.65	44.97	43.84	38.13	37.96	38.31	38.82	17.27	42.82	43.26
Total	99.9	100.77	99.75	100.2	100.12	99.65	100.34	99.82	99.5	99.42	99.97
Fe	0.070	0.065	0.123	0.246	0.982	0.945	0.956	0.826	0.092	0.029	0.011
Mn	0.044	0.033	0.051	0.019	0.005	0.036	0.007	0.038	0.000	0.119	0.096
Mg	0.399	0.415	0.332	0.237	0.008	0.003	0.000	0.033	0.000	0.011	0.002
Ca	0.486	0.486	0.494	0.497	0.005	0.016	0.037	0.103	0.000	0.840	0.890
Pb	0.000	0.000	0.000	0.000	0.000	0.000	0.000	0.000	0.979	0.000	0.000
Sr	0.001	0.001	0.001	0.001	0.000	0.000	0.000	0.000	0.000	0.001	0.000
Cations	1.000	1.000	1.001	1.000	1.000	1.000	1.000	1.000	1.071	1.000	0.999
CO_3	1.045	1.060	1.003	0.972	0.839	0.841	0.850	0.870	0.380	0.973	0.983
$CaCO_3$	48.6	48.6	49.4	49.7	0.5	1.6	3.7	10.3	0.0	84.0	89.1
$MgCO_3$	39.9	41.5	33.2	23.7	0.8	0.3	0.0	3.3	0.0	1.1	0.2
$FeCO_3$	7.0	6.5	12.3	24.6	98.2	94.5	95.6	82.6	8.6	2.9	1.1
$MnCO_3$	4.4	3.3	5.1	1.9	0.5	3.6	0.7	3.8	0.0	11.9	9.6
$PbCO_3$	0.0	0.0	0.0	0.0	0.0	0.0	0.0	0.0	91.4	0.0	0.0
$SrCO_3$	0.1	0.1	0.1	0.1	0.0	0.0	0.0	0.0	0.0	0.1	0.0
Total	99.9	99.9	99.9	99.9	100.0	100.0	100.0	100.0	100.0	99.9	100.0

Tab. 8

Representative analyses of schreyerite, cassiterite, goethite, pyrochroite and szomolnokite.

Mineral	Schreyerite	Cassiterite	Goethite	Pyrochroite	Szomolnokite
Process	Chl-Ap	Chl-Ap	Chl-Ap	Chl-Ap	Chl-Ap
SiO_2	0.08	0.00	0.70	0.11	0.00
TiO_2	48.80	0.04	0.00	0.00	0.00
Al_2O_3	0.21	0.00	0.22	0.13	0.00
Cr_2O_3	3.71	0.00	0.00	0.00	0.00
SnO_2	1.07	100.37	0.00	0.00	0.00
FeO	0.00	0.14	0.00	1.46	48.83
Fe_2O_3	9.37	0.00	80.35	0.00	0.00
Sc_2O_3	0.71	0.00	0.00	0.00	0.00
V_2O_3	20.14	0.00	0.00	0.00	0.00
Mn_2O_3	1.54	0.00	0.00	0.00	0.00
ZnO	0.61	0.00	0.00	0.00	0.00
MnO	0.00	0.00	0.01	65.36	0.00
CaO	0.00	0.00	0.03	6.76	0.00
SrO	3.04	0.00	0.00	0.00	0.00
PbO	3.33	0.00	0.00	0.00	0.00
MgO	0.05	0.10	0.04	0.93	0.00
UO_2	5.42	0.00	0.00	0.00	0.00
Na_2O	0.00	0.00	0.06	0.00	0.00
SO_3	0.00	0.00	0.00	0.00	47.66
F	0.00	0.00	0.24	0.00	0.00
Cl	0.00	0.00	0.01	0.00	0.00
H_2O	1.05	0.00	18.40	19.69	3.51
Total	99.13	100.67	100.06	94.44	96.49
Si	0.006	0.000	0.023	0.002	0.000
Al	0.018	0.000	0.008	0.002	0.000
V	1.154	0.000	0.000	0.000	0.000
Ti	2.627	0.000	0.000	0.000	0.000
Sn	0.031	0.994	0.000	0.000	0.000
Fe^{3+}	0.504	0.000	1.956	0.000	0.000
Fe^{2+}	0.000	0.003	0.000	0.019	1.103
Cr	0.210	0.000	0.000	0.000	0.000
Sc	0.044	0.000	0.000	0.000	0.000
Mn^{3+}	0.084	0.000	0.000	0.000	0.000
Mn^{2+}	0.000	0.000	0.000	0.843	0.000
Ca	0.000	0.000	0.000	0.110	0.000
Zn	0.032	0.000	0.000	0.000	0.000
Sr	0.126	0.000	0.000	0.000	0.000
Pb	0.064	0.000	0.000	0.000	0.000
Mg	0.005	0.003	0.002	0.021	0.000
U	0.086	0.000	0.000	0.000	0.000
Na	0.000	0.000	0.004	0.000	0.000
S	0.000	0.000	0.000	0.000	0.965
Cations	4.991	1.000	1.994	0.997	2.068
OH	0.50	0.00	3.98	2.00	0.00
O	9	2	5	2	4

Tab. 9
Representative analyses of V/Cr-rich muscovite-phengite, V/Cr-rich phengite-illite, V-rich chlorite, chlorite and kaolinite.

Mineral	Phengite	Phengite	Phengite	Phengite	Phengite	Phengite	Phengite	Phengite	Phengite -Illite	Phengite-Illite	Phengite-Illite	Phengite-Illite	Chlorite	Chlorite	Chlorite	Chlorite	Chlorite	Kaolinite
Enriched	V	V	V/Cr	V/Cr	V/Cr	V/Cr	V/Cr	V/Cr	V/Cr	V/Cr	V/Cr	V/Cr	V	V			Fe	
Process	Chl-Ap	Chl-Ap	Chl-Ap	Chl-Ap	Chl-Ap	Chl-Ap	Chl-Ap	Chl-Ap	Chl-Ap	Chl-Ap	Chl-Ap	Chl-Ap	Chl-Ap	Chl-Ap	SedEx	SedEx	SedEx	Chl-Ap
SiO_2	48.59	48.08	48.74	47.84	46.02	46.85	45.59	45.58	50.29	50.34	50.74	51.11	24.23	24.20	25.87	26.27	24.06	47.95
TiO_2	0.13	0.17	0.21	0.16	0.25	0.21	0.29	0.47	0.31	0.24	0.34	0.40	0.06	0.03	0.02	0.00	0.00	0.02
Al_2O_3	33.65	29.30	28.41	28.12	24.39	23.29	22.76	22.79	30.55	27.38	26.22	28.06	19.16	17.97	22.26	22.16	19.29	36.44
Cr_2O_3	0.00	0.00	1.54	0.02	1.33	1.39	1.43	0.81	2.06	0.71	1.06	1.15	0.00	0.40	0.00	0.01	0.00	0.01
FeO	1.29	1.80	2.10	2.13	1.27	0.98	0.90	0.92	1.55	2.17	0.91	0.82	37.13	31.55	23.94	25.51	43.85	0.75
V_2O_3	0.47	1.59	2.97	5.00	5.69	7.30	8.29	10.91	3.57	5.43	8.54	9.35	1.07	2.46	0.01	0.00	0.01	0.00
MnO	0.01	0.01	0.00	0.03	0.05	0.04	0.03	0.04	0.03	0.03	0.03	0.00	0.47	0.45	0.29	0.27	0.26	0.00
MgO	1.41	2.04	2.03	1.74	2.03	2.20	1.92	2.02	1.35	1.97	2.16	1.77	5.65	9.54	15.62	14.23	1.44	0.00
CaO	0.02	0.04	0.03	0.02	0.01	0.04	0.02	0.03	0.02	0.04	0.03	0.01	0.02	0.10	0.00	0.03	0.01	0.03
Na_2O	0.55	0.25	0.33	0.32	0.30	0.26	0.20	0.22	0.24	0.22	0.10	0.08	0.00	0.00	0.01	0.01	0.03	0.01
K_2O	8.86	10.05	8.49	9.34	9.09	9.47	9.33	7.38	4.51	5.54	4.46	2.69	0.00	0.00	0.00	0.00	0.00	0.02
Cl	0.00	0.01	0.00	0.00	0.02	0.00	0.01	0.00	0.00	0.00	0.00	0.00	0.01	0.01	0.01	0.01	0.00	0.00
H_2O	4.55	4.40	4.47	4.43	4.20	4.25	4.18	4.23	4.59	4.51	4.55	4.64	10.59	10.68	11.54	11.52	10.39	13.80
Total	99.53	97.74	99.32	99.15	94.65	96.28	94.95	95.40	99.07	98.58	99.14	100.08	98.39	97.39	99.57	100.02	99.34	99.03
Si	3.204	3.277	3.270	3.241	3.283	3.302	3.271	3.234	3.288	3.348	3.345	3.304	5.489	5.432	5.377	5.467	5.553	2.084
AlIV	0.796	0.723	0.730	0.759	0.717	0.698	0.729	0.766	0.712	0.652	0.655	0.696	2.511	2.568	2.623	2.533	2.447	0.000
Sum_T	4	4	4	4	4	4	4	4	4	4	4	4	8	8	8	8	8	2.084
AlVI	1.817	1.629	1.514	1.484	1.332	1.235	1.194	1.139	1.640	1.492	1.381	1.440	2.600	2.182	2.826	2.898	2.796	1.865
V	0.025	0.087	0.160	0.271	0.325	0.412	0.476	0.620	0.187	0.289	0.451	0.484	0.194	0.442	0.002	0.000	0.002	0.000
Ti	0.006	0.009	0.011	0.008	0.013	0.011	0.016	0.025	0.015	0.012	0.017	0.019	0.010	0.005	0.003	0.000	0.000	0.001
Fe^{2+}	0.071	0.103	0.118	0.121	0.076	0.058	0.054	0.055	0.085	0.121	0.050	0.044	7.034	5.922	4.162	4.439	8.464	0.027
Cr	0.000	0.000	0.082	0.001	0.075	0.077	0.081	0.045	0.106	0.037	0.055	0.059	0.000	0.071	0.000	0.002	0.000	0.000
Mn	0.001	0.001	0.000	0.002	0.003	0.002	0.002	0.002	0.002	0.002	0.002	0.000	0.090	0.086	0.051	0.048	0.051	0.000
Mg	0.139	0.207	0.203	0.176	0.216	0.231	0.205	0.214	0.132	0.195	0.212	0.171	1.908	3.192	4.840	4.414	0.495	0.000
Ca	0.001	0.003	0.002	0.001	0.001	0.003	0.002	0.002	0.001	0.003	0.002	0.001	0.005	0.024	0.000	0.007	0.002	0.001
Na	0.070	0.033	0.043	0.042	0.041	0.036	0.028	0.030	0.030	0.028	0.013	0.010	0.000	0.000	0.004	0.004	0.013	0.001
K	0.745	0.874	0.727	0.807	0.827	0.851	0.854	0.668	0.376	0.470	0.375	0.222	0.000	0.000	0.000	0.000	0.000	0.001
Cations	6.875	6.946	6.860	6.913	6.909	6.916	6.912	6.800	6.574	6.649	6.558	6.450	19.841	19.924	19.888	19.812	19.823	3.980
CCl	0.000	0.002	0.000	0.000	0.005	0.000	0.002	0.000	0.000	0.000	0.000	0.000	0.008	0.008	0.007	0.007	0.000	0.000
OH	2.000	1.999	2.000	2.000	1.998	2.000	1.999	2.000	2.000	2.000	2.000	2.000	15.996	15.996	15.996	15.996	16.000	4.000
O	12	12	12	12	12	12	12	12	12	12	12	12	36	36	36	36	36	9

Tab. 10
Representative analyses of In-rich sakuraiite and sphalerite 2.

Mineral	In sakuraiite	In sakuraiite	In sakuraiite	In sakuraiite	In sakuraiite	In sakuraiite	In sakuraiite	Sphalerite 2
Process	Chl-Ap	Chl-Ap	Chl-Ap	Chl-Ap	Chl-Ap	Chl-Ap	Chl-Ap	Chl-Ap
S	32.98	32.83	31.23	32.09	30.38	30.85	29.75	33.24
Cd	0.00	0.00	0.00	0.00	0.54	0.00	0.28	0.27
Ag	0.03	0.04	0.04	0.10	0.11	0.11	0.00	0.01
Zn	42.10	40.77	36.66	34.54	31.57	28.25	20.66	59.63
Fe	8.69	8.59	9.22	8.73	10.29	10.34	8.63	6.61
Mn	0.00	0.00	0.00	0.00	0.01	0.00	0.00	0.00
Cu	5.86	6.15	8.10	8.49	9.76	10.87	14.21	0.00
In	10.78	11.62	14.67	15.97	18.18	19.67	25.83	0.07
Sn	0.00	0.00	0.00	0.00	0.00	0.00	0.42	0.00
Pb	0.00	0.00	0.00	0.00	0.00	0.00	0.16	0.00
Bi	0.00	0.00	0.00	0.00	0.00	0.00	0.27	0.12
Total (wt %)	100.44	100.00	99.91	99.92	100.85	100.09	100.20	99.95
S	1.021	1.024	0.996	1.022	0.980	1.001	1.000	1.001
Cd	0.000	0.000	0.000	0.000	0.005	0.000	0.003	0.002
Ag	0.000	0.000	0.000	0.001	0.001	0.001	0.000	0.000
Sn	0.000	0.000	0.000	0.000	0.000	0.000	0.004	0.000
Cu	0.092	0.097	0.130	0.136	0.159	0.178	0.241	0.000
Zn	0.639	0.624	0.574	0.539	0.500	0.449	0.341	0.881
Mn	0.000	0.000	0.000	0.000	0.000	0.000	0.000	0.000
Fe	0.154	0.154	0.169	0.160	0.191	0.193	0.167	0.114
In	0.093	0.101	0.131	0.142	0.164	0.178	0.243	0.001
Pb	0.000	0.000	0.000	0.000	0.000	0.000	0.001	0.000
Bi	0.000	0.000	0.000	0.000	0.000	0.000	0.001	0.001
Sum (atom.)	1.999	2.000	2.000	2.000	2.000	2.000	2.001	2.000
Sphalerite	63.9	62.4	57.4	53.9	50	44.9	34.1	88.1
Pyrrhotite	15.4	15.4	16.9	16	19.1	19.3	16.7	11.4
Roquesite	18.5	19.8	26.1	27.8	32.3	35.6	48.4	0.1

Oxidácia a rozpad stratiformnej SedEx sulfidickej mineralizácie v epidotovo-amfibolitovej fácii metamorfózy in situ za vzniku kasiteritu, sľúd bohatých na V, In-Sn-Ag-Sb-Pb-Bi-Zn-Fe-As-Cu-Ni-Co sulfidov a Fe-Ca-Pb karbonátov (lokalita Bystrý potok, gemerikum, Západné Karpaty)

Študované územie lokality Bystrý potok budujú šošovky lyditov, kryštalických vápencov a zriedkavo vápencov s dolomitom, ktoré sú súčasťou grafitických fylitov holeckých vrstiev silúrskeho veku (Grecula et al., 2009, 2011). V stratigrafii spodného paleozoika gemerika holecké vrstvy predstavujú podložie albitovo-kvarcitovo-keratofýrového (trachytového v zmysle klasifikácie IUGS) súvrstvia so stratiformnou sulfidickou mineralizáciou SedEx. Táto SedEx mineralizácia vznikla súčasne s keratofýrovým/bazaltovým magmatizmom v neskorom silúre až devóne a pochádzala z exhalátov, ktoré vznikli počas magmatizmu na morskom dne v spodnopaleozoickom rifte (obr. 1, 2 a 3; Grecula et al., 1982, 2009, 2011; Radvanec a Grecula, 2016).

Silúrsko-devónske horninové sekvencie boli metamorfované v závere variskej orogenézy v období 281 – 256 mil. rokov. V amfibolitovej fácii táto metamorfóza spôsobila aj lokálne anatektické tavenie so vznikom granitu typu S v dvoch horúcich líniách. Metamorfóza súvisí s prenosom tepla nad subdukujúcou platňou a vrcholí vznikom ostrovnooblúkového andezitovo-dacitovo-ryolitového vulkanizmu v perme (Radvanec et al., 2017; Radvanec a Gonda, 2019).

Vápencové šošovky na lokalite Bystrý potok boli metamorfované a metasomaticky zmenené na skarn v epidotovo-amfibolitovej fácii (526 – 546 °C, 3 – 6 kbar) a v príbuznej chloritovo-apatitovej zóne (420 – 540 °C; obr. 1 – 3). Skarn tvorí granát $Grs_{41.4-60.2}Sps_{19.8-32.8}Alm_{16.7-22.2}Adr_{0-8.5}$, hedenbergit $Wo_{44.5-50.1}Fs_{31.6-38.2}En_{12.7-20.7}$, epidot, aktinolit, titanit, kremeň, zirkón a zvyšky kalcitu. Pukliny v skarne sú vyplnené krátkymi žilkami pyrochroitu a kalcitu bohatého na Mn (obr. 4, tab. 2). Vypočítaná teplota 526 – 546 °C pri P = 3 – 6 kbar z granátovo-klinopyroxénového geotermometra (Ravna, 2000) a minerálna asociácia skarnu určujú P-T podmienky epidotovo-amfibolitovej fácie (Spear, 1995). Pri zistenej teplote 420 – 540 °C chloritovo-apatitovej zóny vznikol v skarne aj fluórapatit a chlorit, pričom P-T podmienky chloritovo-apatitovej zóny sa čiastočne prekrývajú s P-T podmienkami epidotovo-amfibolitovej fácie (obr. 5). V týchto P-T podmienkach vznikli v matrixe silikátov skarnu aj sulfidy. V skarne vznikol kobaltit a millerit bol čiastočne nahradený zonálnym hauchecornitom a hauchecornitom-(Sb) (obr. 4, 21, tab. 1). Stabilné relikty dolomitu z holeckých vrstiev boli postupne zatláčané ankeritom, goethitom a sideritom (obr. 11d, f).

Premenou organickej substancie na grafit v epidotovo-amfibolitovej fácii sa z holeckých vrstiev do nadložia s keratofýrmi a primárnou stratiformnou SedEx sulfidickou mineralizáciou uvoľnila fluidná fáza s obsahom O_2, H_2O, CO_2, H_3PO_4, H_2S, HF a V, kde vznikli impregnácie schreyeritu, bielej sľudy-fengitu a chloritu v matrixe s obsahom zmesi pôvodných SedEx sulfidov (obr. 5 a 13, tab. 1, 8). Primárna stratiformná SedEx sulfidická mineralizácia, zložená prevažne z pyritu 1, menej pyrotínu, chalkopyritu, sfaleritu 1, galenitu 1, arzenopyritu, ferrokesteritu, stefanitu, gudmunditu, bizmutinitu 1, sulfidu bohatého na PbBiSb (typ $A_2B_2S_5$) a kobellitu, bola oxidovaná a rozložená touto fluidnou fázou za vzniku novej metamorfogénnej minerálnej asociácie in situ (obr. 6, 7a, 8, 15 – 19, tab. 3). Pôvodný SedEx pyrotín sa rozpadol na asociáciu szomolnokit, pyrit 2, goethit a siderit (obr. 11a – b, tab. 8). Agregáty galenitu 1 oxidovali a rozkladali sa na zmes anglesit a ceruzit (obr. 11c, tab. 6 a 7). Pôvodná SedEx asociácia ferrokesterit s obsahom In, sakuraiit s obsahom Sn ± In a sfalerit 1 obsahujúci In a molekulu roquesitu oxidovala, rozpadla sa a zreagovala na kasiterit, chalkopyrit, sakuraiit s obsahom In a na sfalerit 2 (obr. 9, 10, 14 – 17, tab. 5). Lokálne a vzácne vznikol aj agregát zmesi allanit-(Ce), galenit 1, fluórapatit a kasiterit v matrixe zmesi dolomitu, sideritu a kremeňa. Vzácny je aj vznik agregátu siderit a bastnäsit-(Ce) v matrixe kremeňa (obr. 7b, 11f). Siderit je na skúmanej lokalite bežný minerál. Sulfid PbSbBi (typ $A_2B_3S_6$), wittit s obsahom S, bizmutinit 2, rýdzi Bi a galenit 2 s obsahom Se sú nové minerály, ktoré vznikli z rozpadu sulfidu PbBiSb (typ $A_2B_2S_5$), kobellitu a bizmutinitu 1 (obr. 19, 20, 21, tab. 4). Tri zóny tetraedritov od tetraedritu-(Fe) cez kenoargentotetraedrit-(Fe) až po rozhdestvenskayait-(Fe) ukazujú postupné usporiadanie tetraedritov v troch oddelených zónach riadených medzerami nemiešateľnosti v Cu-Ag substitúcii. Tetraedrity 1 – 3 vznikli rozkladom pôvodného ferrokesteritu, stephanitu a gudmunditu (obr. 18, 21, tab. 6). Gudmundit tiež oxidoval na valentinit (obr. 18e – f, 21, tab. 6). Aj bournonit a sulfid podobný plumositu vznikli rozkladom pôvodnej SedEx asociácie ferrokesterit, galenit 1 a gudmundit (obr. 11e, 14c, 21, tab. 6). Celkovo 22 reakcií opisuje vzťah medzi zdrojovou SedEx mineralizáciou a novými metamorfogénnymi minerálmi, ktoré vznikli na úkor pôvodnej stratiformnej SedEx sulfidickej mineralizácie in situ. Chemické zloženie oxidov, sulfidov, sulfátov a Fe-Ca-Pb karbonátov sú vizualizované v tetraédroch, diagramoch a trojuholníkových diagramoch (obr. 5, 9, 10, 12, 17, 20, 21).

Metamorfogénna fluidná fáza uvoľnená z holeckých vrstiev bola obohatená o ďalšie prvky v stratigrafickom horizonte stratiformnej SedEx sulfidickej mineralizácie. V tomto SedEx horizonte boli pôvodné sulfidy v chloritovo-apatitovej zóne oxidované a rozložené 22 reakciami. Pôvodná fluidná fáza z holeckých vrstiev bola takto obohatená a mala nasledujúce zloženie: O_2, H_2S, H_2O, CO_2, HF, H_3PO_4, K, Na, Ca, Al, Si, Fe, Mg, Mn, Sn, V, REE, U, Ti, Y, Cu, Sb, Bi, Ag, Zn, In, Pb, Ni, Co a As. Geneticky je súčasťou permského matamorfno-magmaticko-hydrotermálneho (MMH) cyklu (Radvanec a Gonda, 2019). Fluidná fáza generovaná v tomto MMH cykle migrovala do štruktúr, kde sa v závislosti od polohy, v ktorej tieto štruktúry vznikli, vytvorili rôzne typy mineralizácie od greisenov a skarnov, ktoré sa nachádzajú v amfibolitovej alebo v epidotovo-amfibolitovej fácii, až po žily v chloritovej zóne gemerika (Grecula et al., 1995; Radvanec a Gonda, 2019).

Doručené / Received: 8. 6. 2022
Prijaté na publikovanie / Accepted: 15. 12. 2022